Distinguishing Magmatic and Metamorphic Processes in Peralkaline Rocks

Petrogenesis and geochemical evolution of the Norra Kärr Complex, Southern Sweden

Dissertation

der Mathematisch-Naturwissenschaftlichen Fakultät
der Eberhard Karls Universität Tübingen
zur Erlangung des Grades eines
Doktors der Naturwissenschaften
(Dr. rer. nat.)

vorgelegt von
MSc. Geol. Petya Georgieva Atanasova
aus Veliko Tarnovo, Bulgarien

Tübingen
2020

Gedruckt mit Genehmigung der Mathematisch-Naturwissenschaftlichen Fakultät der Eberhard Karls Universität Tübingen.

Tag der mündlichen Qualifikation:	14.10.2020
Stellvertretender Dekan:	Prof. Dr. József Fortágh
1. Berichterstatter:	Prof. Dr. Gregor Markl
2. Berichterstatter:	Priv-Doz. Dr. Michael Marks

Acknowledgement

I am equally indebted to Prof. Dr. Gregor Markl and Dr. habil. Michael A.W. Marks. Thank you very much for your lasting support, your patience and understanding, and for all the constructive criticism. Without the many conversations, discussions, time and effort this dissertation would never have been completed. I always felt welcome and "at home" in Tübingen - this is highly appreciated.

Mark Saxon and Magnus Leijd (formerly Tasman Metals Ltd.) gave me the unique opportunity to work on the Norra Kärr intrusion. Thank you very much for your support in the field, for the access to internal data and sample material and for the trust you have placed in me.

I would like to thank Dr. Max Frenzel, Axel Sjöqvist and Magnus Leijd for their constructive criticism, countless discussions, advice and support in evaluating the results. Magnus Leijd, Johan Berg and Thomas Heinig made it possible to document many kilometers of drill core and to characterize them petrographically – thank you. Dr. Joachim Krause has guided, accompanied and supported me in all analytical questions. Many thanks for the intensive, expert and very productive cooperative work. Thank you Joachim, for your dedication and your willingness to carry out and supervise series of measurements on weekends and at night.

I would especially like to thank my colleagues and friends Dr. Max Frenzel, Dr. Mathias Burisch-Hassel, Elisa Hassel, Dr. Raimon Tolosana Delgado, Dr. Simone Raatz, Lucas and Tina Pereira for their motivation and support during the last years. I would like to thank boundlessly my colleagues and co-owners of ERZLABOR Advanced Solutions GmbH Dr. Dirk Sandmann and Dr. Kai Bachmann for their understanding and support, in particular in the final stages of completing this dissertation. They have helped and repeatedly encouraged me on my way. A very special “Thank You” goes to Dr. Richard Gloaguen for providing the final incentive to complete this dissertation. Dr. Benjamin Walter (now at KIT) is thanked for great hospitality. All the above-mentioned persons have made an important contribution to mastering the balancing act between Freiberg and Tübingen.

Prof. Dr. Peter Kausch, your instinct has led me to the world of rare earths – and to my private and professional happiness. I am deeply grateful to you, Peter, for your long-standing friendship and mentoring.

I owe it to my family to stand here today – thank you to my father, Nasko, Nona, Jörn, Tobias and Saskia! For your love, patience, confidence, inner conviction and unconditional support I am deeply indebted to you, my beloved Jens. Thank you - for everything!

To my mother.

You were the first to show me the path I must take.

Abstract

The 1.49 Ga Norra Kärr complex (Sweden) consists of a layered succession of deformed and metamorphosed peralkaline nepheline syenites. The complex was emplaced into the Transscandinavian Igneous Belt either in a volcanic arc setting during the pre-collisional stage of the Danopolonian or Hallandian orogeny or, alternatively, in an active margin setting along the southwestern border of the Fennoscandian Shield. The Norra Kärr intrusive rocks are preserved within a westward-dipping synform, deformed and metamorphosed at moderate to high greenschist-facies conditions during the Sveconorwegian orogeny at 1.15 Ga. Due to the marked metamorphic overprint, the nepheline syenites of the Norra Kärr complex are used in this dissertation as a case study to distinguish the effects of magmatic and metamorphic/hydrothermal processes on the (re-)distribution of high field strength and rare earth elements (REE) in alkaline rocks. For this purpose, a detailed petrographic and mineralogical investigation of the different lithotypes that constitute the Norra Kärr Complex was carried out and combined with studies on the elemental composition of the ore-forming minerals based on electron probe microanalyses. This was further complemented by trace element data for eudialyte-group minerals and clinopyroxenes using laser ablation inductively-coupled mass spectrometry.

Regardless of the intense deformation during the Sveconorwegian–Grenvillian orogeny, indications for primary magmatic layering of the Norra Kärr intrusion are retained. The trace element chemistry of eudialyte-group minerals mimic whole-rock compositions and display well-developed negative Eu-anomalies and strong Sr- and Ba-depletions in chondrite-normalized diagrams. These imply that the Norra Kärr nepheline syenites formed by intense fractional crystallization from an alkali basaltic parental magma. The magmatic mineral assemblage crystallized from a subsolvus syenite melt at continuously decreasing temperatures (700–450°C) and silica activity (0.6–0.3). Owing to initially relatively low peralkalinity and reducing conditions, zirconium was first incorporated into aegirine. Subsequent destabilization of the Zr-rich aegirine indicates increasing peralkalinity, oxygen fugacity and water activity, which resulted in the formation of early magmatic catapleiite. Later crystallization of magmatic Mn- and REE-poor eudialyte-group minerals happened as soon as Cl, REE and high field strength elements were sufficiently enriched in the residual melt.

Metamorphic conditions during the Sveconorwegian–Grenvillian orogeny are constrained to temperatures between 400 and 550°C and a silica activity range of 0.25–0.4. Because of deformation and interaction with hydrothermal fluids, post-magmatic Al-rich aegirine as well as post-magmatic eudialyte-group minerals enriched in REE, Y and Mn were formed. The transition from a magmatic to a metamorphic environment is also recorded by an increase of the REE-content of eudialyte-group minerals. An exceptional enrichment of heavy REE in late metamorphic eudialyte may be the result of residual enrichment: light REE were preferentially mobilized to form local secondary light rare earth-rich rinkite-group mineral assemblages, while the heavy REE stayed behind and formed eudialyte enriched in heavy REE.

This study has documented systematic changes of the mineral chemistry of eudialyte-group minerals as well as clinopyroxenes of the Norra Kärr Complex. Based on field relationships and petrographic arguments, these changes have been associated with the magmatic and metamorphic history of the complex. New insights are thus provided into the behavior of rock-forming silicates in alkaline rocks under medium greenschist to lower amphibolite facies conditions. The results can be tested on and transferred to other metamorphosed peralkaline rocks.

Kurzzusammenfassung

Der 1,49 Ga alte Norra Kärr-Intrusivkomplex (Schweden) besteht aus deformierten und metamorphisierten peralkalischen Nephelinsyeniten. Norra Kärr liegt im Transskandinavischen Magmatischen Gürtel und wurde entweder 1) als Teil eines Vulkanbogens während des präkollisionalen Stadiums der Danopolonischen / Hallandischen Orogenese oder 2) entlang eines aktiven Kontinentalrandes an der südwestlichen Grenze des Fennoskandischen Schildes intrudiert. Die Intrusion ist heute als eine nach Westen einfallende Synform erhalten, die während der Svekonorwegischen Orogenese vor ca. 1,15 Ga unter mäßigen bis hohen grünschieferfazialen Bedingungen deformiert wurde. Die stark verfalteten Gesteine sind eine ideale Fallstudie, um die Effekte magmatischer und metamorpher/hydrothermaler Prozesse in alkalischen Gesteinen sowie die Rolle der Metamorphose bei der Anreicherung und Umverteilung von Seltenerdelementen (REE) zu untersuchen. Zu diesem Zweck wurden detaillierte petrographische und mineralogische Analysen der verschiedenen Lithotypen durchgeführt. Die Arbeit wurde weiterhin durch mineralchemische Untersuchungen mittels Elektronenstrahl-Mikrosonde sowie mit Spurenelementdaten von Eudialyt und Klinopyroxen ergänzt.

Eine primär-magmatische Lagerung ist trotz der intensiven Deformation der Gesteine während der Svekonorwegischen Orogenese erhalten. Die Spurenelementchemie von Eudialyt zeigt gut entwickelte negative Eu-Anomalien und starke Sr- und Ba-Abreicherungen, die gut der Gesamtgesteinsgeochemie entsprechen. Diese implizieren, dass die Nephelinsyenite von Norra-Kärr durch intensive fraktionierte Kristallisation aus einem alkalibasaltischen Magma hervorgegangen sind. Die magmatische Mineralparagenese kristallisierte dabei aus einer subsolvus-syenitischen Schmelze bei kontinuierlich abnehmenden Temperaturen (700-450°C) und Siliciumdioxidaktivitäten (0,6-0,3). Aufgrund der anfänglich relativ niedrigen Peralkalinität unter reduzierenden Bedingungen wurde Zirkonium in Aegirin eingebaut. Die spätere Destabilisierung des Zr-reichen Aegirins deutet auf eine steigende Peralkalinität, Sauerstoff-Fugazität sowie Wasseraktivität hin, welche im Anschluss zur Bildung von frühmagmatischem Katapleiit führten. Die Kristallisation von Mn- und Seltenerdelement-(REE)-armem Eudialyt erfolgte dagegen erst nach ausreichender Anreicherung der Restschmelze mit Cl, REE und HFSE.

Im Rahmen dieser Arbeit wurden die metamorphen Bedingungen während der Svekonorwegisch-Grenvilleschen Orogenese auf Temperaturen zwischen 400 und 550°C und einen Siliciumdioxid-Aktivitätsbereich von 0,25-0,4 geschätzt. Deformation und hydrothermale Alteration führten zur Bildung von postmagmatischem Al-reichen Aegirin. Der Übergang von der magmatischen zur metamorphen Mineralparagenese wird durch die Zunahme des REE-Gehalts in Eudialyt markiert. Die außergewöhnliche Anreicherung von Schweren REE in spätmetamorphem Eudialyt ist auf eine Restanreicherung zurückzuführen: Leichte REE wurden bevorzugt mobilisiert, um lokale sekundäre Minerale zu bilden, während die schweren REE zurückblieben und sich in Eudialyt anreicherten.

Insgesamt hat diese Arbeit die systematischen Veränderungen der Mineralchemie von Eudialyt und Klinopyroxen mithilfe von feldgeologischen und petrographischen Methoden beleuchtet, und die magmatische sowie die metamorphe Geschichte des Norra Kärr-Intrusivkomplexes rekonstruiert. Die so neu gewonnenen Erkenntnisse über das Verhalten gesteinsbildender Silikate in alkalischen Gesteinen bei mittlerer grünschiefer- bis unterer amphibolitfazialer Metamorphose können auf andere metamorphisierte peralkalische Gesteinen übertragen bzw. an solchen getestet werden.

List of publications in the thesis

The thesis contains the results, discussion and interpretation of the following studies:

A)

Atanasova, P., Krause, J., Möckel, R., Osbahr, I., Gutzmer, J., 2015. Electron Probe Microanalysis of REE in Eudialyte Group Minerals: Challenges and Solutions. Microscopy and Microanalysis, 21(5), 1096–1113. https://doi.org/10.1017/S1431927615000720

B)

Atanasova, P., Marks, M.A.W., Heinig, T., Krause, J., Gutzmer, J., Markl, G., 2017. Distinguishing Magmatic and Metamorphic Processes in Peralkaline Rocks of the Norra Kärr Complex (Southern Sweden) Using Textural and Compositional Variations of Clinopyroxene and Eudialyte-group Minerals. J. Petrol. 58, 361–384. https://doi.org/10.1093/petrology/egx019

C)

Atanasova, P., Marks, M.A.W., Frenzel, M., Gutzmer, J., Krause, J., Markl, G., Fractionation of geochemical twins (Zr/Hf, Nb/Ta and Y/Ho) and HREE-enrichment during magmatic and metamorphic processes in peralkaline nepheline syenites from Norra Kärr (Sweden). Submitted for puclication in Lithos.

Description of personal contribution

In the following, authors' contributions to publications that constitute this thesis are specified.

Author	Author position	Scientific ideas %	Data generation %	Analysis and interpretation %	Paper writing %
Atanasova, P	1	70	70	60	80
Krause, J	2	20	25	25	8
Möckel, R	3	0	5	5	2
Osbahr, I	4	0	0	5	5
Gutzmer, J	5	10	0	5	5
Title of paper		Microanalysis of REE in Eudialyte Group Minerals: Challenges and Solutions.			
Status in publication process		Accepted and published			

Author	Author position	Scientific ideas %	Data generation %	Analysis and interpretation %	Paper writing %
Atanasova, P	1	60	80	50	75
Marks, MAW	2	20	0	20	10
Heinig, T	3	3	10	10	3
Krause, J	4	2	10	10	2
Gutzmer, J	5	5		5	5
Markl, G	6	10	0	5	5
Title of paper		Distinguishing Magmatic and Metamorphic Processes in Peralkaline Rocks of the Norra Kärr Complex (Southern Sweden) Using Textural and Compositional Variations of Clinopyroxene and Eudialyte-group Minerals.			
Status in publication process		Accepted and published			

Author	Author position	Scientific ideas %	Data generation %	Analysis and interpretation %	Paper writing %
Atanasova, P	1	60	90	60	70
Marks, MAW	2	30	0	25	20
Frenzel, M	3	4	0	5	0
Gutzmer, J	4	3	0	5	5
Krause, J	5	0	10	0	0
Markl, G	6	3	0	5	5
Title of paper		Fractionation of geochemical twins (Zr/Hf, Nb/Ta and Y/Ho) and HREE-enrichment during magmatic and metamorphic processes in peralkaline nepheline syenites from Norra Kärr (Sweden).			
Status in publication process		Submitted for publication in Lithos			

Table of contents

Introduction

Because of broad applications in high-tech products and possible supply disruptions, interest in the geology of ore deposits of high field strength elements (HFSE) in general and rare earth elements (REE) in particular has experienced a dramatic increase in the last decade. Besides carbonatites, alkaline and especially peralkaline rocks are particularly enriched in HFSE and comprise one of the most promising sources for future supply (e.g., Goodenough et al., 2016; Mitchell, 2015; Smith et al., 2016). Their economic potential was already pointed out by, e.g., Ovchinnikov and Solodov (1980), Smirnov (1974) and Sørensen (1992). The extraordinary enrichment of HFSE and REE in such rocks was explained by the high alkalinity and the reducing conditions during crystallization of the magma, which minimizes the loss of volatile components and maximizes the potential for minerals enriched in HFSE or REE to precipitate during magmatic differentiation (e.g., Kogarko, 1990; Marks et al., 2011; Marks and Markl, 2017).

Peralkaline (molar (Na + K)/Al) ratio > 1) nepheline syenites generally consist of minerals such as alkali feldspar, feldspathoids, sodic amphibole/clinopyroxene and in some cases eudialyte-group minerals (EGM) (Marks and Markl, 2017). Within this context, the mineral chemistry of the EGM is of particular interest. These are often regarded as the primary host of HFSE, although it is well known that the amounts of Zr, Nb, REE and Y may be highly variable (e.g., Johnsen et al., 2003; Pfaff et al., 2010; Rastsvetaeva, 2007; Schilling et al., 2011). The formation of EGM from peralkaline melts is favored by low fO_2 and low H_2O activities (Marks and Markl, 2017 and references therein). Importantly, EGM inherit characteristics from their parental melts (or fluids) which, in turn, are controlled by source characteristics and fractionation of previously crystallizing minerals (e.g., Schilling et al., 2011). In addition, crystal chemical effects likely contribute to trace element incorporation into EGM (Borst et al., 2019). Magmatic EGM are easily altered; metamorphic or hydrothermal overprints result in complex REE-redistribution processes and the formation of separate REE-, Zr- and Nb-minerals (e.g., Borst et al., 2016; Karup-Møller et al., 2010; Karup-Møller and Rose-Hansen, 2013; Möller and Williams-Jones, 2017; Salvi et al., 2000). Yet, today there is still no conclusive evidence for preferential partitioning in EGM for any of the REE or HFSE leading to fractionation trends in the evolving melts (e.g., Marks et al., 2008; Möller and Williams-Jones, 2016; Pfaff et al., 2008; Schilling et al., 2011).

Sodic clinopyoxene (cpx, aegirine-augite to aegirine) is often intimately associated with EGM in peralkaline nepheline syenites (Marks et al., 2011; Marks and Markl, 2017). Based on field studies and experimental data, sodic clinopyroxene does not show strong affinity for the REE (e.g., Beard, 2018; Marks et al., 2004), though they may incorporate significant amounts of other trace elements. The influence of cpx on the formation of economic REE and HFSE occurrences in peralkaline systems is not well understood. However, as key fractionating mineral in alkaline magmatic systems, cpx is relevant for the interpretation of magmatic processes (e.g., Kogarko, 2015; Marks et al., 2004; Möller and Williams-Jones, 2016; Wood and Blundy, 1997). Although systematic changes in major element composition of cpx are common in post-magmatic alteration (Borst et al., 2016; Chakrabarty et al., 2016; Currie and Curtis, 1976), little is known about trace element behavior during such geological overprints.

Many well-studied examples of agpaitic complexes such as the Ilímaussaq complex in Greenland (Dostal, 2015; Marks and Markl, 2015; Sørensen et al., 2006; Upton, 2013) or the Lovozero and Khibina complexes in Russia (Arzamastsev et al., 2005, 2001; Kogarko, 1987; Kogarko et al., 1982; Pekov, 1998) have remained largely unmetamorphosed and undeformed. Knowledge about the behaviour of agpaitic rocks during metamorphism is thus rather limited, but include preliminary studies on the Red Wine and Kipawa complexes in Canada (Breemen and Currie, 2004; Currie and Breemen, 1996; Curtis and Currie, 1981; Curtis and Gittins, 1979), nepheline syenites in Malawi (Woolley et al., 1996) and peralkaline gneisses in India (Chakrabarty et al., 2018, 2016; Goswami and Basu, 2013; Nanda et al., 2008).

The peralkaline Norra Kärr Complex in Sweden (Fig. 1) is a small Proterozoic peralkaline intrusion that has been deformed and partially recrystallized during several metamorphic events (Atanasova et al., 2017; Sjöqvist, 2015). Furthermore, the EGM-bearing nepheline syenites of the Norra Kärr Complex are marked by very high concentrations especially of heavy REE (HREE) (Sjöqvist, 2015; Sjöqvist et al., 2014, 2013). Finally, excellent exposures related to recent exploration drilling (Heinig, 2012) render the succession of the Norra Kärr Complex a highly suitable natural laboratory to distinguish the effects of magmatic and metamorphic/hydrothermal processes in nepheline syenites.

Norra Kärr – discovery, research and exploration

The Norra Kärr Alkaline Complex (in short "Norra Kärr") was discovered on Norra Kärr farm during regional bedrock mapping by the Swedish Geological Survey (SGU) and first described by Törnebohm (1906). The intrusion is located about 2 km east of Lake Vättern (58°06' N, 14°40' E; Figure 2) and approx. 15 km NNE of the township of Gränna in Southern Sweden. It has a roughly elliptical shape (1200 m × 400 m) with the long axis aligned approximately north-south. The general dip is approximately 45° to the west. Törnebohm (1906) published first geologic and petrographic descriptions of "katapleite-syenite" at Norra Kärr including the identification of the two zirconosilicates eudialyte and catapleiite. Adamson (1944) completed comprehensive, petrographic work of all rock types and complemented the descriptions by hand-painted micrographs. He renamed the fine-grained greenish syenite into "Grennaite", after the close by town Gränna (Adamson, 1944).

During the Second World War and in the 1970s, Swedish mining company Boliden AB started exploration activities for zirconium and nepheline. Of primary interest during the Second World War was the possible exploitation of zirconium, while in the 1970s exploration focused on nepheline. In both cases, the extraction was regarded as uneconomic and Boliden AB interrupted its activities. At that time, the complex was dated for the first time by Blaxland (1977) and von Eckermann (1968).

Extraordinary enrichment in particular of HREE resulted in renewed exploration of Norra Kärr in the fall of 2009. Tasman Metals Ltd., a Canadian junior exploration company, drilled approx. 21 km of diamond exploration core and performed geochemical assays of ca. 10000 samples, culminating in the publication of a prefeasibility report for mining and extraction of rare earth elements and zirconium in 2015 (Short et al., 2015). Tasman Metals was taken over by Leading Edge Materials in 2016, a company that still maintains the exploration rights to Norra Kärr (Leading Edge Materials Corp., 2018). Active mineral exploration enabled geoscientific research at many different locations around the world, e.g. University of Gothenburg (Sjöqvist, 2015; Sjöqvist et al., 2017, 2014, 2013), University of Britisch Columbia (Bluemel et al., 2013) or University of Tübingen (Knittel, 2017).

Geological setting

The Norra Kärr Alkaline Complex (Fig. 1) is situated in the Trans-Scandinavian Igneous Belt, which intruded into the Svecofennian domain of Fennoscandia in the course of juvenile crust reworking between 1.85–1.75 Ga (Andersson et al., 2007 and references therein). The Trans-scandinavian Igneous Belt extends over a distance of ca. 1400 km from NW Norway to SE Sweden and comprises of an array of monzodioritic to granitic batholiths of alkali-calcic to calc-alkaline composition (Högdahl et al., 2004).

Sjöqvist et al. (2017) constrained the magmatic emplacement of the Norra Kärr Complex into the TIB at 1.49±0.01 Ga by dating zircons from the fenizited zone surrounding the complex with the U–Pb method by LA-MC-ICP-MS. The age may be used to suggest an emplacement related either to extensional or collisional geotectonic events of regional importance. Between 1.65 and 1.50 Ga, an active extensional margin existed along the southwestern border of the Fennoscandian Shield (McLelland, 1989); the intrusion of alkali-calcic and calc-alkaline magmas into the southernmost parts of the TIB may be related to this event (Åberg, 1988). There is no clear indication in the literature that Norra Kärr rocks are genetically linked to the intrusions mentioned above, but age and geochemical affinity render a relationship possible. Another possible scenario is the emplacement of the Norra Kärr Complex in a typical volcanic arc setting during the pre-collisional stage of the Danopolonian or Hallandian orogeny, which took place at approx. 1.47 Ga. At that time, to the east and south-east of Lake Vättern, A- and I-type magmatism is reported (Brander, 2011; Brander and Söderlund, 2009).

Between 1140 – 900 Ma wide areas of the southern and central TIB, as well as broad areas of south-western Fennoscandia were deformed and metamorphosed during the collision of Fennoscandia with Amazonia (Grenvillian/Sveconorwegian orogeny, Bingen et al., 2008). These areas are now referred to as the Sveconorwegian orogenic belt. The area east of Lake Vättern belongs to the frontal zone of this orogen and was mainly affected by metamorphism during the late stages of the orogeny, the so-called Falkenberg and Dalane phases (e.g., Bingen et al., 2008 and references therein). During the Falkenberg phase (980-970 Ma) crustal thickening and associated eclogite facies conditions affected the Fennoscandian crust. This was followed by decompression, relaxation and gravitational collapse during the Dalane phase at 970-900 Ma (Bingen et al., 2008, 2006; Möller et al., 2007). During this time the N-S trending

Protogine Zone was formed as a steep, sheer zone at the very front of the Sveconorvegian orogeny (Andréasson and Rodhe, 1994; Söderlund et al., 2004; Wahlgren et al., 1994).

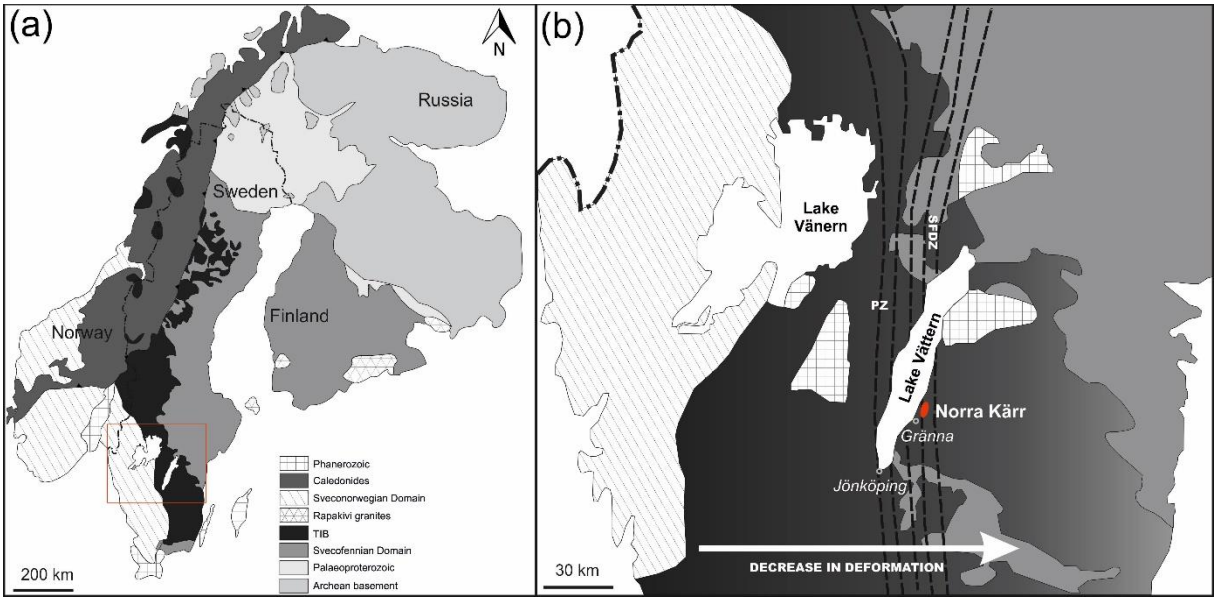

Fig.1. (a) Simplified geological map of Fennoscandia illustrating major lithological units (modified after Högdahl et al., 2004). Red box is enlarged in (b), where the red ellipse marks the Norra Kärr Alkaline Complex. The white arrow indicates the direction of decreasing regional deformation during the Sveconorwegian orogeny. PZ - Protogine Zone, SFDZ - Sveconorwegian Frontal Deformation Zone (simplified after Söderlund et al., 2002; Wahlgren et al., 1994).

The Norra Kärr Alkaline Complex

The Norra Kärr Complex covers an area of approx. 350 x 1100 m and is located in the Växjö Granite Suite (TIB I), between the Vimmerby Batholith in the east and the major Protogine shear zone (PZ) in the west (Fig. 1b). The body is preserved within a westwards dipping (approx. 40°) synform (Fig. 2), deformed by moderate E-W and late, weak N-S directed compression under ductile conditions (Rankin, 2011).

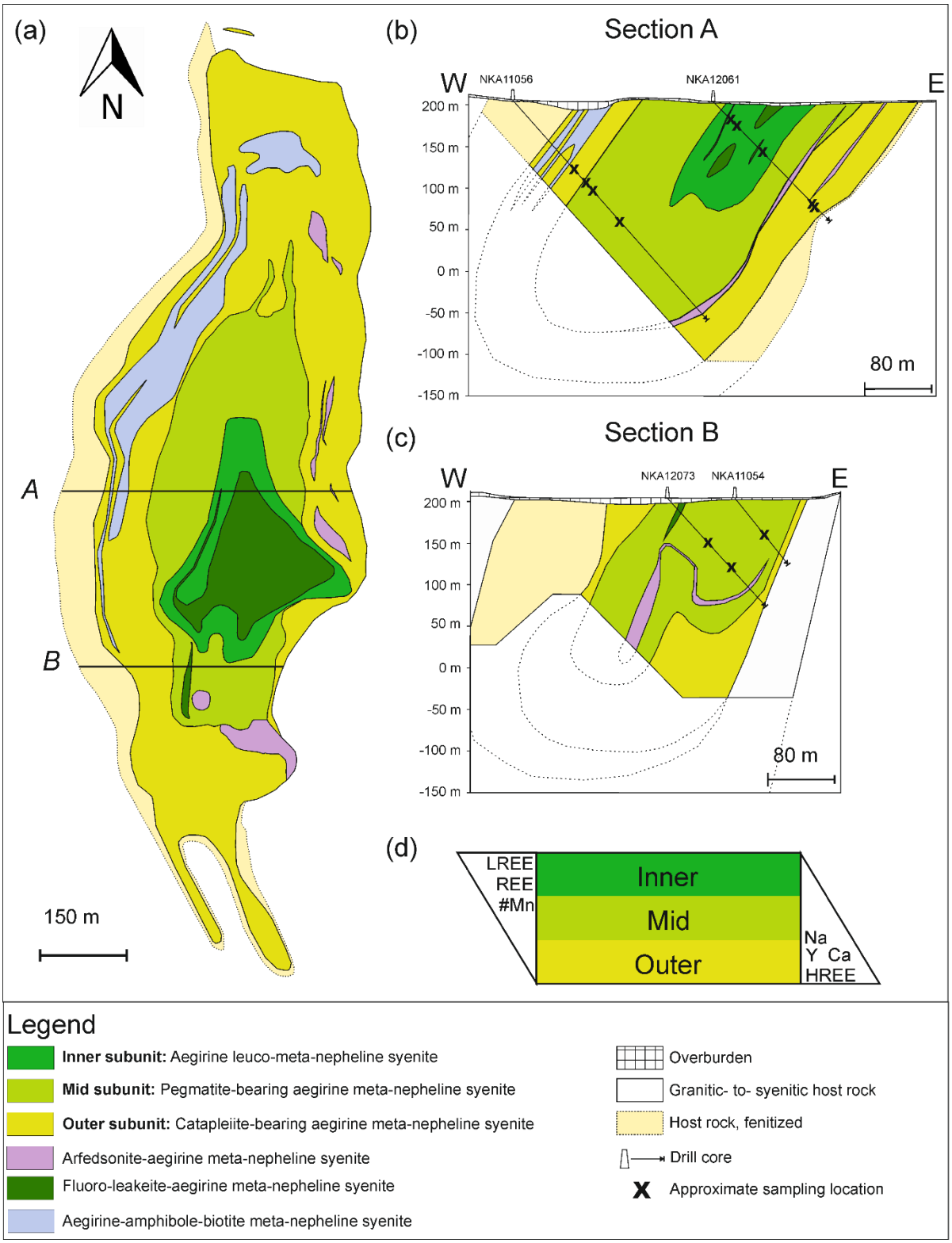

Fig.2. (a) Simplified geological map of Norra Kärr illustrating major lithological units (modified after Tasman Metals Ltd., with contributions of Heinig, 2012). The deformation is well visualized in W-E cross sections (b) Section A and (c) Section B. Approximate sampling location of samples used for this study as listed in Table 1 are indicated. d) Possible primary magmatic layering of the intrusion with preserved major and trace element enrichment and depletion (#Mn = Mn/(Mn+Fe)).

Lithological Architecture

The granitic host rocks at the western contact of the Norra Kärr Alkaline Complex and some deeper parts in the east (only known from drill cores) exhibit clear signs of fenitization (Adamson, 1944; Sjöqvist, 2015; von Eckermann, 1968). These fenites form an up to 100 m wide contact zone, but also occur as decimeter-thick veins in the surrounding granite. They are characterized by the absence of quartz, which is replaced by albite, magnetite, hematite and fluorite, and the replacement of biotite by aegirine (Adamson, 1944; Sjöqvist, 2015). Fenitization of the alkaline rocks itself is less prominent and rarely occurs in the outer subunit, only at the direct contact to the fenitized host rocks. Recently, the fenitization of the granitic gneisses was dated to 1.49 ± 0.01 Ga (U-Pb zircon age, Sjöqvist et al., 2017), which is interpreted to coincide with the age of magmatic emplacement of Norra Kärr. Younger ages determined by Sjöqvist et al. (2014) constrain the deformation during the Sveconorvegian orogeny from 1148 ± 5 Ma onwards. At Norra Kärr neither the surrounding country rocks (granitic- to- syenitic gneisses) nor the metamorphosed syenites of the complex itself provide any clear evidence indicating the grade of metamorphism of the complex. Regional geological studies (Wahlgren and Stephens, 2004) report lower greenschist facies conditions for the area to the East of Lake Vättern and the Protogine Shear Zone (Fig. 1). Considering this and the actual position of the complex within this major shear zone (Fig. 1), moderate to high greenschist facies conditions can be assumed.

For this study, the peralkaline rocks of Norra Kärr were collectively classified as meta-nepheline syenites (after Gillespie and Styles, 1999; for detailed explanation of this classification see Heinig, 2012). The most common rock type (85 vol.% of the exposed area), the so-called grennaite (Adamson, 1944) is a catapleiite and EGM-bearing aegirine meta-nepheline syenite (Fig. 2). The texture of this unit varies systematically across the deposit (Fig. 3). On the basis of the frequency of medium- to- coarse-grained lenses and bands or schlieren (Adamson, 1944; Sjöqvist, 2015; Törnebohm, 1906), the frequency of catapleiite and the degree of deformation, three subunits with gradual transitions between them are distinguished. The central part (inner subunit) is strongly foliated and best described as an aegirine leuco-meta-nepheline syenite (a.k.a. migmatitic grennaite; lithologic nomenclature by Tasman Metals Ltd., Sjöqvist et al., 2013). This area is surrounded by a zone rich in pegmatoidal schlieren (mid subunit) named pegmatite-bearing aegirine meta-nepheline syenite (a.k.a. pegmatitic grennaite; Adamson, 1944). The border area (outer subunit) of the complex is defined by a foliated

catapleiite-bearing aegirine meta-nepheline syenite (a.k.a. catapleiite grennaite; Adamson, 1944).

Minor rock types of the Norra Kärr Alkaline Complex include strongly folded fluoro-leakeite-aegirine meta-nepheline syenite (previously called kaxtorpite), aegirine-amphibole-biotite meta-nepheline syenite (a.k.a. pulaskite) and arfvedsonite-aegirine meta-nepheline syenite (former lakarpite), well-known from the discovery outcrop of Norra Kärr (Sjöqvist et al., 2013).

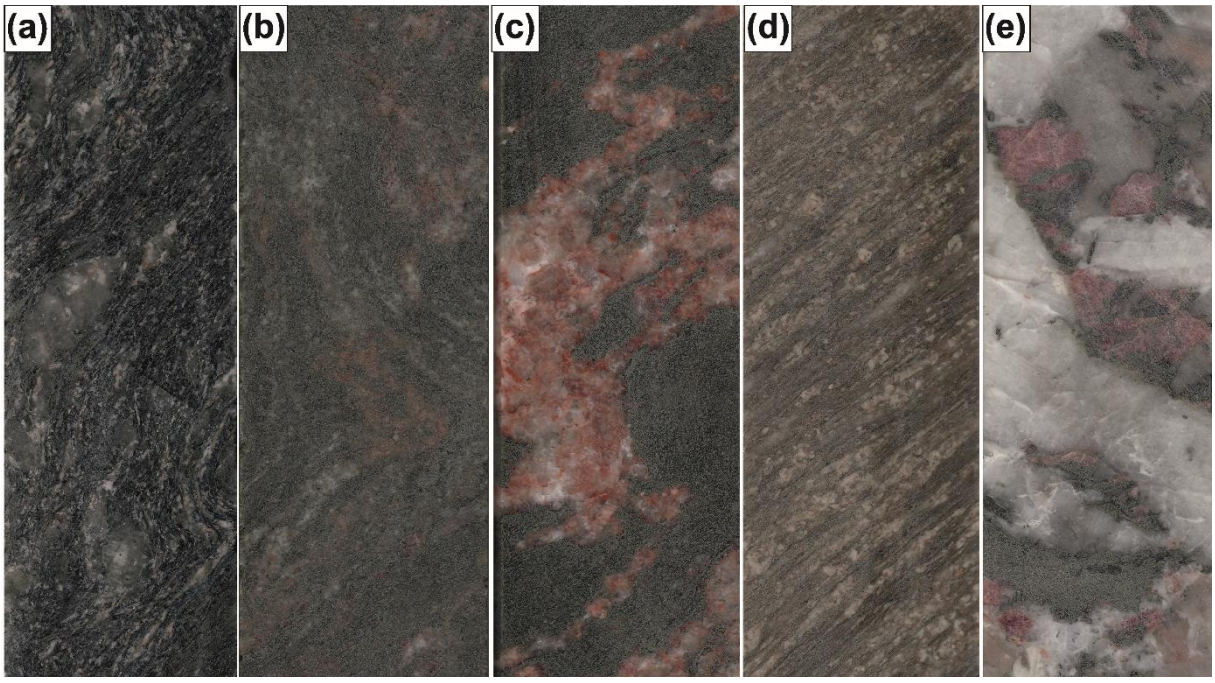

Fig.3. Selected core samples that illustrate characteristic mesoscopic features of lithologies of the Norra Kärr Complex. (a) Folded fluoro-leakeite-aegirine meta-nepheline syenite. (b) Catapleiite-and EGM-bearing aegirine meta-nepheline syenite with 5 % pegmatoidal schlieren sillustrating complex folding. (c) Catapleiite-and EGM-bearing aegirine meta-nepheline syenite with 30 to 50 % pegmatoidal schlieren with small scale folding of the schlieren, minerals show hematization. (d) Foliated fine- to medium-grained aegirine leuco-meta-nepheline syenite. (e) Coarse-grained schlieren with microcline, albite and EGM, fine-grained euhedral aegirine forms patchy aggregates.

Deformation and Metamorphism

The most common deformation features of all rock types include the alignment and stretching of some minerals, e.g., clinopyroxene, EGM, and catapleiite as well as the presence of porphyroclasts (mainly microcline), which have tails of recrystallized material. The porphyroblasts are commonly preserved in a finer-grained, probably recrystallized matrix and form typical shear-related patterns (sigma- and delta-clasts). In the inner subunit, crenulated foliation and almost "migmatitic" recrystallized structures are observed. The outer subunit is often schistose and gradually fine-grained to aphanitic. It has porphyric appearance and often includes laths like, 1 – 30 mm long, elongated to needle-like crystals of catapleiite.

Objectives and Approach

The two major aims of this study are:

1. to distinguish the magmatic attributes of an agpaitic complex from characteristics related to subsequent deformation and metamorphism.
2. to differentiate the effects of HFSE and REE partitioning under magmatic and metamorphic conditions.

To achieve these aims, a large suite of samples of the different lithotypes was selected from deep (unweathered) diamond drill core across the Norra Kärr Complex. More than 100 polished thin sections were prepared from this suite of samples. Detailed petrographic characterization was carried out for all lithotypes using light and electron microscopic methods. This was done to understand mineralogical changes and to identify possible mineral reactions (see Fig.4). This was complemented by detailed mineral chemical studies, using electron microprobe as well as laser ablation ICPMS data, in order to constrain the redistribution of HFSE – and in particular REE during alteration and metamorphism (Fig. 4). In order to minimize crystal damage and to achieve accurate quantification of the rather complex chemical composition of EGM with the electron microprobe, a dedicated analytical protocol had to be developed and tested. A final set-up was chosen to minimize the instability of EGM under the electron beam.

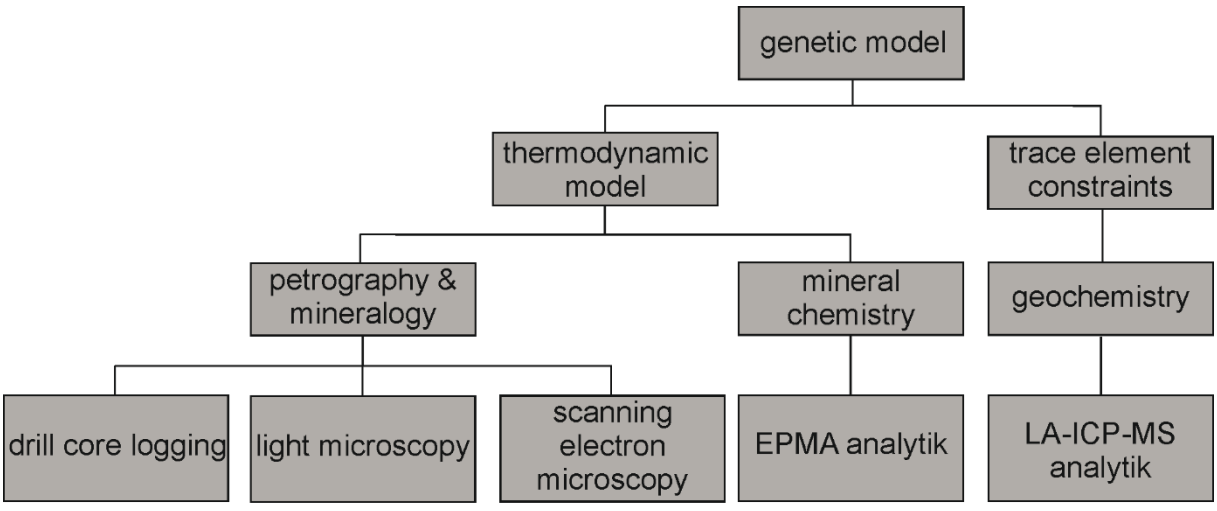

Fig. 4 Overview of workflow including analytical methods applied and all major outputs obtained.

Electron Probe Microanalysis of REE in Eudialyte Group Minerals: Challenges and Solutions

The monitoring of systematic variations in major, minor and trace element compositions of ore-forming minerals such as eudialyte-group minerals (EGM) is a powerful tool in reconstructing geological processes at local as well as regional scale. The electron probe microanalyzer (EPMA) is an essential and very widespread analytical technique for the systematic collection of robust mineral chemistry data sets.

Using EPMA, major and minor element concentrations can be quantified. However, the accurate quantification of the chemical composition of EGM with EPMA is complicated by structural and chemical variability, mutual interferences of X-ray lines, in particular of the rare earth elements, diffusive volatility of light anions (e.g., F^-, Cl^-) and cations (e.g., Na^+, K^+ or Si^{4+}) and instability of EGM under the electron beam, i.e. due to lattice changes or even glass formation. Though such difficulties were known (see e.g. Chakrabarty et al., 2012; Olivo and Williams-Jones, 1999), neither a systematic documentation of the instability of EGM under the electron beam, nor a protocol of optimal conditions for measurement routines has been publicly available. For this dissertation, 101 experiments have been designed and evaluated, in order to minimize crystal damage during routine measurements of EGM and in order to yield robust quantitative mineral chemistry data. Thirty different instrumental setups combining the four variables beam mode (steady vs. scanning mode), beam diameter (1-20 µm), edge length of scanned square (8-20 µm) and scanning speed (1-10) were evaluated. Repeatability was ensured by conducting 30 measurements for each of the 30 settings. All 900 measurements were repeated for three measurement sequences A, B, and C.

The effects of diffusive volatility and beam damage have been found to be minimal, when a square of 20x20 µm is scanned with a beam diameter of 6 µm at the fastest possible speed, while measuring elements critical to electron beam exposure (e.g., Na, Cl, F, Si, and Ca) early in the measurement sequence. In addition, matrix-matched reference materials have been selected defined and procedures for offline corrections of X-ray interferences defined using individual calibration factors.

This first comprehensive methodological study on EMPA analyses of EGM thus yields an optimized analytical approach for the definition of a suitable analytical protocol. A similar approach may well be applicable to other minerals of complex mineral chemistry.

Distinguishing magmatic and metamorphic processes in peralkaline rocks of the Norra Kärr complex (Southern Sweden) using textural and compositional variations of clinopyroxene and eudialyte-group minerals

The peralkaline Norra Kärr Complex has been deformed and partially recrystallized during regional metamorphism. The main aim of this investigation has thus been to distinguish magmatic signatures retained in the nepheline syenites of the Norra Kärr Complex from those characteristics related to subsequent deformation and metamorphism. Mineral textures and compositions of rock-forming silicates were studied for this purpose by light as well as electron microscopy and EPMA. The focus was on structurally and compositionally complex minerals of the eudialyte-group (EGM), catapleiite and clinopyroxene, which are all stable over a large P-T range and thus regarded as suitable monitors for physicochemical changes. Combining textures and paragenetic relations of clinopyroxene and EGM with systematic variations in their chemical composition enabled the reconstruction of magmatic and subsequent metamorphic conditions.

Regardless of the intense deformation due to folding of the Norra Kärr Complex during the Sveconorvegian/Grenvillian orogeny, indications for primary magmatic layering of the intrusion are retained on the deposit scale. This agrees with compositional changes of magmatic EGM from the outer to the inner subunit of the complex that may be interpreted to reflect the effects of fractional crystallization. The reconstruction of the magmatic crystallization conditions delivered new insights of critical parameters for EGM formation. At Norra Kärr, EGM are exceptionally Cl-poor, but may contain up to about 3 wt % H_2O. This observation leads to the conclusion that the stability fields of EGM and catapleiite may coexist. Crystallization of catapleiite and resulting enrichment of REE *vs.* Zr in the melt is identified as a crucial factor stabilizing EGM in this relatively Cl-poor & H_2O-rich environment.

Mean compositions of Al-aegirine from Norra Kärr were used to compute pressures between 2.5 and 8 kbar and temperatures between 300 and 700°C for regional metamorphism, suggesting greenschist- to lower amphibolite-facies conditions. These are the first (broad) constraints on p-T conditions attained during the Sveconorwegian / Grenvillian orogeny in the Norra Kärr Complex. The proposed conditions slightly exceed assumed moderate to high greenschist-facies metamorphic conditions, previously postulated based on regional geological arguments.

Fractionation of geochemical twins (Zr/Hf, Nb/Ta and Y/Ho) and HREE-enrichment during magmatic and metamorphic processes in peralkaline nepheline syenites from Norra Kärr (Sweden)

This study combines three major data sets, namely quantitative mineralogical data, whole-rock geochemical data of all drill hole available and LA-ICP-MS trace element data of eudialyte-group minerals (EGM) and clinopyroxene (cpy) of the Norra Kärr Complex. It aims to differentiate the effects of HFSE and REE partitioning under magmatic and metamorphic conditions. Although systematic changes in major element composition of cpx are common in post-magmatic alteration, little is known about the influence of cpx on the formation of economic REE and HFSE ores in peralkaline systems. Similarly, magmatic EGM are easily altered; metamorphic or hydrothermal overprints result in complex REE-redistribution processes and the formation of separate REE-, Zr- and Nb- minerals, thought there is no conclusive evidence for preferential partitioning of any of the REE or HFSE in EGM.

The exact calculation of partition coefficients was not possible in the course of the study. However, it is obvious that the REE partition coefficients for EGM are always much larger than those for cpx. However, the observed negative correlation in REE incorporation between EGM and cpx suggests that in the absence of major REE-bearing minerals, cpx could incorporate more REE and thus influence the deportment of REE in peralkaline systems.

The study documents further that cpx is able to fractionate the geochemical twins Zr and Hf under magmatic conditions, showing strong affinity for Hf. By contrast, under metamorphic conditions, EGM fractionate the REE (and likely Nb and Ti), resulting in exceptional enrichment of heavy rare earth elements (HREE) vs. light rare earth elements (LREE) in late metamorphic eudialyte. Recrystallization of magmatic EGM during regional metamoprhism evidently leads to the release of LREE and possibly also of Nb and Ti. HREE, in contrast, remained immobile and became residually enriched in late metamorphic, poikilitic EGM. Elements mobilized from EGM were immediately consumed to form rinkite-group minerals, thus essentially retaining the isochemical character of regional metamorphism at a mesoscopic and macroscopic scale. Results suggest that even in highly evolved systems, HFSE can be used as robust proxies for the evolution of the systems, if whole rock geochemical data are combined with mineral chemistry and data on partitioning behavior.

Conclusions

This careful petrographic and mineral chemical study has elucidated the effects of metamorphism, deformation and hydrothermal fluid-rock interaction on the mineralogy and mineral chemistry of agpaitic rocks of the Norra Kärr Complex in Sweden. It contributes to the general understanding of the genesis and alteration of EGM-bearing REE deposits resulting in local HREE enrichment under magmatic and metamorphic conditions.

The Norra Kärr Alkaline Complex is considered to be of alkali basaltic origin with its formation being possibly linked to prolonged rifting and magmatism in the course of the Mesoproterozoic geotectonic evolution of the Scandinavian Shield. Even after intense deformation and regional metamorphism at upper greenschist / lower amphibolite facies conditions, it is still possible to identify primary magmatic textures and compositions in EGM and clinopyroxene from the peralkaline rock suite that comprises the Norra Kärr Complex. Primary magmatic layering of the intrusion is preserved. Progressive enrichment of REE, LREE and Mn in whole rock samples from the bottom towards the top of the layered igneous succession provides important evidence for the primary magmatic nature of this layering.

The two mineral groups that were in the focus of this study, clinopyroxene and EGM, have a large pressure and temperature stability range; both have very variable mineral chemistry and are able to adapt their composition to changing conditions. Therefore, both were studied in detail in order to provide a record of the evolution of the nepheline syenites of the Norra Kärr Complex. Both minerals were found to have crystallized from a subsolvus syenite melt over a rather large temperature interval (700ºC to 450ºC) with a corresponding decrease in a_{SiO2} from 0.6 to about 0.3.

Zirconium-aegirine was the first clinopyroxene to form during magmatic crystallization. It crystallized at relatively low peralkalinity and under reducing conditions. Still during magmatic crystallization and in response to an increase in peralkalinity of the residual magma and at moderate-to-high f_{O2} and a_{H2O}, Zr-aegirine was destabilized and aegirine *sensu stricto* formed. At this point catapleiite became the main host mineral for Zr. Due to the absence of sodalite and the very early formation of catapleiite, a_{HCl} further increased and REE and HFSE were enriched in the residual melt, promoting EGM crystallization. Crystallization of EGM seems not necessarily restricted to specific conditions, forming even at very low a_{HCl} and at relatively high a_{H2O}. EGM crystallization appears to rather be constrained by the concentrations of

specific elements in the melt. Of importance appears to be the availability of REE in the magma in general, and HREE in particular. It remains yet uncertain, if this enrichment is due to the presence of a mantle source pre-enriched in REE, or if it is related to the process of melt formation. Fractional crystallization as expressed by compositional layering preserved in the now deformed and metamorphosed complex is associated with relatively minor, yet systematic changes in whole-rock REE compositions. These trends are closely tracked by the composition of magmatic EGM, the dominant host of REE.

During the Sveconorvegian/Grenvillian orogeny, the rocks of the Norra Kärr Complex were deformed and folded. Late metamorphic EGM and Al-aegirine formed at 400 - 550ºC and in an a_{SiO2} range of 0.25-0.4 at pressures not exceeding 5 kbars. During regional metamorphism EGM interacted with metamorphic fluids, either changing its composition or being partly-destabilized to form catapleiite and secondary REE-bearing britholite or rinkite group minerals. This process was accompanied by local redistribution of REE. As a result, the composition of EGM changed significantly, with HREE becoming enriched in recrystallized EGM and LREE incorporated into e.g. rinkite-group minerals. Remobilization of HFSE remained local in extent, with whole rock compositions evidently affected by this process; regional metamorphism remained evidently isochemical at meso- and macroscopic scale with respect to HFSE.

Yet, the study also illustrates a surprising extent at which geochemical twins such as Zr/Hf or Y/Ho of the HFSE can be fractionated during magmatic and post-magmatic alteration processes. Within this context, Y/Ho fractionation observed in cpx at Norra Kärr is almost certainly related to the regional metamorphic overprint – and not linked to magmatic crystallization. This points to the fact that in highly evolved magmatic systems, such as the Norra Kärr Complex, whole rock data on geochemical twins – element pairs often thought to be suitable as geochemical proxies – should only be regarded as robust proxies that reflect the evolution of the studied system only, if such data are combined with mineral chemistry data.

List of References

Åberg, G., 1988. Middle Proterozoic anorogenic magmatism in Sweden and worldwide. Lithos 21, 279–289.

Adamson, O.J., 1944. The petrology of the Norra Kärr district: An occurrence of alkaline rocks in southern Sweden. GFF 66, 113–255.

Andersson, U.B., Rutanen, H., Johansson, Å., Mansfeld, J., Rimša, A., 2007. Characterization of the Paleoproterozoic mantle beneath the Fennoscandian Shield: Geochemistry and isotope geology (Nd, Sr) of~ 1.8 Ga mafic plutonic rocks from the Transscandinavian Igneous Belt in southeast Sweden. Int. Geol. Rev. 49, 587–625.

Andréasson, P., Rodhe, A., 1994. Ductile and brittle deformation within the Protogine Zone, southern Sweden: a discussion. GFF 116, 115–117.

Arzamastsev, A.A., Belyatsky, B. V, Travin, A. V, Arzamastseva, L. V, Tsarev, S.E., 2005. Dike Rocks in the Khibina Massif: Relations with the Plutonic Series, Age, and Characteristics of the Mantle Source. Petrology 13, 267–288.

Arzamastsev, A.A., Glaznev, V.N., Arzamastseva, L. V, Bea, F., Montero, P., 2001. Kola alkaline province in the Paleozoic: evaluation of primary mantle magma composition and magma generation conditions. Russ. J. Earth Sci. 3.

Atanasova, P., Marks, M.A.W., Heinig, T., Krause, J., Gutzmer, J., Markl, G., 2017. Distinguishing Magmatic and Metamorphic Processes in Peralkaline Rocks of the Norra Kärr Complex (Southern Sweden) Using Textural and Compositional Variations of Clinopyroxene and Eudialyte-group Minerals. J. Petrol. 58, 361–384. https://doi.org/10.1093/petrology/egx019

Beard, C.D., 2018. Mineral-melt trace element partitioning in alkaline magmatic systems 152.

Bingen, B., Nordgulen, O., Viola, G., 2008. A four-phase model for the Sveconorwegian orogeny, SW Scandinavia. Nor. Geol. Tidsskr. 88, 43.

Bingen, B., Stein, H.J., Bogaerts, M., Bolle, O., Mansfeld, J., 2006. Molybdenite Re–Os dating constrains gravitational collapse of the Sveconorwegian orogen, SW Scandinavia. Lithos 87, 328–346.

Blaxland, A.B., 1977. Agpaitic magmatism at Norra Kärr? Rb□ Sr isotopic evidence. Lithos 10, 1–8.

Bluemel, B., Leijd, M., Dunn, C., Hart, C.J.R., Saxon, M., Sadeghi, M., 2013. Biogeochemical expression of rare earth element and zirconium mineralization at Norra Kärr, Southern Sweden. J. Geochemical Explor. https://doi.org/10.1016/j.gexplo.2012.12.005

Borst, A.M., Finch, A.A., Friis, H., Horsburgh, N.J., Gamaletsos, P.N., Goettlicher, J., Steininger, R., Geraki, K., 2019. Structural state of rare earth elements in eudialyte-group minerals. Mineral. Mag. 1–16. https://doi.org/10.1180/mgm.2019.50

Borst, A.M., Friis, H., Andersen, T., Nielsen, T.F.D., Waight, T.E., Smit, M.A., 2016. Zirconosilicates in the kakortokites of the Ilímaussaq complex, South Greenland:

Implications for fluid evolution and high-field-strength and rare-earth element mineralization in agpaitic systems. Mineral. Mag. 80, 5–30.

Brander, L., 2011. The Mesoproterozoic Hallandian event-a region-scale orogenic event in the Fennoscandian Shield.

Brander, L., Söderlund, U., 2009. Mesoproterozoic (1.47–1.44 Ga) orogenic magmatism in Fennoscandia; Baddeleyite U–Pb dating of a suite of massif-type anorthosite in S. Sweden. Int. J. Earth Sci. 98, 499–516.

Breemen, O. van, Currie, K.L., 2004. Geology and U Pb geochronology of the Kipawa Syenite Complex a thrust related alkaline pluton and adjacent rocks in the Grenville Province of western Quebec. Can. J. Earth Sci. 41, 431–455.

Chakrabarty, A., Mitchell, R.H., Ren, M., Pal, Supriyo, Pal, Supratim, Sen, A.K., 2018. Nb-Zr-REE re-mobilization and implications for transitional agpaitic rock formation: insights from the Sushina Hill Complex, India. J. Petrol. https://doi.org/10.1093/petrology/egy084

Chakrabarty, A., Mitchell, R.H., Ren, M., Saha, P.K., Pal, S., Pruseth, K.L., Sen, A.K., 2016. Magmatic, hydrothermal and subsolidus evolution of the agpaitic nepheline syenites of the Sushina Hill Complex, India: implications for the metamorphism of peralkaline syenites. Mineral. Mag. 80, 1161–1193. https://doi.org/10.1180/minmag.2016.080.057

Chakrabarty, A., Pruseth, K.L., Sen, A.K., 2012. Compositions and petrogenetic significance of the eudialyte group minerals from Sushina, Purulia, West Bengal. J. Geol. Soc. India 79, 449–459.

Currie, K.L., Breemen, O. van, 1996. The Origin of Rare Minerals in the Kipawa Syenite Complex Western Quebec. Can. Mineral. 34, 435–451.

Currie, K.L., Curtis, L.W., 1976. An application of multicomponent solution theory to jadeitic pyroxenes. J. Geol. 179–194.

Curtis, L.W., Currie, K.L., 1981. Geology and petrology of the Red Wine alkaline complex, central Labrador. Geological Survey of Canada.

Curtis, L.W., Gittins, J., 1979. Aluminous and titaniferous clinopyroxenes from regionally metamorphosed agpaitic rocks in central Labrador. J. Petrol. 20, 165–186.

Dostal, J., 2015. Rare Metal Deposits Associated with Alkaline/Peralkaline Igneous Rocks. Rev. Econ. Geol. 18.

Gillespie, M., Styles, M., 1999. BGS rock classification scheme, Volume 1. Classification of igneous rocks.

Goodenough, K.M., Schilling, J., Jonsson, E., Kalvig, P., Charles, N., Tuduri, J., Deady, E.A., Sadeghi, M., Schiellerup, H., Müller, A., Bertrand, G., Arvanitidis, N., Eliopoulos, D.G., Shaw, R.A., Thrane, K., Keulen, N., 2016. Europe's rare earth element resource potential: An overview of REE metallogenetic provinces and their geodynamic setting. Ore Geol. Rev. 72, Part 1, 838–856. https://doi.org/http://dx.doi.org/10.1016/j.oregeorev.2015.09.019

Goswami, B., Basu, S.K., 2013. Metamorphism of Proterozoic agpaitic nepheline syenite gneiss from North Singhbhum Mobile Belt, eastern India. Mineral. Petrol. 107, 517–538.

Högdahl, K., Andersson, U.B., Eklund, O., 2004. The Transscandinavian Igneous Belt (TIB) in Sweden: a review of its character and evolution. Geological survey of Finland.

Johnsen, O., Ferraris, G., Gault, R.A., Grice, J.D., Kampf, A.R., Pekov, I. V, 2003. The nomenclature of eudialyte-group minerals. Can. Mineral. 41, 785–794.

Karup-Møller, S., Rose-Hansen, J., 2013. New data on eudialyte decomposition minerals from kakortokites and associated pegmatites of the Ilímaussaq complex, South Greenland. Geol. Soc. Denmark. Bull. 61, 47–70.

Karup-Møller, S., Rose-Hansen, J., Sørensen, H., 2010. Eudialyte decomposition minerals with new hitherto undescribed phases from the Ilímaussaq complex, South Greenland. Geol. Soc. Denmark. Bull. 58, 75–88.

Knittel, A., 2017. Experimentelle Untersuchungen der Phasenbeziehungen in peralkalinen Schmelzen der Norra Kärr Intrusion bei 1 kbar. Eberhard Karls Universität Tübingen.

Kogarko, L.N., 2015. Fractionation of zirconium in pyroxenes of alkaline magmas. Geochemistry Int. 53, 1–8.

Kogarko, L.N., 1990. Ore-forming potential of alkaline magmas. Lithos 26, 167–175.

Kogarko, L.N., 1987. Alkaline rocks of the eastern part of the Baltic Shield (Kola Peninsula). Geol. Soc. London, Spec. Publ. 30, 531–544.

Kogarko, L.N., Lazutkina, L.N., Romanchev, B.P., 1982. Problems of Genesis of Eudialyte Mineralization. Geokhimiya 1415–1432.

Marks, M., Halama, R., Wenzel, T., Markl, G., 2004. Trace element variations in clinopyroxene and amphibole from alkaline to peralkaline syenites and granites: implications for mineral–melt trace-element partitioning. Chem. Geol. 211, 185–215.

Marks, M.A.W., Coulson, I.M., Schilling, J., Jacob, D.E., Schmitt, A.K., Markl, G., 2008. The effect of titanite and other HFSE-rich mineral (Ti-bearing andradite, zircon, eudialyte) fractionation on the geochemical evolution of silicate melts. Chem. Geol. 257, 153–172.

Marks, M.A.W., Hettmann, K., Schilling, J., Frost, B.R., Markl, G., 2011. The mineralogical diversity of alkaline igneous rocks: critical factors for the transition from miaskitic to agpaitic phase assemblages. J. Petrol. 52, 439–455.

Marks, M.A.W., Markl, G., 2017. A global review on agpaitic rocks. Earth-Science Rev. 173, 229–258.

Marks, M.A.W., Markl, G., 2015. The Ilímaussaq alkaline complex, South Greenland, in: Layered Intrusions. Springer, pp. 649–691.

McLelland, J.M., 1989. Crustal growth associated with anorogenic, mid-Proterozoic anorthosite massifs in northeastern North America. Tectonophysics. https://doi.org/10.1016/0040-1951(89)90163-7

Mitchell, R.H., 2015. Primary and secondary niobium mineral deposits associated with carbonatites. Ore Geol. Rev. 64, 626–641.

Möller, C., Andersson, J., Lundqvist, I., Hellström, F., 2007. Linking deformation, migmatite

formation and zircon U–Pb geochronology in polymetamorphic orthogneisses, Sveconorwegian Province, Sweden. J. Metamorph. Geol. 25, 727–750.

Möller, V., Williams-Jones, A.E., 2017. Magmatic and Hydrothermal Controls on the Mineralogy of the Basal Zone, Nechalacho REE-Nb-Zr Deposit, Canada☼. Econ. Geol. 112, 1823–1856. https://doi.org/10.5382/econgeo.2017.4531

Möller, V., Williams-Jones, A.E., 2016. Petrogenesis of the Nechalacho Layered Suite, Canada: Magmatic Evolution of a REE–Nb-rich Nepheline Syenite Intrusion. J. Petrol. 57, 229–276.

Nanda, J., Gupta, S., Dobmeier, C.J., 2008. Metamorphism of the Koraput Alkaline Complex, Eastern Ghats Province, India—evidence for reworking of a granulite terrane. Precambrian Res. 165, 153–168.

Olivo, G.R., Williams-Jones, A.E., 1999. Hydrothermal REE-rich eudialyte from the Pilanesberg complex, South Africa. Can. Mineral. 37, 653–664.

Ovchinnikov, L.N., Solodov, N.A., 1980. Deposits of lithophile rare metals. Nedra, Moscow, 559p.

Pekov, I. V, 1998. Yttrium mineralization in the Khibiny–Lovozero alkaline complex (Kola Peninsula). Zap. VMO 5, 66–85.

Pfaff, K., Krumrei, T., Marks, M., Wenzel, T., Rudolf, T., Markl, G., 2008. Chemical and physical evolution of the 'lower layered sequence'from the nepheline syenitic Ilímaussaq intrusion, South Greenland: Implications for the origin of magmatic layering in peralkaline felsic liquids. Lithos 106, 280–296.

Pfaff, K., Wenzel, T., Schilling, J., Marks, M.A.W., Markl, G., 2010. A fast and easy-to-use approach to cation site assignment for eudialyte-group minerals. Neues Jahrb. für Mineral. J. Mineral. Geochemistry 187, 69–81.

Rankin, L.R., 2011. Structural setting of the Norra Kärr intrusive complex, Central Sweden. Geointerp Confidential Report 2011/14.

Rastsvetaeva, R.K., 2007. Structural mineralogy of the eudialyte group: A review. Crystallogr. Reports 52, 47–64. https://doi.org/10.1134/s1063774507010063

Salvi, S., Fontan, F., Monchoux, P., Williams-Jones, A.E., Moine, B., 2000. Hydrothermal mobilization of high field strength elements in alkaline igneous systems: evidence from the Tamazeght Complex (Morocco). Econ. Geol. 95, 559–576.

Schilling, Julian, Marks, M.A.W., Wenzel, T., Vennemann, T., Horváth, L., Tarassoff, P., Jacob, D.E., Markl, G., 2011. The magmatic to hydrothermal evolution of the intrusive mont saint-hilaire complex: Insights into the late-stage evolution of peralkaline rocks. J. Petrol. 52, 2147–2185.

Schilling, J, Wu, F.-Y., McCammon, C., Wenzel, T., Marks, M.A.W., Pfaff, K., Jacob, D.E., Markl, G., 2011. The compositional variability of eudialyte-group minerals. Mineral. Mag. 75, 87–115.

Short, M. , Apelt, T. , Moseley, G. , Mounde, M. , La Touche, G., 2015. Amended & Restated Prefeasibility Study - NI 43-101 - Technical report for the Norra Kärr Rare Earth Element Deposit prepared. Vancouver, Canada.

Sjöqvist, A.S.L., 2015. Agpaitic rocks of the Norra Kärr alkaline complex. Earth Sci. University of Gothenburg.

Sjöqvist, A.S.L., Cornell, D.H., Andersen, T., Andersson, U.B., Christensson, U.I., Ranjer, S.J.E., Holtstam, D., Leijd, M., 2014. Geochronology of the Norra Kärr alkaline complex, southern Sweden, in: 31st Nordic Geological Winter Meeting, Lund, Sweden.

Sjöqvist, A.S.L., Cornell, D.H., Andersen, T., Christensson, U.I., Berg, J.T., 2017. Magmatic age of rare-earth element and zirconium mineralisation at the Norra Kärr alkaline complex, southern Sweden, determined by U–Pb and Lu–Hf isotope analyses of metasomatic zircon and eudialyte. Lithos 294–295, 73–86. https://doi.org/10.1016/J.LITHOS.2017.09.023

Sjöqvist, A.S.L., Cornell, D.H., Andersen, T., Erambert, M., Ek, M., Leijd, M., 2013. Three compositional varieties of rare-earth element ore: eudialyte-group minerals from the Norra Kärr Alkaline Complex, Southern Sweden. Minerals 3, 94–120.

Smirnov, V.I., 1974. Ore deposits of the U.S.S.R. 3, 404–409.

Smith, M.P., Moore, K., Kavecsánszki, D., Finch, A.A., Kynicky, J., Wall, F., 2016. From mantle to critical zone: A review of large and giant sized deposits of the rare earth elements. Geosci. Front.

Söderlund, U., Möller, C., Andersson, J., Johansson, L., Whitehouse, M., 2002. Zircon geochronology in polymetamorphic gneisses in the Sveconorwegian orogen, SW Sweden: ion microprobe evidence for 1.46–1.42 and 0.98–0.96 Ga reworking. Precambrian Res. 113, 193–225.

Söderlund, U., Patchett, P.J., Vervoort, J.D., Isachsen, C.E., 2004. The 176 Lu decay constant determined by Lu–Hf and U–Pb isotope systematics of Precambrian mafic intrusions. Earth Planet. Sci. Lett. 219, 311–324.

Sørensen, H., 1992. Agpaitic nepheline syenites: a potential source of rare elements. Appl. Geochemistry 7, 417–427.

Sørensen, H., Bohse, H., Bailey, J.C., 2006. The origin and mode of emplacement of lujavrites in the Ilímaussaq alkaline complex, South Greenland. Lithos 91, 286–300. https://doi.org/10.1016/j.lithos.2006.03.021

Thomas Heinig, 2012. Lithological architecture of the Norra Kärr complex. Technical University Bergakademie Freiberg.

Törnebohm, A.E., 1906. Katapleiite-syenit, en nyupptäckt varietet af nefelinsyenit i Sverige. SGU Ser. C 1–54.

Upton, B.G.J., 2013. Tectono-magmatic evolution of the younger Gardar southern rift, South Greenland. Geol. Surv. Denmark Greenl. Bull.

von Eckermann, H., 1968. New contributions to the interpretation of the genesis of the Norra Kärr alkaline body in Southern Sweden. Lithos 1, 76–88.

Wahlgren, C.-H., Cruden, A.R., Stephens, M.B., 1994. Kinematics of a major fan-like structure in the eastern part of the Sveconorwegian orogen, Baltic Shield, south-central Sweden. Precambrian Res. 70, 67–91.

Wahlgren, C., Stephens, M.B., 2004. Tectonometamorphic reworking of TIB rocks during the Sveconorwegian orogeny, south-central Sweden. Spec. Pap. Surv. Finl. 37, 56.

Wood, B.J., Blundy, J.D., 1997. A predictive model for rare earth element partitioning between clinopyroxene and anhydrous silicate melt. Contrib. to Mineral. Petrol. 129, 166–181.

Woolley, A.R., Platt, R.G., Eby, G.N., 1996. Relatively Aluminous Alkali Pyroxene in Nepheline Syenite from Malawi. Can. Mineral. 34, 423–434.

Internet Reference List

Leading Edge Materials Corp., 2018; https://leadingedgematerials.com/norra-karr/; status: 29.04.2020

Appendix

Appendix A

The version of record Atanasova, P., Krause, J., Möckel, R., Osbahr, I., Gutzmer, J., 2015. Electron Probe Microanalysis of REE in Eudialyte Group Minerals: Challenges and Solutions. Microscopy and Microanalysis, 21(5), 1096-1113 © Microscopy Society of America 2015, published by Cambridge University Press is available online at: https://doi.org/10.1017/S1431927615000720 and doi:10.1017/S1431927615000720

Microsc. Microanal. 21, 1096–1113, 2015
doi:10.1017/S1431927615000720

Microscopy AND Microanalysis

Electron Probe Microanalysis of REE in Eudialyte Group Minerals: Challenges and Solutions*

Petya Atanasova,[1,*] Joachim Krause,[1] Robert Möckel,[1] Inga Osbahr,[1] and Jens Gutzmer[1,2]

[1]*Helmholtz-Zentrum Dresden—Rossendorf, Helmholtz Institute Freiberg for Resource Technology, Halsbruecker Str. 34, 09599 Freiberg, Saxony, Germany*
[2]*Department of Mineralogy, Technical University Bergakademie Freiberg, Brennhausgasse 14, D-09596 Freiberg, Saxony, Germany*

Abstract: Accurate quantification of the chemical composition of eudialyte group minerals (EGM) with the electron probe microanalyzer is complicated by both mineralogical and X-ray-specific challenges. These include structural and chemical variability, mutual interferences of X-ray lines, in particular of the rare earth elements, diffusive volatility of light anions and cations, and instability of EGM under the electron beam. A novel analytical approach has been developed to overcome these analytical challenges. The effect of diffusive volatility and beam damage is shown to be minimal when a square of $20 \times 20\,\mu$m is scanned with a beam diameter of $6\,\mu$m at the fastest possible speed, while measuring elements critical to electron beam exposure early in the measurement sequence. Appropriate reference materials are selected for calibration considering their volatile content and composition, and supplementary offline overlap correction is performed using individual calibration factors. Preliminary results indicate good agreement with data from laser ablation inductively coupled plasma mass spectrometry demonstrating that a quantitative mineral chemical analysis of EGM by electron probe microanalysis is possible once all the parameters mentioned above are accounted for.

Key words: rare earth elements, eudialyte, electron probe microanalyzer, beam conditions, diffusive volatility

Introduction

Eudialyte group minerals (EGM) are a compositionally complex group of silicates that may become an important source of heavy rare earth elements (HREE). Associated with other REE-bearing minerals, EGM occur in highly evolved magmatic complexes, so called agpaites, and represent the most important index minerals in such systems (Schilling et al., 2011). Heavy rare earth elements deposits hosted by alkaline complexes are commonly marked by a complex and highly unusual mineralogy. This poses particular challenges not only for beneficiation, but also for accurate analytical characterization. Eudialyte group minerals may incorporate significant concentrations of more than 30 different elements, including the group of 14 naturally occurring lanthanides and Y, where the light REE are commonly more abundant than the HREE. The work of several groups (e.g., Johnsen et al., 2003; Rastsvetaeva, 2007; Pfaff et al., 2010; Schilling et al., 2011) on the mineral composition of EGM led first to the proposal, and later the enhancement of a general formula for EGM by the Commission on New Minerals and Mineral Names of the International Mineralogical Association (IMA; Johnsen et al., 2003). This general formula is

$$[N1\,N2\,N3\,N4\,N5]_3[M1a\,M1b]_3 M2_{3-6} M3\,M4\,Z_3 [Si_{24}\,O_{72}]\theta_4\,X1\,X2,$$

with

$N(1–5)$ = Na, H_3O^+, K, Sr, REE, Ba, Mn, Ca;
$M1$ = Ca, Mn, REE, Fe, Na, Sr;
$M2$ = Fe, Mn, Na, Zr, Ta, Ti, Ba, H_3O^+;
$M(3–4)$ = Si, S, Nb, Ti, W, Na;
Z = Zr, Ti, Nb;
θ = O, OH, H_2O;
$X(1–2)$ = Cl, F, H_2O, OH, CO_3, SO_4, AlO_4, MnO_4.

This formula illustrates the inherent complexity of crystal structure and chemistry of the EGM, implying variable cation site occupation, the presence of vacancies, as well as the high, but variable, amount of volatiles, i.e. light cations and anions. Considering this complexity, it is not surprising that mineral chemical analyses often produce variable analytical results, in particular analytical totals far below 94 wt% (e.g., Coulson & Chambers, 1996; Johnsen & Gault, 1997; Olivo & Williams-Jones, 1999; Chakrabarty et al., 2012). This is true particularly for microanalysis using an electron probe microanalyzer (EPMA).

The most common analytical challenges in electron probe microanalyses include (1) the diffusive volatility of

Received January 20, 2015; accepted May 1, 2015
*Corresponding author. p.atanasova@hzdr.de

*This article is intended for the Special Issue from the EMAS 2014 Workshop on "Electron Probe Microanalysis of Materials Today – Rare and Noble Elements: from Ore Deposits to High-tech Materials".

light anions (e.g., F^- and Cl^-) and light cations (e.g., K^+ and Na^+), (2) the presence of nondetectable volatiles in the crystal structure, and (3) the occurrence of mutual interferences between the characteristic X-ray lines of major and trace elements, in particular of the REE (Pyle et al., 2002). In addition, the choice of (matrix-matched) reference materials for calibration, analytical detection limits, and the physical instability of EGM under the electron beam are fundamental factors influencing analytical precision.

Studies by Stormer et al. (1993) and Pyle et al. (2002) clearly illustrate the need for additional experimental analytical work and the systematic recording of (1) the behavior of light cations, anions and volatiles during electron beam exposure, and the subsequent effects of this behavior on the accurate estimation of all detectable major and minor elements, (2) the impact of the selected reference materials on the analytical results for major and minor elements and (3) the careful selection of X-ray lines for each element and the identification of background and peak positions devoid of mutual interferences.

The current study emphasizes the unique combination of different analytical approaches and methods essential for an assessment of the key parameters necessary for the careful optimization and performance of accurate quantitative analytical measurements of EGM with EPMA. It accentuates the great challenge of the continuous modification of the crystal lattice, molecular bonding, and elemental composition of the analyzed EGM, which occur during interaction with the electron beam. A set of experiments was designed to identify and evaluate the critical factors for quantification of the chemical composition of EGM. Furthermore, laser ablation inductively coupled plasma mass spectrometry (LA-ICP-MS) analyses are used to evaluate quality of the EPMA data. The proposed analytical protocol largely minimizes the analytical challenges mentioned above. It has been successfully tested on a variable suite of EGM from the Norra Kärr intrusion.

Materials and Methods

In order to avoid effects of the crystallographic orientation of the sample all experiments were performed on a single crystal. A coarse-grained sample (NKA 5408) was selected from drill core NKA11054 from the Norra Kärr alkaline complex, Southern Sweden. For all experiments polished thin and thick sections of a ca. 10×10 mm euhedral eudialyte single crystal were prepared and used (see Figs. 1a–1d). Earlier investigations by Sjöqvist et al. (2013) and Atanasova et al. (2013) illustrate EGM crystals from Norra Kärr to be complexly zoned. For the present study, the areas with the smallest compositional variability of the crystal were identified by optical microscopy and EPMA element distribution mappings of major (e.g., Zr, Si, Al) and minor (e.g., Ce, Y) elements. Three zones of similar chemical composition were

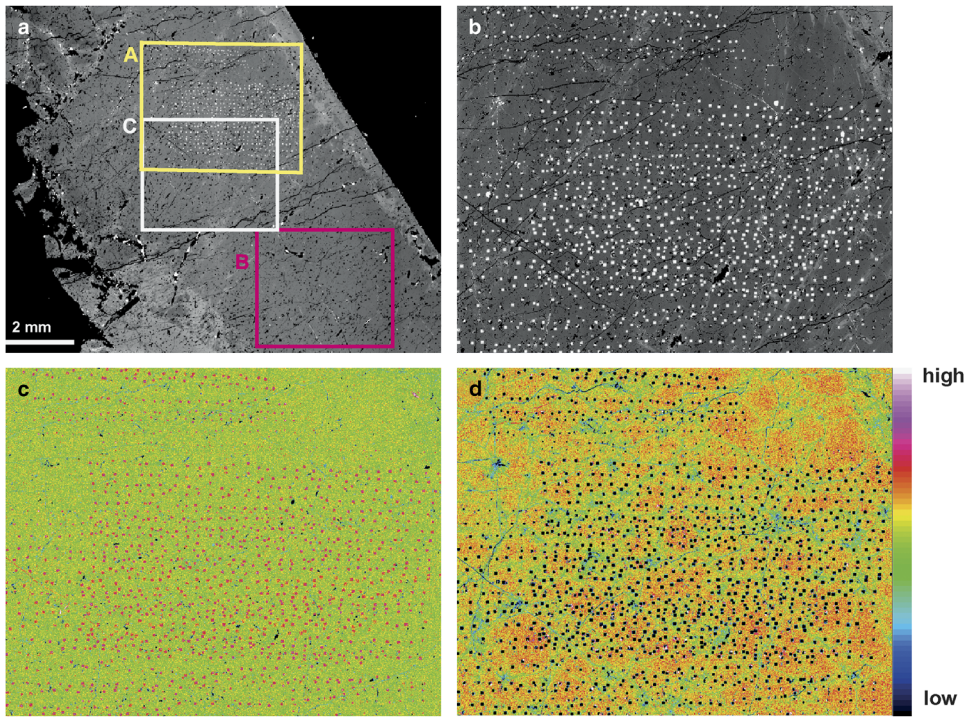

Figure 1. **a**: Electron probe microanalyzer (EPMA) compositional (BSE) image of the single euhedral eudialyte crystal (sample NKA 5408) used for all measurements illustrating the selected areas A, B, and C for beam condition experiments. **b**: BSE enlarged image of area A illustrating small compositional variations and the selected points for quantitative measurements. **c**: Si and (**d**) Na element distribution maps of area A showing Si increase and Na decrease after measurement, respectively.

selected to place points for quantitative analyses (Figs. 1a–1d and Supplementary Figs. 1–3).

Supplementary Figures 1–3

Supplementary Figures 1–3 can be found online. Please visit journals.cambridge.org/jid_MAM.

Instrumentation

Besides EPMA, the results of thermogravimetric analysis coupled to mass spectrometry (TG-MS) were used to determine the content of volatiles in the sample and to identify individual volatile species. LA-ICP-MS was applied to determine the concentration of REE in the EGM—in order to validate EPMA data.

EPMA

Measurements were performed with a JEOL JXA 8530F (JEOL Ltd, Tokio, Japan) at the Helmholtz-Institute Freiberg for Resource Technology. The system is equipped with a field emission electron gun and five wavelength dispersive spectrometers (WDS). Two of these spectrometers are provided with H-type crystals for high sensitivity and one with L-type crystals for elevated sensitivity combined with good energy resolution.

X-ray element distribution maps were acquired with an acceleration voltage of 20 kV, a beam current of 50 nA, beam diameter of 14 μm, and a dwell time of 140 ms. Aluminum, Y, Nd, Cl, and Ce were measured using the WDS, while Si, K, Ca, Mn, Zr, and Fe were measured with an energy dispersive spectrometer (EDS) in order to avoid multiple cycles of measurement on the WDS and save instrument time. Area A (Figs. 1a–1d, Supplementary Fig. 1) was additionally mapped for Na, Zr, Si, Ca, and Mn using the WDS.

In order to identify the elements relevant for a particular set of samples, qualitative X-ray analysis and additional EDX spectra were collected and evaluated. In the case of the Norra Kärr samples, the major elements Si, Al, Na, K, Ca, Fe, Mn, and Zr, the minor elements Hf, Nb, Cl, F, Y and the group of 14 REE, as well as the trace elements Ti and S were identified as relevant. Phosphorous was only measured for the calculation of an offline overlap correction measuring REE-orthophosphates and to monitor the instrumental drift for REE during analysis using monazite from Astimex Standards Ltd. (Astimex Standards Ltd, Toronto ON, Canada) (standard holder MINM 25–53, serial IK). For the detection of all 30 elements, five different analyzer crystals TAP, PETH, LIFL, LIFH, and LDE1 and all five spectrometers were used. Assignment of the analyzed elements to detector crystals and spectrometers is shown in Table 1. All quantitative analyses were performed at an accelerating voltage of 20 kV and a beam current of 20 nA. Since the chief aim of this paper is to establish a new analytical protocol for analysis of REE in EGM, a complete list of the specific settings for every element is given in Table 8.

TG-MS

Thermogravimetric analyses were conducted using a Netzsch STA 409 CD device (Erich NETZSCH GmbH & Co. Holding KG, Germany), coupled directly to a mass spectrometer. The sample material was handpicked (from sample NKA 5408) and ground in an agate mortar to a particle size <0.3 mm. A small amount of 26 mg was heated in an Al_2O_3 crucible up to 1450°C under vacuum conditions. The heating rate was kept constant at 10 K/min. Mass–charge ratios (m/z) of evaporating volatiles were detected with 100 ms per step for m/z 1–100.

LA-ICP-MS

The measurements were performed on a 193 nm Photon Machines Analyte G2 excimer laser ablation system coupled to a Thermo Finnigan Element 2 sector field ICP-MS at the Institute for Mineralogy of the Westfälische Wilhelms-Universität Münster, Germany. A frequency of 10 Hz and a spot size of 40 μm were used. Helium was used as the carrier gas. The ablated material was analyzed in the ICP-MS in low-resolution mode with a counting time of 20 s on the background and 50 s on the sample. NIST612-glass was used for calibration of the instrument and quantification of the measured intensities. KL2-G and GOR132-G glasses were used to monitor instrumental drift and quality of the analysis. Data reduction was performed using a programmed Microsoft Excel spreadsheet. Blank-corrected count rates were calculated relative to the internal standard (^{29}Si) in

Table 1. Assignment of Analyzed Elements to Detector Crystals and Spectrometers.

Order	Channel 1	Channel 2	Channel 3	Channel 4	Channel 5
1	Na Ka1,2 TAP	Si Ka1,2 TAP	Ho Lb1 LIFL	Cl Ka1 PETH	Tm La1 LIFH
2	F Ka1,2 LDE1	Zr La1,2 TAP	Yb La1 LIFL	K Ka1 PETH	Er La1 LIFH
3	Hf Ma TAP	Nb La1,2 TAP	Dy Lb1 LIFL	Ca Ka1 PETH	Fe Ka1 LIFH
4	Al Ka1,2 TAP	Y La1,2 TAP	Sm Lb1 LIFL	Ti Ka1 PETH	Mn Ka1 LIFH
5			Gd La1 LIFL	Lu Lb1 LIFH	Pr Lb1 LIFH
6			Eu La1 LIFL	Tb La1 LIFH	Ce La1 LIFH
7			Nd Lb1 LIFL	S Ka1 PETH	La La1 LIFH
8				P Ka1 PETH	

order to compensate for the intensity decrease during ablation. The Excel routine also rejects obvious outliers. The detection limit was between 0.2 and 2.0 μg/g for REE and 10 μg/g for Y. Details of the analytical procedure may be found in Jochum et al. (2006, 2007).

Experimental Setup for EPMA

In order to define the most appropriate beam conditions for the measurements a total of 101 experiments were performed. The settings chosen resulted in a measurement time of 814 s per analysis. Furthermore, available reference materials were tested for the correction of major elements.

Beam Conditions

At the beginning, experiments 1a–g (Table 2) were performed with the intent to characterize and visualize the change in X-ray intensity over the time of the measurements. X-ray intensities were measured for 28 elements, excluding P and S. The latter were considered to be of minor importance. The results were used to define five elements for further tests at different beam diameters and scan speed settings, while scanning a rectangular area of 40 by 20 μm in x and y. In this particular case, the X-ray signals on the WDS spectrometers and the probe current were measured, while the secondary electron image was recorded with a magnification of 3,500 times. The extent of 40 μm in the x direction is too large to match Braggs' law over the entire scanned surface for some elements (e.g., Si) leading to lower count rates compared with the round beam of 20 μm diameter.

The experimental results were used to define different measurement sequences and to identify suitable beam settings for further experiments, investigating analytical precision. For this purpose, four main variables were defined, namely beam mode, beam diameter, edge length of scanned square and scanning speed. Thirty different setups (listed in Table 3) combining the four variables were chosen to be most representative. Two different beam modes were compared, steady mode (eight experiments), a continuous irradiation of the sample by a round beam and scanning mode (22 experiments), where a square with a defined edge length is scanned by the beam. Since these experiments were performed as a quantitative analysis, the scanned area has the shape of a square.

In scanning mode, beam diameters between <0.06 μm (focused beam) and 6 μm (experiments 12–18, Table 3), and edge lengths between 8 and 26 μm, in 3 μm steps (experiments 1–11, Table 3) were conducted. The effect of different scan speed settings was tested for a square with an edge length of 20 μm (experiments 9 and 18–22; Table 3). In steady mode, beam diameters between 5 and 26 μm (experiments 23–30, Table 3), in 3 μm steps were tested. Previous tests had resulted in extreme damage to the sample when diameters smaller than 5 µm were chosen.

Repeatability was ensured by conducting 30 measurements for each of the 30 settings, that is, 900 measurements in total. All 900 measurements were repeated for the measurement sequences A, B, and C (Table 4).

Reference Materials

One of the most important aspects for quantification of the chemical composition of a sample with EPMA is the use of appropriate reference materials to calibrate peak position and intensity for each element. As suggested by Pyle et al. (2002), the synthetic Smithsonian orthophosphate standards (USNM 168484 to USNM 168499, Jarosewich & Boatner, 1991) were used for the calibration of Y and all REE, except Gd. For all other elements, certified reference materials from Astimex Standards Ltd. (standard holder MINM 25–53,

Table 2. Experimental Setup "X-ray Intensity".

Experiment	Elements Tested	Area Shape	Scanning	Beam Diameter (μm)	Scan Speed Settings
1a	Na, Si, Ho, K, Tm	Round	No	20	na
1b	F, Hf, Yb, Ca, Er	Round	No	20	na
1c	Y, Zr, Dy, Ti, Fe	Round	No	20	na
1d	Al, Nb, Gd, Lu, Mn	Round	No	20	na
1e	Na, Si, Eu, Tb, Pr	Round	No	20	na
1f	Na, Si, Sm, Cl, Ce	Round	No	20	na
1g	Na, Si, Nd, K, La	Round	No	20	na
2	Na, Si, Dy, Ca, Ce	Rectangular	Yes	<0.06 (focused)	1
3	Na, Si, Dy, Ca, Ce	Rectangular	Yes	1	1
4	Na, Si, Dy, Ca, Ce	Rectangular	Yes	1	3
5	Na, Si, Dy, Ca, Ce	Rectangular	Yes	1	6
6	Na, Si, Dy, Ca, Ce	Rectangular	Yes	1	10
7	Na, Si, Dy, Ca, Ce	Rectangular	Yes	2	1
8	Na, Si, Dy, Ca, Ce	Rectangular	Yes	3	1
9	Na, Si, Dy, Ca, Ce	Rectangular	Yes	4	1
10	Na, Si, Dy, Ca, Ce	Rectangular	Yes	5	1
11	Na, Si, Dy, Ca, Ce	Rectangular	Yes	6	1

na, not applicable.

Table 3. Experimental Setup "Beam Conditions".

Nr	Beam Mode, Area Shape	Beam Diameter (μm)	Edge Length of Square (μm)	Scan Speed Settings
1	Scanning, square	3	8	1
2	Scanning, square	3	11	1
3	Scanning, square	3	14	1
4	Scanning, square	3	17	1
5	Scanning, square	3	20	1
6	Scanning, square	3	23	1
7	Scanning, square	3	26	1
8	Scanning, square	6	17	1
9	Scanning, square	6	20	1
10	Scanning, square	6	23	1
11	Scanning, square	6	26	1
12	Scanning, square	0	20	1
13	Scanning, square	1	20	1
14	Scanning, square	2	20	1
15	Scanning, square	3	20	1
16	Scanning, square	4	20	1
17	Scanning, square	5	20	1
18	Scanning, square	6	20	2
19	Scanning, square	6	20	3
20	Scanning, square	6	20	5
21	Scanning, square	6	20	7
22	Scanning, square	6	20	9
23	Steady, round	5	na	na
24	Steady, round	8	na	na
25	Steady, round	11	na	na
26	Steady, round	14	na	na
27	Steady, round	17	na	na
28	Steady, round	20	na	na
29	Steady, round	23	na	na
30	Steady, round	26	na	na

na, not applicable.

serial IK and standard holder METM 25–44, serial NC) were used. The influence of reference materials on the quantification of the concentration of a specific element was studied by calibrating the X-ray intensities for the major elements Na, Si, Ca, Mn, Fe, and Zr on a number of available reference materials. A single spot analysis AB23 (sample 5408) was offline-corrected using all available calibrations (Table 5 and Supplementary Appendix 2).

Supplementary Appendix 2. Supplementary Appendix 2 can be found online. Please visit journals.cambridge.org/jid_MAM.

Interferences

In order to assess the extent of mutual interferences, spectra for all elements present in the measurement sequence were acquired, preferentially on pure element reference materials. A detailed comparison of the spectra acquired in this manner allowed for the identification of optimal positions for measurements of peaks and background.

Results

In order to resemble the actual setup of an analytical protocol for the EPMA, results are presented in a sequence starting with the beam conditions followed by the selection of appropriate reference materials for calibration, and offline interference correction at the end. The complete set of experimental data acquired is given in the appendices.

Experimental Setup "X-ray Intensity"

The change in X-ray intensity was calculated (in relative percent (%)) in relation to the initial value, as an average of the first and last 20 s for every experiment (see Supplementary Appendix 1). For experiments 1a–g, the strongest dependence of the measured X-ray intensity on irradiation with time was recorded for Na (up to 95% relative decrease in signal). A continuous rise of X-ray intensity of up to 14% for Si and ~5–8% for most of the other major elements, namely Ca, Zr, Mn, and Fe, as well as the minor elements Hf, Y, Ti, Nb, and Cl was noted (Supplementary Appendix 1). Repeated measurements (experiments 1e–g, Table 2) of apparent Na and Si intensities support these observations. Although

Table 4. Experimental Setup "Elemental Sequence".

		Start of Measurement after Start of Analysis (s)		
Spectrometer	Element	Sequence A	Sequence B	Sequence C
1	Na	0	120	360
1	F	15	135	300
1	Hf	75	195	120
1	Al	255	0	0
2	Si	0	120	345
2	Zr	30	150	300
2	Nb	75	195	120
2	Y	255	0	0
3	Ho	0	315	540
3	Yb	120	435	465
3	Dy	195	510	390
3	Sm	270	585	315
3	Gd	345	0	240
3	Eu	420	75	60
3	Nd	600	255	0
4	Cl	0	465	585
4	K	60	525	645
4	Ca	90	555	540
4	Ti	135	600	465
4	Lu	210	285	285
4	Tb	390	0	105
4	S	570	180	30
4	P	645	255	0
5	Tm	0	300	450
5	Er	180	480	375
5	Fe	255	555	300
5	Mn	330	0	225
5	Pr	405	75	150
5	Ce	480	150	75
5	La	555	225	0

the detected signals for all elements of the REE group appear noisy, numerical values for most of the REE (e.g., Ce, Nd, Gd, Dy) hint at a small, but detectable increase in X-ray intensity during measurement. Due to very low count rates for all remaining elements, a clear trend cannot be observed. The recorded probe current showed a slight decrease from 1.70 $\times 10^{-8}$ to 1.68 $\times 10^{-8}$ A (more details are given in Supplementary Appendix 1).

Supplementary Appendix 1

Supplementary Appendix 1 can be found online. Please visit journals.cambridge.org/jid_MAM.

Results of the experimental setup "X-ray intensity" were used to define the order in which elements are measured in the sequence, in order to minimize the effects of signal changes over time, especially for the elements most sensitive to beam exposure, in particular Na, K, Si, F, and Cl. The resulting optimized measurement sequence A is listed in Table 4. In addition, five elements were selected for further testing: Na for its observed sensitivity to the electron beam, Si as the most abundant element in the EGM, Ca as an indicator for the other major elements, and Ce and Dy as representatives for the REE.

Table 5. Tested Reference Materials.

Reference Material	Si	Na	Ca	Fe	Mn	Zr
Albite_AST	+	+				
Orthoclase_AST	+					
Tugtupite_AST	+	+				
Pyrope_AST	+					
Obsidian_AST	+					
Cr-Diopside_AST	+					
Bustamite_AST	+		+	+	+	
Almandine_AST	+			+		
Diopside_AST	+		+			
Rhodonite_AST	+				+	
Jadeite_AST	+	+				
Spodumene_AST	+					
Olivine_AST	+			+		
Kaersutite_AST	+		+	+		
Plagioclase_AST	+		+			
Pollucite_AST	+					
Willemite_AST	+					
Chlorite_AST	+					
Hematite_AST				+		
Magnetite_AST				+		
Zirconia_AST						+
Zr-AST						+

The effect of beam diameter on the X-ray intensity of Na scanning a rectangular area is illustrated in Figure 2b. A general decrease in signal is apparent for every experiment. However, the decrease in intensity is less pronounced with increasing beam size and scan speed settings, achieving the best result of ~40% using the fastest possible scan speed setting 1 and a beam diameter of 6 μm. Additionally, compared with the application of a round, steady beam, a more stable signal was observed for about the first 100 s (see Fig. 2b).

For Si and Ca, similar to Na, a general, but smaller and later change in X-ray intensity is observed for every experiment. An increase of 3% for Si (Fig. 2a) and <1% for Ca (Supplementary Appendix 1) at a beam diameter of 6 μm is recorded. Due to low count rates, variations in the X-ray intensities of Ce and Dy fluctuated strongly and therefore results for both elements are not further discussed. The probe current decreased by between 0.3 and 1.0%.

Experimental Setup "Beam Conditions"

Obvious outliers caused by known physical reasons, such as the occurrence of inclusions, fractures, holes, polishing, or coating effects were rejected from the dataset. A general decrease in surface damage with increasing beam diameter

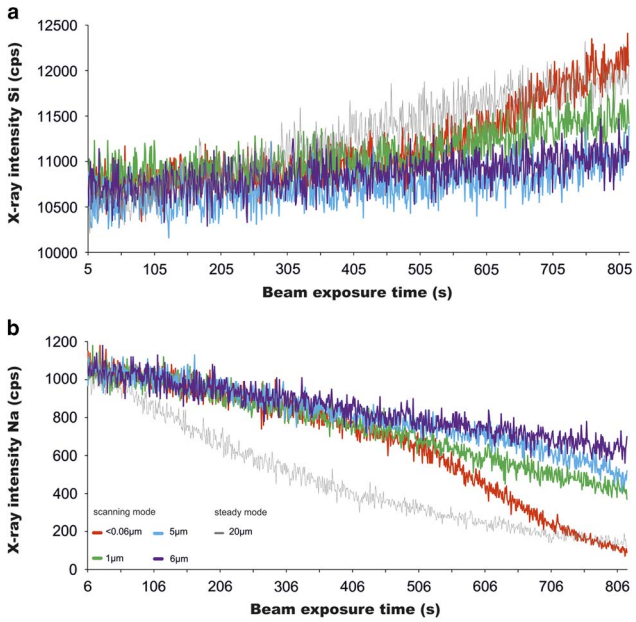

Figure 2. Diagram illustrates the change of (**a**) Si and (**b**) Na X-ray intensity over time. It is obvious that the apparent diffusive volatility of Na and the accurate quantification of Si are both affected by the measurement mode and the beam diameter used.

and size of the scanned area was monitored, with a significant advantage applying the scanning mode (see Fig. 3b).

In steady mode (round beam), the results of eight experiments (performed 30 times each) clearly illustrated a direct correlation between beam diameter and calculated analytical total. In particular, an increase in analytical totals of up to 3 wt% (from ~94.5 wt% at 26 μm up to 97.5 wt% at 5 μm, Supplementary Appendix 1) was observed with decreasing size of beam diameter. For elements measured early in the sequence (e.g., Na and Si), a remarkable consistency (variations below one wt%) for beam diameters between 11 and 26 μm was noted. For beam diameters from 5 to 8 μm, an obvious shift towards higher concentrations for SiO_2 and lower concentrations for Na_2O was observed (see Figs. 4a, 4b). Concentrations for CaO, K_2O, Nb_2O_5, Yb_2O_3, and Dy_2O_3 measured in the middle of the sequence increased by ca. 5–10 % (relative) when decreasing the beam diameter (Supplementary Appendix 1). Major and minor element oxides such as Y_2O_3, FeO, MnO, and Ce_2O_3, measured late in the sequence (after 255 s), were significantly affected by a continuous increase in concentration (ca. 10–15 %) with decreasing beam diameter. The concentrations of all other detected elements are too low to identify a trend outside the analytical uncertainty.

In scanning mode, the dataset clearly illustrates the significance of the size of the scanned area on the analytical result, in particular for edge lengths up to 14 μm. Reduction of the scanned area size yielded increasing analytical totals of up to 1 wt% (Fig. 5c) reflecting the increase in X-ray intensity of major and minor elements as described above (Figs. 2a, 2b and Figs. 5a, 5b). Even the SiO_2 concentration, measured very early in the sequence (see Fig. 2a) was found to be controlled by area size showing values of up to 51 wt% for edge lengths 8–11 μm compared with a maximum of 50.3 wt% for edge lengths larger than 14 μm (Fig. 5b). Similar observations were made for almost all major and minor elements (more detailed data in Supplementary Appendix 1), though the elemental order in the measurement sequence remains the most important parameter controlling the extent of such variations. Sodium showed increasing concentrations by increasing size of analyzed area (Fig. 5a).

The effect of the size of scanned area on the analytical result becomes less apparent for scanned squares with edge lengths ≥17 μm (see Fig. 5c). The effects of beam size and scan speed settings are negligible for all experiments in scanning mode (Supplementary Appendix 1).

Experimental Setup "Elemental Sequence"

The experimental setup "beam conditions" (Table 3) was applied for two alternative measurement sequences B and C (see Table 4). Elements critical to beam exposure (as defined above) were intentionally placed later in the measurement sequence and results were compared with results from measurement sequence A. Exemplary plots of results for Na_2O and SiO_2 and the analytical total are presented in Figures 6A(a)–6A(c) and Figures 6B(a)–6B(c). All other results are included in Supplementary Appendix 1.

For both modes, the variation in concentrations within sequences B and C became more distinct compared with the results for sequence A, with Na_2O concentrations below 0.3 wt% and SiO_2 contents of up to ca. 60 wt%. Nevertheless, the observed variations still follow the same trends as in measurement sequence A.

In contrast, considering the data for the analytical totals, there is a clear difference in the observed patterns. The totals for B and C in steady mode inverted at a diameter of 11 and 17 μm, respectively, and increased (Fig. 6A(c)). Similarly, in scanning mode, results for the analytical totals for the measurement sequences B and C differed both from each other and from the results for measurement sequence A (Fig. 6B(c)). While the analytical totals for measurement sequence A continuously (almost linear) decreased with increasing size of area, the results for measurement sequence B showed the opposite trend. In contrast to both almost linear patterns, results for the analytical totals for measurement sequence C showed a complex pattern, with decreasing values from 5–17 μm edge length and increasing values for edge lengths of 20–26 μm.

Volatiles

As shown in Figure 7, the total loss of volatiles during heating amounts to about 3.3 wt% of the eudialyte sample NKA 5408. Two main degassing temperatures could be distinguished: at around 250–300°C and 450–700°C. These temperature ranges correspond well to the signal of

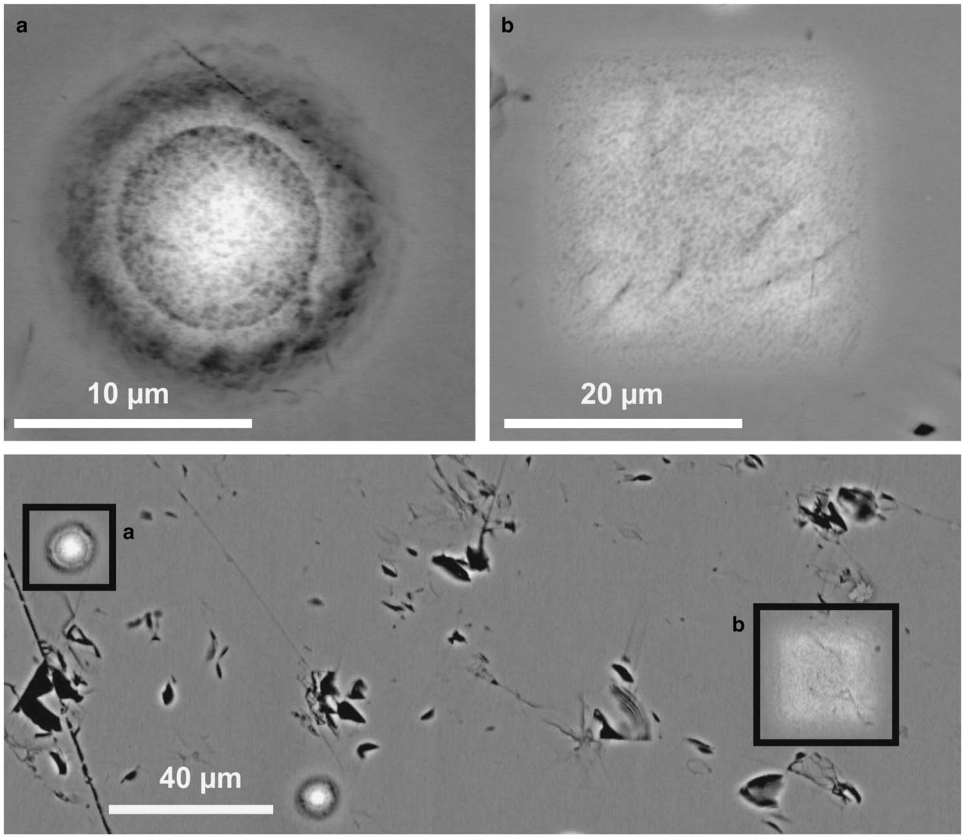

Figure 3. Crystal damage of eudialyte after exposition to the electron beam in (**a**) steady mode and (**b**) scanning mode for 814 s.

$m/z = 18$ (H_2O), with main peaks at 280 and 550°C, respectively (see Fig. 7). Minor signals were also detected at higher temperatures (around 1050°C) at $m/z = 32$–36, 38, 48–50, 64, 65, 66, all of which correspond to sulfur and sulfur compounds/fragments and $m/z = 44$, 45 (CO_2). No evidence for other compounds was found in the mass spectra. The presence of sulfur is in accordance with EPMA findings (Supplementary Appendices 1 and 3).

Supplementary Appendix 3

Supplementary Appendix 3 can be found online. Please visit journals.cambridge.org/jid_MAM.

Reference Materials

Depending on the reference material chosen for calibration, calculated SiO_2 contents for a given analysis varied over a range of more than 10 wt% (48.78–58.95 wt% using Pyrope_AST and Chlorite_AST, respectively, see Fig. 8). Consequently, the analytical totals also varied between 94.94 and 105.43 wt%. For the other major elements tested the differences were smaller [(Na_2O = 12.00 wt% using Tugtupite_AST to 12.53 wt% using Albite_AST; CaO = 6.71 wt% for Plagioclase_AST to 6.92 wt% for Kaersutite_AST; FeO = 2.33 wt% for Magnetite_AST to 2.55 wt% for Kaersutite_AST (see Supplementary Appendix 2)]. For MnO and ZrO_2, only insignificant differences were observed when using different reference materials (data given in Supplementary Appendix 2).

Interferences and their Corrections

When analyzing EGM, the high number of elements contained in detectable concentrations results in many peak–background and peak–peak overlaps. This is particularly true for the REE (Figs. 9a–9c). The measurement program for EGM developed in this study includes 30 elements, resulting in 51 peak–peak overlaps (Table 6). Peak–background overlaps were avoided by careful selection of the spectrometer positions for peak and background for each element. For Na, Hf, Zr, Nb, Y, Yb, Gd, Lu, Tm, Er, Fe, Pr, Tb, and S, only one background was measured due to unavoidable interferences on the other background position. If peak–peak overlaps cannot be avoided by the selection of another X-ray line (e.g., NdLβ1 instead of NdLα1), an overlap correction is necessary. The correction applied is an offline overlap correction approach, which combines a ZAF matrix correction and a subsequent offline interference correction with calculated overlap factors (Table 6). The general procedure for this offline overlap correction is to measure the reference materials for each element (five analyses on each) after the calibration for peak positions and intensity, but before the sample analyses, and to determine overlap factors based on the proportion of the resulting weight percent of

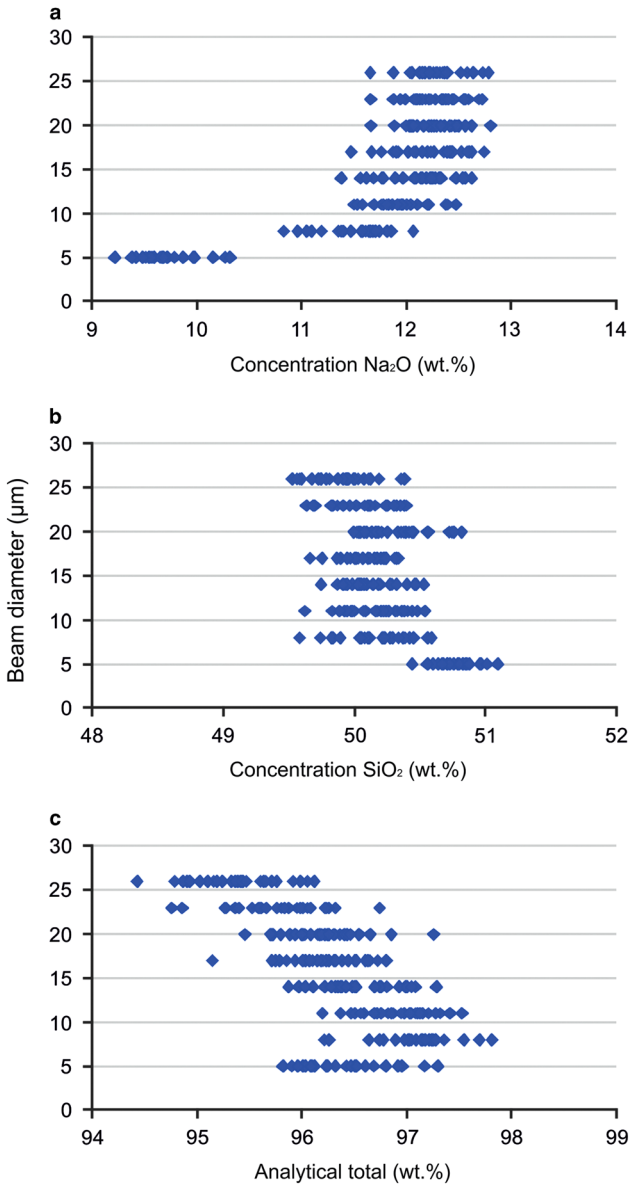

Figure 4. Variations in (**a**) Na_2O and (**b**) SiO_2 concentrations (ZAF corrected) as well as in (**c**) calculated analytical totals for different beam size diameters in steady mode.

overlapping elements. This offline overlap correction and the determination of the overlap factors are described in detail for the correction of platinum group elements in Osbahr et al. (2015, this issue). Additional qualitative work is required for Sr- and Ba-rich varieties of EGM to explore potential interferences.

The high relative standard deviation >10% for the calculated overlap factors for KKα2 on HfMα (51.7%), TmMα on AlKα1,2 (22.75%), LuMβ on HfMα (21.8%) or FeKα2 on SmLβ1 (15.7%) show that the factors vary strongly for each calibration (Table 6). This results from shifts of flank positions of overlapping peaks as even slight changes in the peak position will have a strong effect on the count rate (Figs. 9b, 9c).

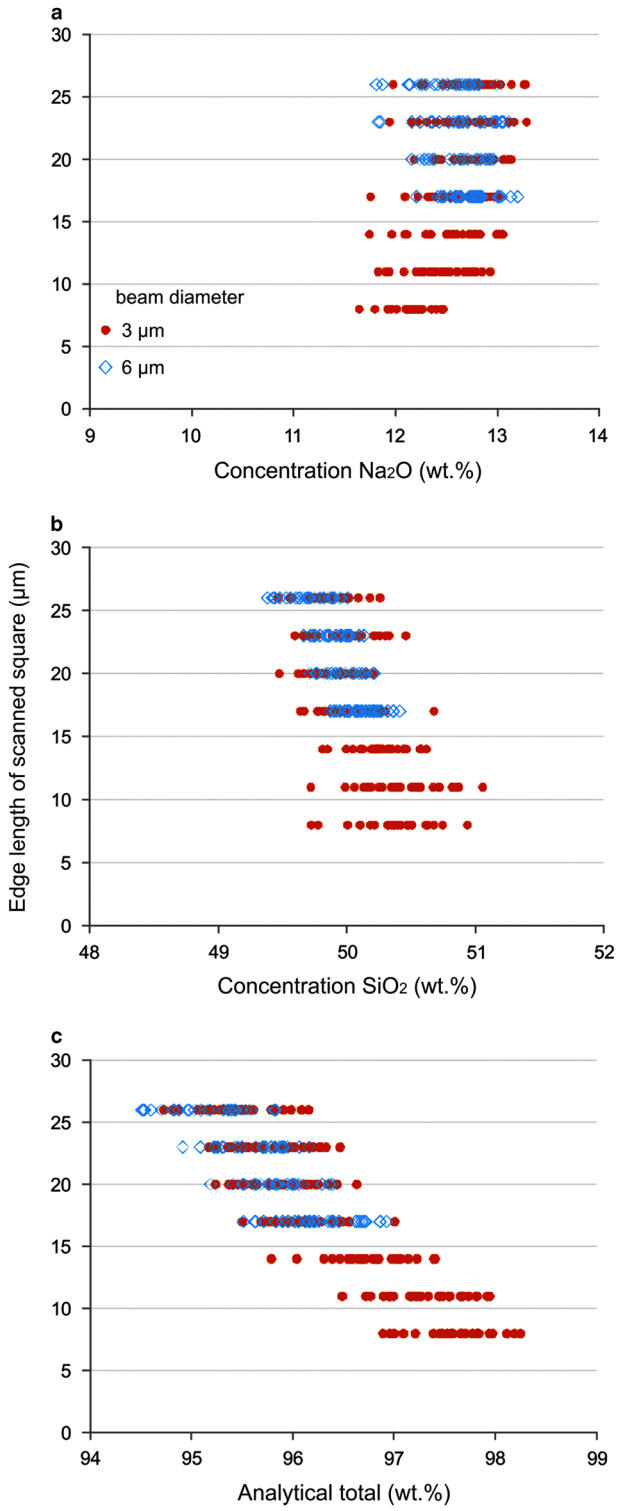

Figure 5. ZAF-corrected concentrations for (**a**) Na_2O and (**b**) SiO_2 and (**c**) calculated analytical totals for different edge lengths and beam diameters in scanning mode.

LA-ICP-MS data

The relative difference in concentration between the two applied methods, EPMA (raw data) and LA-ICP-MS and the effect of subsequent offline overlap correction on the EPMA

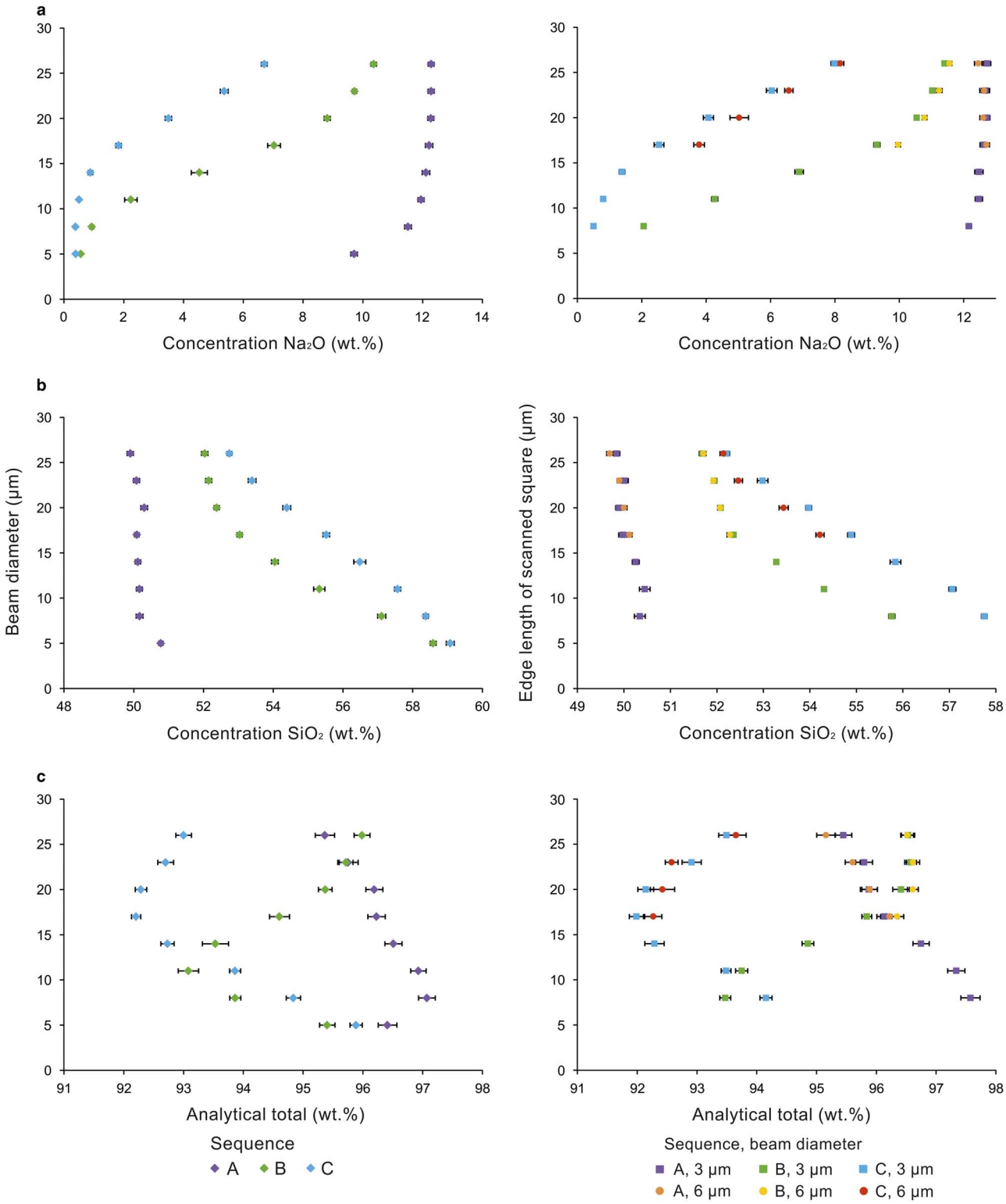

Figure 6. In **A**: steady and **B**: scanning mode (**a**) Na_2O, (**b**) SiO_2 and (**c**) the analytical totals are used to illustrate the effects of the elemental order in a particular measurement sequence (here A, B and C) with respect to beam diameter and to size of scanned square in scanning mode. Illustrated are mean values and the corresponding confidence intervals (CI) of the mean.

data (corr) is visualized in the logarithmic plot Figure 10a. A logarithmic scale is chosen in order to adequately display the confidence intervals (CI) of the calculated mean of the 21 concentration differences (21 spots measured) per element. Results used for comparison are listed in Table 7. LA-ICP-MS results show low standard deviation values for

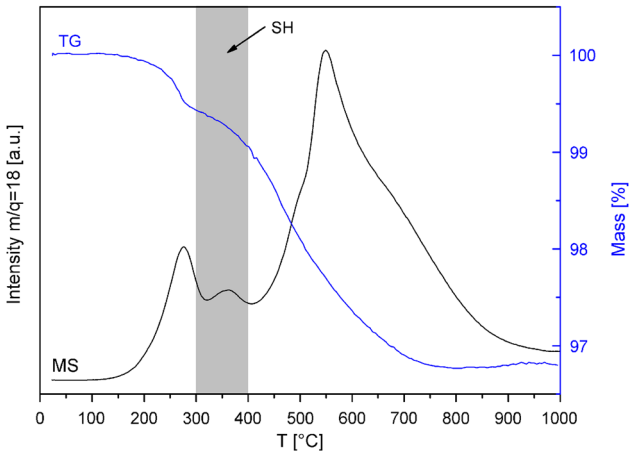

Figure 7. Thermogravimetric analysis (TG) and thermogravimetric analysis coupled to mass spectrometry (TG-MS) data for fragments of the eudialyte crystal investigated (for $m/q = 18$, which is the main mass–charge ratio for water). There are two main water degassing peaks at around 280 and 550°C, respectively. The overall mass loss around 3.3 wt% is predominantly due to the loss of water. Note that MS spectra are recorded under vacuum condition; the TG-curve was recorded in an Ar-atmosphere. SH indicates temperature range of specimen heating by the electron beam.

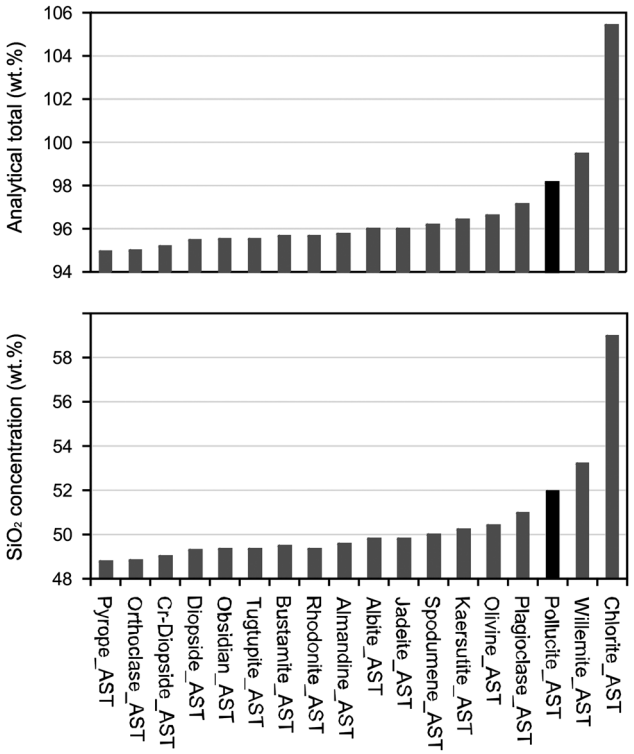

Figure 8. Values for the analytical total and the SiO_2 content for the selected eudialyte analysis using different reference materials for silicon. Pollucite is identified to be the most appropriate reference material for Si.

all elements. In contrast, EPMA results for Eu, Tb, Ho and Tm show certain variability, which is also reflected in wider confidence intervals. While Ce, Pr, Nd, Ho, and corrected Gd concentrations obtained with both methods agree within the analytical errors, all other elements show significant differences between the results acquired (Fig. 10a). However, these differences, in particular for La, Dy, Er and for Sm, Y and Yb only account for ~15 and 20%, respectively. Differences for Eu, Tb, and Tm are more significant. A comparison of normalized REE and Y concentrations obtained by both methods is illustrated in Figure 10b.

Discussion

In order to minimize crystal damage several experimental setups are evaluated. Experiments are not only chosen to best characterize the instability of EGM under the electron beam, but also to determine the optimal conditions for all measurement routines.

Beam Conditions

The results of 2711 measurements at various beam conditions (as listed above) clearly show X-ray intensity variations over time for almost all elements measured. A significant decrease in Na intensity is recognized during the first seconds of measurement (Fig. 2b). This especially makes the detection of Na an exacting procedure. However, the latter problem may be solved by early detection of Na at the beginning of the measurement sequence and short measurement times on peak and background as already proposed by Andersen et al. (2010) and Pfaff et al. (2008). Strongly affected are also the major elements Si, Ca, Zr, K, Mn, and Fe, as well as the minor elements Y, Nb, and Ti, whose signal intensities notably increase over the time of measurement (see Fig. 2a and Supplementary Appendix 1). At first glance, the decrease in Na intensity and the increase in signals for Si and other major elements are simultaneous indicating a direct influence of the diffusive volatility of Na on the behavior of other elements (Figs. 2a, 2b). However, in fact this increase in signals for Si and the other major elements is postponed if compared with the decrease of Na signal, indicating that other processes are also involved. These could include a change in crystal structure or a transformation into an amorphous phase.

The highly volatile element Cl shows increasing signal intensity over time despite the majority of observations made by Stormer et al. (1993), who indicated a decline in F and Cl intensities in apatite after a longer period of exposure to the electron beam. Though, the same study also provides indications that anisotropy of diffusion and hence a dependency of the crystallographic orientation of the sample as observed for apatite may cause an increase in intensities of F and Cl due to diffusion to sites near the surface of the sample. All measurements for the present study were performed on a single crystal in order to avoid a variable influence of this effect on the results.

As illustrated by the current study, the diffusive volatility of Na, as well as the X-ray intensity variations of many other elements, strongly depend on beam diameter and

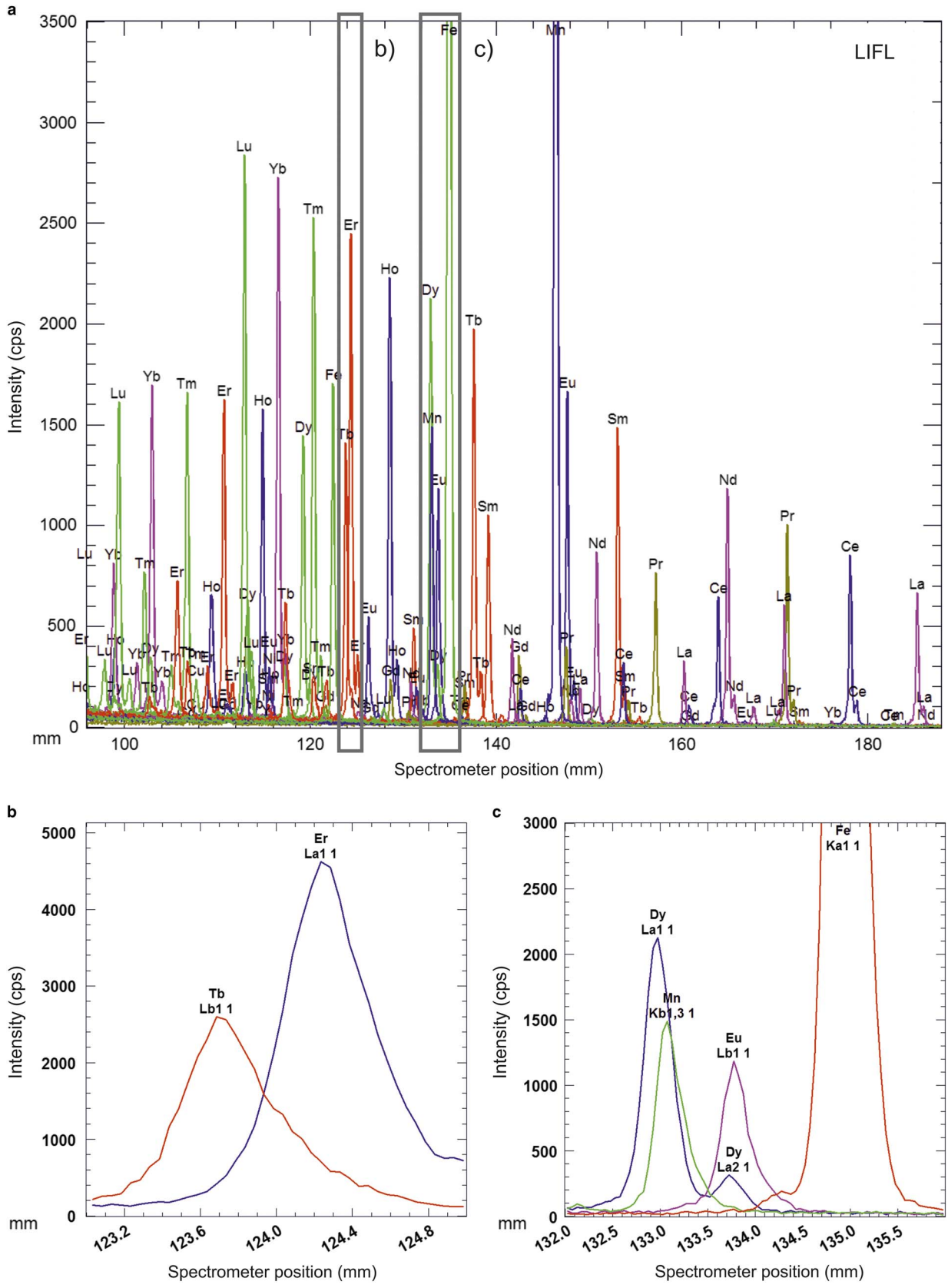

Figure 9. **a**: Spectral interferences of X-ray lines. Highlighted are (**b**) mutual interferences of rare earth elements (REE) and (**c**) overlap of REE with major elements.

Table 6. Correction Factors for the Offline Overlap Correction of Mutual Interferences.

Line	Interference	15 May 2014	29 May 2014	14 August 2014	12 September 2014	Average	Rel. SD (%)
Na Ka1,2	Ho MZ	0.0095	0.0102	0.0093	0.0076	0.0092	11.9
F Ka1,2	Ho Mb 2nd Order	0.0080	0.0059	0.0061	0.0079	0.0070	16.1
Hf Ma	K Ka2 2nd Order	0.0199	0.0196	0.0202	0.0036	0.0158	51.7
	Er Mg	0.0131	0.0133	0.0128	0.0106	0.0125	10.0
	Lu Mb	0.0616	0.0619	0.0590	0.0370	0.0549	21.8
Al Ka1,2	Tm Ma	0.0169	0.0172	0.0173	0.0102	0.0154	22.7
Si Ka1,2	—						
Zr La1,2	Y Lb1,3	0.0150	0.0139	0.0142	0.0111	0.0135	12.7
Nb La1,2	Zr Lb6	0.0090	0.0088	0.0085	0.0077	0.0085	6.7
	Hf Lg3	0.0071	0.0075	0.0073	0.0075	0.0074	2.7
Y La1,2	Hf Mg	0.0031	0.0031	0.0030	0.0033	0.0031	3.6
	Nb LL	0.0048	0.0046	0.0047	0.0042	0.0046	5.9
	Nd Lb1,4 3rd Order	0.0043	0.0045	0.0041	0.0037	0.0041	7.7
Ho Lb1	Lu La2	0.0046	0.0048	0.0041	0.0038	0.0043	10.6
Yb La1	Sm Lg3	0.0029	0.0036	0.0037	0.0020	0.0030	25.8
Dy Lb1	—						
Sm Lb1	Fe Ka2	0.0015	0.0012	0.0012	0.0011	0.0013	15.7
	Tb Lb2	0.0093	0.0100	0.0082	0.0088	0.0091	8.3
Gd La1	Ce Lg1	0.0637	0.0712	0.0709	0.0618	0.0669	7.2
	La Lg3	0.0138	0.0146	0.0149	0.0141	0.0144	3.3
	Nd Lb2,15	0.0069	0.0071	0.0077	0.0056	0.0068	13.0
Eu La1	Mn Ka2	0.0055	0.0061	0.0046	0.0048	0.0053	12.8
	Nd Lb3	0.0068	0.0081	0.0076	0.0072	0.0074	7.7
	Pr Lb2,15	0.1661	0.1602	0.1602	0.1407	0.1568	7.1
Nd Lb1	—						
K Ka1	—						
Ca Ka1	—						
Ti Ka1	La LN	0.0027	0.0030	0.0030	0.0028	0.0029	5.0
	Hf Lb1	0.0024	0.0023	0.0025	0.0023	0.0024	3.9
Lu Lb1	Yb Lb2,15	0.1107	0.1186	0.1139	0.1146	0.1145	2.8
	Dy Lg3	0.0474	0.0468	0.0470	0.0490	0.0475	2.1
	Ho Lg1	0.0879	0.0912	0.0919	0.0894	0.0901	2.0
Tb La1	Fe Ka2	0.0021	0.0020	0.0023	0.0022	0.0022	5.6
	Sm Lb3	0.0022	0.0022	0.0028	0.0025	0.0024	10.4
Cl Ka1	Nd La1	0.0035	0.0036	0.0036	0.0037	0.0036	2.2
S Ka1	Nb Lb4	0.0011	0.0013	0.0014	0.0014	0.0013	9.8
P Ka1	—						
Tm La1	Dy Lb4	0.0326	0.0321	0.0326	0.0318	0.0323	1.2
	Gd Lb2,15	0.0061	0.0057	0.0074	0.0077	0.0067	14.1
	Sm Lg1	0.0943	0.0934	0.0943	0.0945	0.0941	0.5
	Tb Lb3	0.0064	0.0059	0.0065	0.0064	0.0063	4.2
Er La1	Fe Kb1,3	0.0050	0.0054	0.0054	0.0054	0.0053	3.8
	Hf LL	0.0229	0.0228	0.0213	0.0220	0.0223	3.3
	Tb Lb4	0.1478	0.1458	0.1368	0.1364	0.1417	4.2
Fe Ka1	—						
Mn Ka1	Eu La1	0.0030	0.0036	0.0037	0.0034	0.0034	8.6
	Nd Lb3	0.0040	0.0037	0.0038	0.0038	0.0038	3.0
	Pr Lb2,15	0.0032	0.0031	0.0032	0.0032	0.0032	1.7
Pr Lb1	—						
Ce La1	—						
La La1	Nd LL	0.0038	0.0043	0.0044	0.0039	0.0041	7.0

Rel. SD, relative standard deviation.

measurement mode (steady versus scanning mode). To our knowledge, scanning mode has never been tested and applied to measure EGM, even if it is a well-known method for analysis of beam sensitive materials like feldspars and glasses with EPMA (Nielsen & Sigurdsson, 1981; Morgan & London, 1996; Couch et al., 2003 and references therein).

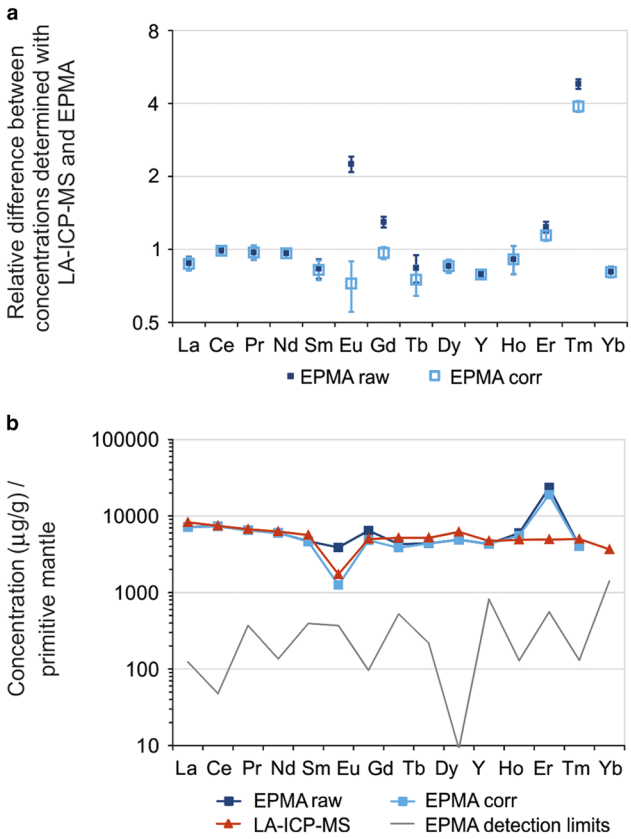

Figure 10. Comparison of rare earth elements (REE) and Y concentrations in eudialyte (21 measurements from sample NKA 5408) obtained by electron probe microanalyzer (EPMA; raw versus corr, offline overlap-corrected data) and laser ablation–inductively coupled plasma–mass spectrometry (LA-ICP-MS). **a**: The logarithmic plot on the basis of two illustrates the relative average difference within a confidence interval between elemental concentrations determined by EPMA, subsequently corrected EPMA data and LA-ICP-MS calculated concentrations. **b**: Average concentrations are normalized to primitive mantle (values given by Palme & O'Neill, 2003). Results are listed in Table 7.

The presented results clearly demonstrate the advantages of the application of scanning mode compared with measurement with a steady, defocused beam. These include less apparent specimen damage (as shown in Fig. 3), less pronounced variations in X-ray intensity (Fig. 2), and changes in intensity arising later in the period of measurement. The effects of beam diameter and scan speed settings on the analytical results are negligible for all experiments in scanning mode. The data indicate that a larger beam size and a faster scan speed improve the stability of the sample and hence yield more reliable results (Figs. 5a–5c). The effect of the size of scanned area on the analytical result becomes less apparent for scanned squares with edge lengths $\geq 17\,\mu$m indicating less alteration of the sample due to interaction with the electron beam.

The observation that in scanning mode surface damage is visibly reduced (Fig. 3b) and more stable signals over time are produced (Fig. 2) cannot alone be explained by the size of area, which is 27% larger in the case of a square with a given edge length if compared with a round beam with the same beam diameter. It can be assumed that the discontinuous exposure of the sample to the beam when applying the scanning mode if compared with the continuous exposure with the round beam accounts for most of the observed differences between both modes. Atomic force microscopy scans over the analyzed areas support this assumption showing significant increase in surface bulge with decreasing diameter and size of area (Krause et al., 2016 in preparation).

Furthermore, the nonsynchronous decline in Na signal and the remarkable late increase in X-ray intensities of other elements, seem to be very likely caused by heating EGM (to 200–400°C) and decreasing the birefringence indicating a change in the lattice parameters (Bøggild, 1953; Ahmed & MacKenzie, 1978). This could cause, or at least intensify, the loss of volatiles and water as illustrated in Figure 7. Current measurements with Raman spectroscopy performed by Krause et al. (2016, in preparation) give indications for a significant lattice change (very likely glass formation) in EGM structure, least pronounced when applying scanning mode.

The order in which elements are analyzed in a measurement sequence proves to be of great importance for the analytical precision (see Fig. 6A and Fig. 6B). It enables minimization of signal variations and ensures correct detection of elements most sensitive to beam exposure, in particular Na, K, Si, F, and Cl. However, it is important to be noted that some elements (especially those measured late in the sequence) remain affected by interaction of the electron beam with the sample. It can be assumed that the effect on the measured concentrations due to alteration of the sample by the electron beam using carefully optimized beam parameters is within the margin of the analytical uncertainty for elements with low concentrations.

Considering all above discussed implications, the optimal conditions for measurement having the smallest possible impact on the analytical result are defined for scanning mode with 6 μm beam diameter and edge lengths of a scan area of at least 17 μm. A beam current of 20 nA at an accelerating voltage of 20 kV should be retained to generate enough X-ray intensity to detect minor and trace elements. The resulting optimized measurement sequence A is listed in Table 4. However, the precise identification of suitable positions for measurement is essential and the method discussed may not be applicable for very finely zoned eudialytes (e.g., due to growth zonation). A desired higher spatial resolution needs to be critically evaluated against the above discussed negative effects in the quality of the analysis when smaller beam sizes are used.

Reference Materials

The importance of a careful selection of appropriate reference materials is a fundamental issue for accurate quantification of EPMA analyses and has been documented for the

Table 7. Comparison of Data Acquired with EPMA (Raw and Corr, Offline Overlap Corrected) and LA-ICP-MS.

	Relative Difference in Concentrations				Concentrations Normalized to Primitive Mantle (μg/g)					
	EPMA Raw/LA-ICP-MS		EPMA Corr/LA-ICP-MS		EPMA Raw		EPMA Corr		LA-ICP-MS	
Element	Average	CI (±)	Average	CI (±)	Average	Rel. SD (%)	Average	Rel. SD (%)	Average	Rel. SD (%)
La	0.88	0.06	0.87	0.06	4,926	13.27	4,895	13.35	5,667	13.89
Ce	0.99	0.04	0.99	0.04	13,055	5.26	13,055	5.26	13,288	7.75
Pr	0.97	0.07	0.97	0.07	1,752	13.58	1,752	13.58	1,813	7.09
Nd	0.96	0.04	0.96	0.04	7,970	8.40	7,970	8.40	8,301	6.96
Sm	0.83	0.08	0.82	0.08	2,008	18.17	1,983	18.40	2,425	6.72
Eu	2.25	0.17	0.72	0.17	627	17.45	203	55.42	279	8.24
Gd	1.30	0.07	0.97	0.06	3,672	7.09	2,736	9.33	2,849	9.12
Tb	0.84	0.11	0.75	0.11	450	27.40	403	30.79	542	9.98
Dy	0.85	0.05	0.85	0.05	3,113	11.02	3,113	11.02	3,679	10.70
Y	0.79	0.02	0.79	0.02	21,396	9.09	21,337	9.11	27,084	7.48
Ho	0.91	0.12	0.91	0.12	683	31.83	683	31.83	749	12.53
Er	1.24	0.06	1.14	0.06	2,781	10.49	2,572	11.34	2,270	13.04
Tm	4.81	0.22	3.89	0.20	1,686	6.04	1,363	7.57	353	11.29
Yb	0.81	0.04	0.81	0.04	1,859	14.28	1,855	14.31	2,304	10.79
Lu									259	10.10

EPMA, electron probe microanalyzer; LA-ICP-MS, laser ablation inductively coupled plasma mass spectrometry; Rel. SD, relative standard deviation; CI, confidence interval.

quality of analysis of, e.g. olivine, feldspars, garnet, and REE-phosphates (e.g., Pyle et al., 2002). As shown for a representative eudialyte analysis, the silicon concentration varies by more than 10 wt% when re-calculated offline with different reference materials for Si. Consequently, the analytical total varies considerably.

Because of the complex chemical composition and structure of the EGM, it is not possible to assess the total content of volatiles with EPMA and at the same time to use the analytical total as a criterion for the quality of the EPMA analyses. TG-MS can be used to generate information on both the total amount of volatiles contained in a sample, as well as their composition.

The total content of volatiles derived from TG-MS for the eudialyte studied here amounts to 3.3 wt%, predominantly H_2O, with minor amounts of CO_2, and SO_2 (Supplementary Appendix 3, Fig. 7). Assuming a total content of water and CO_2 around 3 wt%, the analytical total after the offline overlap correction should be around 97 wt%—a justified expectation that may be used to assess the validity of the electron microprobe data.

Among the tested reference materials for Si, plagioclase from ASTIMEX Ltd. yields an analytical total of 97.13 wt%. Using pollucite $(Cs,Na)_2Al_2Si_4O_{12}•(H_2O)$ from the same source, the analytical total is at 98.13 wt%, which appears somewhat to high (Supplementary Appendix 2, Fig. 8). However, a much larger dataset shows analytical totals ~97 wt%, if pollucite is used as reference material for Si (P. Atanasova, unpublished data). In addition, pollucite shares some chemical features with EGM, in particular its Na content, the substantial amount of water, the presence of heavier elements (Cs, Rb) similar to the REE, Y, Hf, and Nb in eudialyte. Besides SiO_2, quantification of other major and minor components (Na_2O, CaO, MnO, FeO) is also influenced by selection of the appropriate reference material—as documented in this study (see Supplementary Appendix 2 and Table 8).

Interferences

Numerous correction factors, calculated and measured, from different authors (Amli & Griffin, 1975; Roeder, 1985; Reed & Buckley, 1996; Pyle, 2001) have been reviewed in Pyle et al. (2002). The values exhibit a variation of the overlap factors between the different methods applied in the different studies (e.g., for PrLβ2 on EuLα1, the correction factor varies between 0.124 and 0.156 or for SmLg1 on TmLα1, the factor varies between 0.087 and 0.139 as compiled in Pyle et al., 2002). Thus, Roeder (1985) already noted that overlap factors have to be determined for every individual EPMA. In addition, the variability of overlap factors over time determined in this study (Table 5) illustrates that a re-determination of the overlap factors with each re-calibration of the peak position is imperative. Osbahr et al. (2015, this issue) document similar findings for major and minor elements in platinum group minerals. In view of the chemical variability of EGM, the analytical protocol needs to be adapted, cf. for Sr- or Ba-rich varieties (e.g. Tamazeght (Schilling et al. 2009) and Pilanesberg (Mitchell & Liferovich 2006)).

Comparison with LA-ICP-MS Data

In order to assess overall quality of the EPMA data and subsequent overlap corrections, the results can be compared with concentrations determined by LA-ICP-MS on the

Table 8. Final settings for further analyses.

Nr	Element/ Line	Spectrometer/ Crystal	Position Peak (mm)	Position Lower Background (mm)	Position Upper Background (mm)	Measurement Peak (s)	Measurement Background (s)	Reference Material
1	Na Ka1,2	1 TAP	129.563	0	8.043	10	5	Albite_AST
2	F Ka1,2	1 LDE1	85.011	6.946	12.1	40	10	Fluorite_AST
3	Hf Ma	1 TAP	81.799	0	1.307	120	60	Hafnium_AST
4	Al Ka1,2	1 TAP	90.596	7.188	7.4	80	20	Orthoclase_AST
5	Si Ka1,2	2 TAP	77.462	5.325	5.766	20	5	Pollucite_AST
6	Zr La1,2	2 TAP	66.023	0	2.8	30	15	Zirconia_AST
7	Nb La1,2	2 TAP	62.261	0	9.93	120	60	Niobium_AST
8	Y La1,2	2 TAP	70.124	0	2.18	80	40	Y_Phosphate_SI
9	Ho Lb1	3 LIFL	114.786	6.764	3.254	80	20	Ho_Phosphate_SI
10	Yb La1	3 LIFL	116.48	0	1.501	50	25	Yb_Phosphate_SI
11	Dy Lb1	3 LIFL	119.165	1.198	10.907	50	12.5	Dy_Phosphate_SI
12	Sm Lb1	3 LIFL	139.113	8.99	5.8	50	12.5	Sm_Phosphate_SI
13	Gd La1	3 LIFL	142.456	0	1.653	50	25	GdP_5O_{14}_AST
14	Eu La1	3 LIFL	147.612	3.525	1.98	120	30	Eu_Phosphate_SI
15	Nd Lb1	3 LIFL	150.795	1.2	5.2	40	10	Nd_Phosphate_SI
16	Cl Ka1	4 PETH	151.414	5.008	3.455	40	10	Tugtupite_AST
17	K Ka1	4 PETH	119.704	3.452	5.107	20	5	Orthoclase_AST
18	Ca Ka1	4 PETH	107.389	5.266	7.748	30	7.5	Diopside_AST
19	Ti Ka1	4 PETH	87.707	0	3.7	50	25	Rutile_AST
20	Lu Lb1	4 LIFH	99.069	5.74	0	120	60	Lu_Phosphate_SI
21	Tb La1	4 LIFH	137.589	7.566	6.361	120	30	Tb_Phosphate_SI
22	S Ka1	4 PETH	172.093	5.936	0	50	25	Sphalerite_AST
23	P Ka1	4 PETH	197.141	8	4.3	40	10	Ce_Phosphate_SI
24	Tm La1	5 LIFH	120.14	0	9.825	120	60	Tm_Phosphate_SI
25	Er La1	5 LIFH	124.154	0	5.655	50	25	Er-Phosphate_SI
26	Fe Ka1	5 LIFH	134.781	0	9.5	50	25	Magnetite_AST
27	Mn Ka1	5 LIFH	146.307	2.014	5.5	50	12.5	Rhodonite_AST
28	Pr Lb1	5 LIFH	157.131	0	1.847	50	25	Pr_Phosphate_SI
29	Ce La1	5 LIFH	178.168	4.9	2.4	50	12.5	Ce_Phosphate_SI
30	La La1	5 LIFH	185.421	4.4	3.6	50	12.5	La_Phosphate_SI

same spots. The average REE and Y concentration of 21 measurements along a profile in sample NKA 5408 obtained with the two analytical techniques are reported in Table 7. For most of these elements, interference-corrected concentrations determined with EPMA closely match the values obtained with the LA-ICP-MS within analytical errors (Fig. 10a). Exceptions are Eu, Tb, Y and Tm. The difference between concentrations determined with the two methods exceeds 20% (relative). The X-ray lines of all of these elements are subject to strong mutual interferences (Figs. 9a–9c; Table 8) and the concentrations are often less than one order of magnitude above the limit of detection of the EPMA (Fig. 10b). This illustrates that concentrations close to the detection limit associated with elevated errors in the counting statistics have to be treated with great care. It can be assumed that both the low net count rate and mutual interferences prevent a reliable analysis of some REE with EPMA at such concentrations.

The REE-patterns in the normalized plot (Fig. 10b) are also helpful to evaluate the quality of analysis since they commonly form straight trends in magmatic systems with the exception of Europium. The overall shape of the REE pattern derived from the EPMA measurements is straight with the exception of the elements mentioned above. This indicates that interference-corrected concentrations for most of the REE are appropriate.

For Y, the REE pattern derived from LA-ICP-MS shows a slight positive anomaly, which points to an analytical problem with the LA-ICP-MS analysis of Y. Lutetium could not be measured with EPMA due to several peak overlaps and because the background measurement is influenced by mutual interferences. Since the HREE are of particular importance, the use of an alternative analytical method such as LA-ICP-MS or secondary ion mass spectrometry should be considered, if HREE occur at trace element level.

Conclusions

On the basis of 101 experiments, the behavior of EGM during electron beam exposure is tested. Thereby the following fundamental observations are made:

1. Eudialyte is highly sensitive to beam exposure and thus conditions are required to minimize near surface crystal

lattice destruction. Scanning a square instead of performing measurements with a steady, defocused beam is found to be less destructive and detected X-Ray intensities remain more stable over time. Optimal results are obtained scanning a square of at least 17 μm edge lengths using a defocused beam of 6 μm and the fastest scan speed settings. The effect of irradiation on the analytical result is further reduced by measuring elements most sensitive to beam exposure (e.g., Na, Cl, F, Si, and Ca) very early in the sequence.

2. The choice of appropriate reference materials is proved to be of great importance for accurate quantification. Materials having analogous chemical properties and content of volatiles are found to be most favorable.
3. Adequate positioning of upper and lower background or measurement of only one background, as well as careful selection of a line free of interferences (e.g., HoL_{β} instead of HoL_{α}), are highly advisable. Additional re-determination of offline overlap correction factors with each individual calibration is essential for obtaining appropriate analytical results.
4. A combination with other analytical techniques (e.g., XRF/XRD to determine incorporated elements; TG-MS to identify the nature and amount of volatiles; LA-ICP-MS or SIMS to verify quality of data and to complement elements with concentrations close to detection limit) is essential for successful optimization of the EPMA analytical protocol.

Following these considerations is mandatory for a successful quantitative determination of the chemical composition of EGM with EPMA.

The wide compositional variety and the often complex chemical zonation of EGM requires customization of the analytical protocol in particular with respect to additional elements such as Sr or Ba and to the size of the scanned area according to the zonation patterns in the sample. In cases of very fine compositional zonation, the desired spatial resolution has to be pondered against the negative effects of electron beam interaction with the sample on the analytical precision.

Acknowledgments

Research for this study was mainly performed at the Helmholtz Institute Freiberg for Resource Technology. It was supported and benefited from numerous discussions with Sabine Haser, Bernhard Schulz, Max Frenzel and Axel Renno. Their help is sincerely acknowledged. LA-ICP-MS analyses were carried out at the Institute for Mineralogy of the Westfälische Wilhelms-Universität Münster with the greatly appreciated assistance of Jasper Berndt and Beate Schmitte. TG-MS measurements were performed at the Institute for Mineralogy, Technical University Bergakademie Freiberg by Dominique Briesing in the laboratory of Gerhard Heide. The authors are deeply grateful for their support. Sincere thanks are given to Andreas Bartzsch und Maik Trogisch for producing polished thin and thick sections required for this study. Furthermore, the authors are indebted to Tasman Metals Ltd. for supporting field work and for providing rock samples. The manuscript was improved by the comments and suggestions of two anonymous reviewers. Their help is greatly appreciated. The authors thank MAM for the great editorial handling.

References

Ahmed, M. & MacKenzie, W.S. (1978). Preliminary report on the synthesis and stability of eudialyte. In *Progress in Experimental Petrology. Fourth Progress Report 1975–1978*, MacKenzie, W.S. (Ed.), **11**, pp. 47–49. Series D, Manchester, NERC.

Amli, R. & Griffin, W.L. (1975). Microprobe analysis of REE minerals using empirical correction factors. *Am Mineral* **60**, 599–606.

Andersen, T., Erambert, M., Larsen, A.O. & Selbekk, R.S. (2010). Petrology of nepheline syenite pegmatites in the Oslo rift, Norway: Zirconium silicate mineral assemblages as indicators of alkalinity and volatile fugacity in mildly agpaitic magma. *J Petrol* **51**(11), 2303–2325.

Atanasova, P., Krause, J. & Gutzmer, J. (2013). Mineralogical characterization of REE mineralization in Norra Kärr alkaline complex, Sweden, 12th SGA Biannual Meeting, 12–15 August 2013, Uppsala, Sweden, pp. 298–301.

Bøggild, O.B. (1953). The mineralogy of Greenland. *Meddelelser dm Grønland* **149**(3), 1–442.

Chakrabarty, A., Pruseth, K.L. & Sen, A.K. (2012). Compositions and petrogenetic significance of the eudialyte group minerals from Sushina, Purulia, West Bengal. *J Geol Soc India* **79**, 449–459.

Couch, S., Harford, C.L., Sparks, R.S.J. & Carroll, M.R. (2003). Experimental constraints on the conditions of formation of highly calcic plagioclase microlites at the Soufriéte Hills Volcano, Montserrat. *J Petrol* **44**(8), 1455–1475.

Coulson, I.M. & Chambers, A.D. (1996). Patterns of zonation in rare-earth-bearing minerals in nepheline syenites of the North Qôroq Center, South Greenland. *Canad Mineral* **34**, 1163–1178.

Jarosewich, E. & Boatner, L. (1991). Rare-earth element reference samples for electron microprobe analysis. *Geostandards Newsletter* **15**(2), 307–309.

Jochum, K.P., Stoll, B., Herwig, K. & Willbold, M. (2006). Improvement of in situ Pb isotope analysis by LA-ICP-MS using a 193 nm Nd:YAG laser. *J Anal At Spectrom* **21**, 666–675.

Jochum, K.P., Stoll, B., Herwig, K. & Willbold, M. (2007). Validation of LA-ICP-MS trace element analysis of geological glasses using a new solid-state 193 nm Nd:YAG laser and matrix matched calibration. *J Anal At Spectrom* **22**, 112–121.

Johnsen, O. & Gault, R.A. (1997). Chemical variation in eudialyte. *Neues Jahrbuch der Mineralogie Abhandlungen* **171**, 215–237.

Johnsen, O., Ferraris, G., Gault, R.A., Grice, J., Kampf, A.R. & Pekov, I.V. (2003). The nomenclature of eudialyte-group minerals. *Canad Mineral* **41**, 785–794.

Krause, J., Rudolph, M., Atanasova, P. & Gutzmer, J. (2016). Effects of electron beam irradiation on eudialyte group minerals. Manuscript in preparation.

Mitchell, R.H. & Liferovich, R.P. (2006). Subsolidus deuteric/hydrothermal alteration of eudialyte in lujavrite from the Pilansberg alkaline complex, South Africa. *Lithos* **91**, 352–372.

Morgan, G.B. VI & London, D. (1996). Optimizing the electron microprobe analysis of hydrous alkali aluminosilicate glasses. *Am Mineral* **81**, 1176–1185.

Nielsen, C.H. & Sigurdsson, H. (1981). Quantitative methods for electron microprobe analysis of sodium in natural and synthetic glasses. *Am Mineral* **66**, 547–552.

Olivo, G.R. & Williams-Jones, A.E. (1999). Hydrothermal REE-rich eudialyte from the Pilanesberg complex, South Africa. *Canad Mineral* **37**, 653–663.

Osbahr, I., Krause, J., Bachmann, K. & Gutzmer, J. (2015). Efficient and accurate identification of platinum group minerals by a combination of mineral liberation analysis and electron probe microanalyser with a new approach of offline overlap correction of platinum group elements concentrations. *Microsc Microanal.* (this issue).

Palme, H. & O'Neill, H.S.C. (2003). Cosmochemical estimates of mantle composition. In *The Mantle and Core*, Carlson, R.W. (Eds.), vol. 2: *Treatise on Geochemistry*, Holland, H.D. & Turekian, K.K., pp. 1–38. Oxford: Elsevier-Pergamon.

Pfaff, K., Krumrei, T., Marks, M., Wenzel, T., Rudolf, T. & Markl, G. (2008). Chemical and physical evolution of the 'lower layered sequence' from the nepheline syenitic Ilímaussaq intrusion, South Greenland: Implications for the origin of magmatic layering in peralkaline felsic liquids. *Lithos* **106**, 280–296.

Pfaff, K., Wenzel, T., Schilling, J., Marks, M.A.W. & Markl, G. (2010). A fast and easy-to-use approach to cation site assignment for eudialyte-group minerals. *Neues Jahrbuch der Mineralogie Abhandlungen* **171**, 215–237.

Pyle, J.M. (2001). Distribution of selected trace elements in pelitic metamorphic rocks: pressure, temperature, mineral assemblage and reaction-history controls. PhD dissertation, Rensselaer Polytechnic Institute, Troy, NY.

Pyle, J.M., Spear, F.S. & Wark, D.A. (2002). Electron microprobe analysis of REE in apatite, monazite and xenotime: Protocols and pitfalls. In *Reviews in Mineralogy and Geochemistry*, Kohn, M.L., Rakovan, J. & Hughes, J.M. (Eds.), vol. 48: *Phosphates*, pp. 337–362. Washington, DC, Mineralogical Society of America.

Rastsvetaeva, R.A. (2007). Structural mineralogy of the eudialyte group: A review. *Crystallogr Rep* **52**(1), 47–64.

Reed, S.J.B. & Buckley, A. (1996). Virtual WDS. *Microchimica Acta* **13**, 479–483.

Roeder, P.L. (1985). Electron-microprobe analysis of minerals for rare-earth elements: Use of calculated peak-overlap correction. *Canad Mineral* **23**, 263–271.

Schilling, J., Marks, M.A.W., Wenzel, T. & Markl, G. (2009). Reconstruction of magmatic to subsolidus processes in an agpaitic system using eudialyte textures and composition: A case study from Tamazeght, Morocco. *Canad Mineral* **47**, 351–365.

Schilling, J., Wu, F.Y., McCammon, C., Wenzel, T., Marks, M.A.W., Pfaff, K., Jacob, D.E. & Markl, G. (2011). The compositional variability of eudialyte-group minerals. *Mineral Mag* **75**(1), 87–115.

Sjöqvist, A.S.L., Cornell, D.H., Andersen, T., Erambert, M., Ek, M. & Leijd, M. (2013). Three compositional varieties of rare-earth element ore: Eudialyte-group minerals from the Norra Kärr alkaline complex, Southern Sweden. *Minerals* **3**, 94–120.

Stormer, J.C. Jr., Pierson, M.L. & Tacker, R.C. (1993). Variations of F and Cl X-ray intensity due to anisotropic diffusion in apatite during electron microprobe analysis. *Am Mineral* **78**, 641–648.

.

Appendix B

This is a pre-copyedited, author-produced version of an article accepted for publication in Journal of Petrology following peer review. The version of record Atanasova, P., Marks, M.A.W., Heinig, T., Krause, J., Gutzmer, J., Markl, G., 2017. Distinguishing Magmatic and Metamorphic Processes in Peralkaline Rocks of the Norra Kärr Complex (Southern Sweden) Using Textural and Compositional Variations of Clinopyroxene and Eudialyte-group Minerals. J. Petrol. 58, 361–384. is available online at: https://doi.org/10.1093/petrology/egx019 and DOI: 10.1093/petrology/egx019.

Distinguishing magmatic and metamorphic processes in peralkaline rocks of the Norra Kärr complex (Southern Sweden) using textural and compositional variations of clinopyroxene and eudialyte-group minerals.

Atanasova P.[1,2], Marks M. A. W.[2], Heinig T.[1], Krause J.[1], Gutzmer J.[1,3], Markl G.[2]

[1]Helmholtz-Zentrum Dresden - Rossendorf, Helmholtz Institute Freiberg for Resource Technology, 09599 Freiberg, Saxony, Germany

[2]Universität Tübingen, Fachbereich Geowissenschaften, 72074 Tübingen, Germany

[3]Technical University Bergakademie Freiberg, Department of Mineralogy, 09596 Freiberg, Germany

Keywords: deformed nepheline syenite; rare earth elements; clinopyroxene, eudialyte-group minerals

Abstract

The 1.49 Ga old Norra Kärr complex in Southern Sweden contains rocks characterized by a very high ratio of (Na+K)/Al ≥ 1.2 and a complex and highly unusual mineralogy, including rock-forming catapleiite, eudialyte-group minerals as well as minor rinkite- and britholite-group minerals. In contrast to other well-studied examples of agpaitic rocks, the Norra Kärr rocks have been deformed and partially metamorphosed during the Sveconorvegian/Grenvillian orogeny, and are now preserved in a westward dipping synform.

Magmatic and metamorphic processes at the Norra Kärr complex are distinguished by combining rock fabrics of clinopyroxene and eudialyte-group minerals. Both mineral groups are stable over a large P-T range, which makes them excellent monitors of the geochemical evolution of such systems and enables the reconstruction of magmatic and subsequent metamorphic conditions.

The magmatic mineral assemblage crystallized from a subsolvus syenite at continuously decreasing temperatures (700 - 450ºC) and silica activity (0.6 - 0.3). Due to initially relatively low peralkalinity and reducing conditions, Zr was first incorporated in Zr-aegirine. Subsequent destabilization of the latter indicates increasing peralkalinity, oxygen fugacity and water activity, which resulted in the crystallization of early magmatic catapleiite. Crystallization of presumably later magmatic Mn- and REE-poor eudialyte-group minerals happened as soon as sufficient Cl, REE and HFSE were enriched in the residual melt.

Metamorphic conditions during the Sveconorvegian/Grenvillian orogeny are constrained to T between 400 - 550ºC and a_{SiO2} range of 0.25 - 0.4. Due to deformation and interaction with fluids, post-magmatic Al-rich aegirine as well as post-magmatic eudialyte-group minerals enriched in REE, Y and Mn formed. Subsequently, the eudialyte-group minerals were destabilized and decomposed to post-magmatic catapleiite and secondary REE-bearing minerals. During the whole history of the complex, a_{SiO2} remains very similar, indicating very little interaction with the surrounding granitic rocks.

Regardless of the intense deformation due to folding of the Norra Kärr body during the Sveconorvegian /Grenvillian orogeny, indications for primary magmatic layering of the intrusion are retained on the deposit scale. In addition, the compositional changes of magmatic eudialyte-group minerals from the outer to the inner subunit indicate a primary geochemical evolution feature due to fractional crystallization.

INTRODUCTION

During the last decade the economic interest in high field strength elements (HFSE) and rare earth elements (REE) increased due to their broad application in high-tech products. In addition to carbonatites, alkaline and especially peralkaline rocks (molar Na+K > Al) are particularly enriched in HFSE and comprise one of the most promising sources for future REE supply (Goodenough et al., 2016; Mitchell, 2015; Smith et al., 2016). The extraordinary enrichment of HFSE and REE in such rocks was explained by the high alkalinity and the reducing conditions during crystallization of the magma, which minimizes the loss of volatile components and maximizes the ore precipitation potential during magmatic differentiation (e.g. Kogarko, 1990; Marks et al., 2011).

This study investigates peralkaline rocks of the Norra Kärr complex in southern Sweden, which are characterized by an unusual mineralogy including rock-forming catapleiite, eudialyte-group minerals (EGM) and minor REE-bearing minerals of the rinkite- and britholite-groups (Adamson, 1944; Sjöqvist et al., 2013; von Eckermann, 1968). Such lithologies are classified as agpaitic rocks, a term originally introduced by Ussing (1912) and later complemented by Sørensen (1997, 1960) and (Marks et al., 2011). Minerals of the eudialyte group are the most common index minerals in agpaitic rocks (J Schilling et al., 2011; Sørensen, 1997). Such minerals can incorporate significant concentrations of more than 30 elements, including Zr, Nb and naturally occurring lanthanides and Y, with LREE being commonly more abundant than the HREE.

Unlike other well-studied examples of agpaitic complexes such as the Ilímaussaq complex in Greenland (most recent work by Dostal, 2015; Marks and Markl, 2015; Sørensen et al., 2006; Upton, 2013) or the Lovozero and Khibina complexes in Russia (Arzamastsev et al., 2005, 2001; Kogarko, 1987; Kogarko et al., 1982; Pekov, 1998), the igneous Norra Kärr body has been deformed and partially recrystallized during subsequent metamorphic events. This specific feature is used to amplify the restricted knowledge on the behavior of agpaitic rocks during metamorphism, which is to date mainly limited to studies of the Red Wine and Kipawa complexes in Canada (Breemen and Currie, 2004; Currie and Breemen, 1996; Curtis and Currie, 1981; Curtis and Gittins, 1979); nepheline syenites in Malawi (Woolley et al., 1996) and peralkaline gneisses in India (Chakrabarty et al., 2016a; Goswami and Basu, 2013; Nanda et al., 2008). We present detailed observations on rock and mineral textures combined with compositional data

for the major rock-forming minerals to provide some direct insight into the petrological and geochemical processes accompanied by the deformation and metamorphism of agpaitic rocks.

GEOLOGICAL SETTING

The Norra Kärr complex is located approx. 2 km E of Lake Vättern, approx. 15 km NNE of the township of Gränna in Southern Sweden (Fig. 1). It is situated in the Trans-scandinavian Igneous Belt, which intruded into the Svecofennian domain of Fennoscandia in the course of juvenile crust reworking between 1.85–1.75 Ga (Andersson et al., 2007 and references therein). The Trans-scandinavian Igneous Belt rocks form a voluminous array of monzodioritic to granitic batholiths of alkali-calcic to calc-alkaline composition (Högdahl et al., 2004) (Fig. 1). They extend over ca. 1400 km from NW Norway to SE Sweden. Significant igneous activity between 1.65–1.50 Ga was responsible for the formation of an active margin along the south-western border of the Fennoscandian Shield (McLelland, 1989). From ca. 1470 Ma onwards A- and I-type granitoids and syenitoids were emplaced in a typical volcanic-arc setting, marking the pre-collisional stage of the Danopolonian or Hallandian orogeny in the area east and southeast of Lake Vättern (Brander, 2011; Brander and Söderlund, 2009). In the time of 1.5-1.4 Ga two possible settings for intra-cratonic magmatism are discussed in the literature, an anorogenic and an orogenic extension.

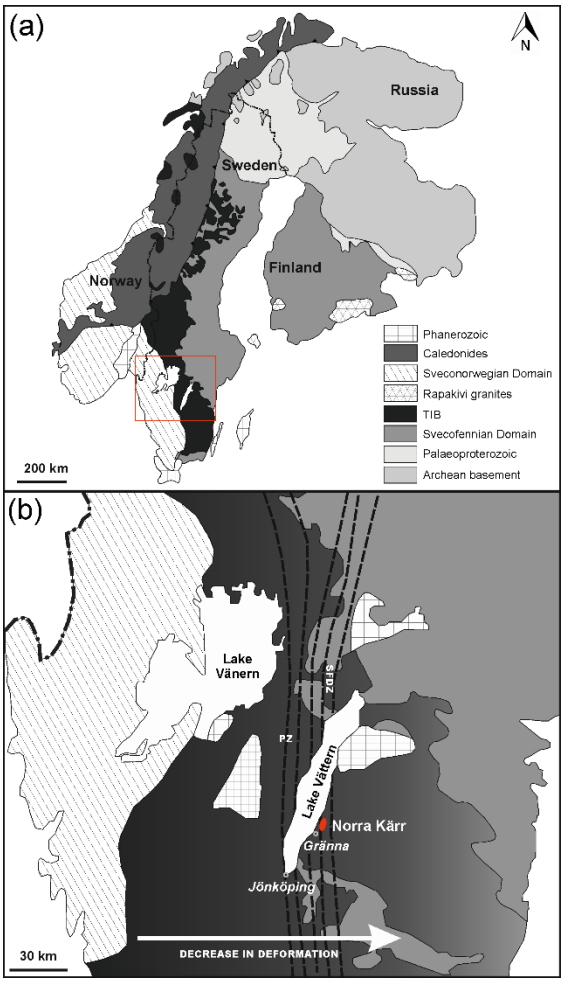

Fig.1. (a) Simplified geological map of Fennoscandia illustrating major lithological units (modified after Högdahl et al., 2004). Red box is enlarged in (b), where the red ellipse resembles the Norra Kärr complex. The white arrow indicates the direction of decreasing regional deformation during the Sveconorwegian orogeny. PZ - Protogine Zone, SFDZ - Sveconorwegian Frontal Deformation Zone (simplified after Söderlund et al., 2002; Wahlgren et al., 1994).

Åberg (1988) interpreted the emplacement of alkali-calcic and calc-alkaline intrusions into the southernmost parts of the Trans-scandinavian Igneous Belt as a product of continental rifting between 1.48 and 1.35 Ga (Åberg et al., 1985a, 1985b, 1984; Smellie and Stuckless, 1985).

During the period of around 1140 – 900 Ma wide areas of the southern and central Trans-scandinavian Igneous Belt, as well as broad areas of south-western Fennoscandia were subject to the collision of Fennoscandia with Amazonia during the Grenvillian/Sveconorwegian orogeny (Bingen et al., 2008). These areas form today the Sveconorwegian orogenic belt. The area east of Lake Vättern belongs to the frontal zone of the orogen and was mainly affected by metamorphism during the late stages of the orogeny, the so-called Falkenberg and Dalane phases (Bingen et al., 2008 and references therein). During the Falkenberg phase (980-970 Ma) crustal thickening and associated eclogite facies conditions affected the Fennoscandian crust to at least 50 km depth. This was followed by decompression, relaxation and gravitational collapse during the Dalane phase at 970-900 Ma (Bingen et al., 2008, 2006; Möller et al., 2007). During this time the N-S trending Protogine Zone was formed as a steep, sheer zone at the very front of the Sveconorvegian orogen (Andréasson and Rodhe, 1994; Söderlund et al., 2004; Wahlgren et al., 1994).

The Norra Kärr complex

The relatively small Norra Kärr complex covers an area of approx. 350 x 1100 m and is located in the Växjö Granite Suite (TIB I), between the Vimmerby Batholith in the east and the major Protogine shear zone (PZ) in the west (Fig. 1b). The body is preserved within a westwards dipping (approx. 40°) synform (Fig. 2), deformed by moderate E-W and late, weak N-S directed compression under ductile conditions (Rankin, 2011).

The granitic host rocks at the western contact of the Norra Kärr complex and some deeper parts in the east (only known from drilling cores) exhibit clear signs of fenitization (Adamson, 1944; Sjöqvist, 2015; von Eckermann, 1968). These fenites are up to 100 m wide massive horizons, but also occur as decimeter-thick veins in the surrounding granite. They are characterized by the absence of quartz, which is replaced by albite, magnetite, hematite and fluorite, and the replacement of biotite by aegirine (Adamson, 1944; Sjöqvist, 2015). Fenitization of the alkaline rocks itself is less prominent and rarely occurs in the outer subunit, only at the direct contact to the fenitized host rocks.

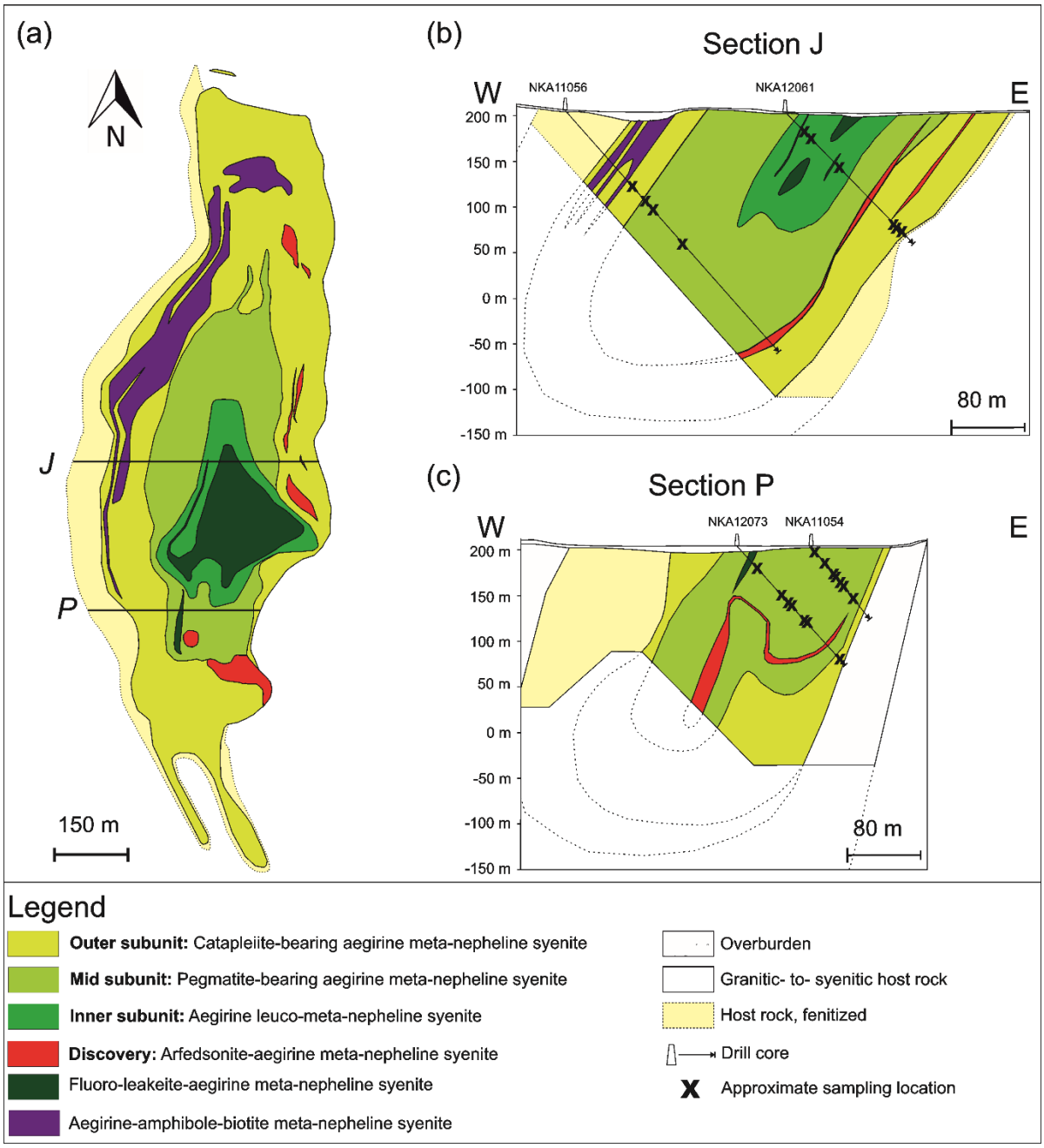

Fig.2. (a) Simplified geological map of the Norra Kärr complex illustrating major lithological units (modified after Tasman Metals Ltd.). The deformation is well visualized in W-E cross sections (b) J and (c) P. The sampling locations as given in Table 1 are marked as black crosses.

Recently, the fenitization of the granitic gneisses was determined to have a U-Pb zircon age of 1.49 ± 0.01 Ga (Sjöqvist et al., 2014), which is interpreted coeval with the age of magmatic emplacement of the Norra Kärr complex in a presumably pre-collisional rifting setting. Younger ages determined by Sjöqvist et al. (2014) constrain the deformation during the Sveconorvegian orogeny from 1148 ± 5 Ma onwards. At Norra Kärr neither the surrounding country rocks (granitic- to-

syenitic gneisses) nor the metamorphosed syenites of the complex itself provide any clear evidence indicating the grade of metamorphism of the complex. Regional geological studies report lower greenschist facies conditions for the area to the East of Lake Vättern and the Protogine shear Zone (Fig. 1). Considering this and the actual position of the complex within this major shear zone (Fig. 1), moderate to high greenschist facies conditions can be assumed.

For this study, the peralkaline rocks of the Norra Kärr complex were collectively classified as meta-nepheline syenites (Gillespie and Styles, 1999). The most common rock type (85 vol.% of the exposed area), the so-called grennaite (Adamson, 1944) is a catapleiite-and EGM-bearing aegirine meta-nepheline syenite (Fig. 2). The texture of this unit varies systematically across the deposit (Figs 3, 4). On the basis of the frequency of medium- to- coarse-grained lenses and bands or schlieren (Adamson, 1944; Sjöqvist, 2015; Törnebohm, 1906) the frequency of catapleiite and the degree of deformation, the following three subunits with gradual transitions between them are distinguished. 1) The central part (inner subunit) was strongly foliated (Figs 3a-b and 4a-c) and is best described as an aegirine leuco-meta-nepheline syenite (a.k.a. migmatitic grennaite; lithologic nomenclature by Tasman Metals Ltd.). This area is surrounded by a zone rich in pegmatoidal schlieren (mid subunit, Figs 3e-h and 4e and i-k) named pegmatite-bearing aegirine meta-nepheline syenite (a.k.a. pegmatitic grennaite) (Adamson, 1944). The border area (outer subunit, Figs 3c and 4f-h) of the complex is defined by a foliated catapleiite-bearing aegirine meta-nepheline syenite (a.k.a. catapleiite grennaite) (Adamson, 1944).

Minor rock types of the Norra Kärr complex include the strongly folded fluoro-leakeite-aegirine meta-nepheline syenite (previously called kaxtorpite, Fig. 4d), the aegirine-amphibole-biotite meta-nepheline syenite (a.k.a. pulaskite) and the arfvedsonite-aegirine meta-nepheline syenite (former lakarpite), well-known from the discovery outcrop of Norra Kärr (Sjöqvist et al., 2013).

The most common deformation features of all rock types include the alignment and stretching of certain minerals (e.g. clinopyroxene, EGM, catapleiite, Fig. 4a-e) and the presence of porphyroclasts (mainly microcline, Fig. 4f-h), which have tails of recrystallized material (Fig. 4h). They are commonly preserved in a finer-grained, probably recrystallized matrix and form typical shear related patterns (sigma- and delta-clast, Fig. 4f).

PETROGRAPHY

The phase assemblages and micro-textural characteristics of the investigated samples are described in the following. A list of investigated samples is given in Table 1, sample locations are indicated in Fig.2. The modal mineralogy of the main subunits is summarized in Table 2.

Catapleiite-and EGM-bearing aegirine meta-nepheline syenite (grennaite)

Inner subunit (aegirine leuco-meta-nepheline syenite)

This unit displays strong foliation and in places intense folding, with rather common crenulated foliation and gneissic textures (Figs 3a and b and 4a-c). The main felsic minerals are subhedral to anhedral and fine-grained albite (up to 30 wt.%), microcline (up to 20 wt.%) and nepheline (approx. 10 wt.%), the latter being partly to significantly replaced by natrolite (10-35 wt.%). Fine-to-medium-grained aegirine (15-20 wt.%) occurs as subhedral to anhedral, needle or columnar-shaped crystals, which commonly exhibit irregular rims and/or replacement textures of darker BSE contrast (Fig. 5c). Fine-to-medium-grained EGM (approx. 15 wt.%), can be concentrated in hinge zones of folds and be partly enriched in mm-wide bands, mainly composed of feldspar and clinopyroxene (Fig. 4c). In these bands elongated minerals are aligned while coarser-grained minerals form σ- and/or δ-clasts. Eudialyte-group minerals are commonly elongated and ductile deformed in the direction of foliation (Figs 3a, 4a and 6c). The crystals show no zoning or overgrowth textures but are commonly intergrown with fine-grained, anhedral catapleiite and minor britholite-group minerals. The most common accessories include galena and sphalerite.

Mid subunit (pegmatite-bearing aegirine meta-nepheline syenite)

This subunit contains variable amounts of leucocratic, mid-to-coarse-grained and partly-pegmatitic nepheline syenite schlieren (up to ten cm in thickness) set in a fine-grained aegirine meta-nepheline syenite matrix.

The dark green-grey matrix (grain size < 1mm) is characterized by a homogeneous mineral distribution with no specific accumulation of minerals (Fig. 3d). Deformation is displayed by the alignment of most of the mineral grains (Fig. 4e) and stretching of rarely occurring larger crystals (e.g. catapleiite needles). The main rock-forming minerals are anhedral albite (55 wt.%), nepheline (10 wt.%) and clinopyroxene (20 wt.%) with minor

microcline (5 wt.%), catapleiite (3 wt.%), EGM (2 wt.%), natrolite (3 wt.%) and accessory britholite- and rinkite-group minerals (≤ 0.25 wt.%). The latter are always spatially associated with EGM.

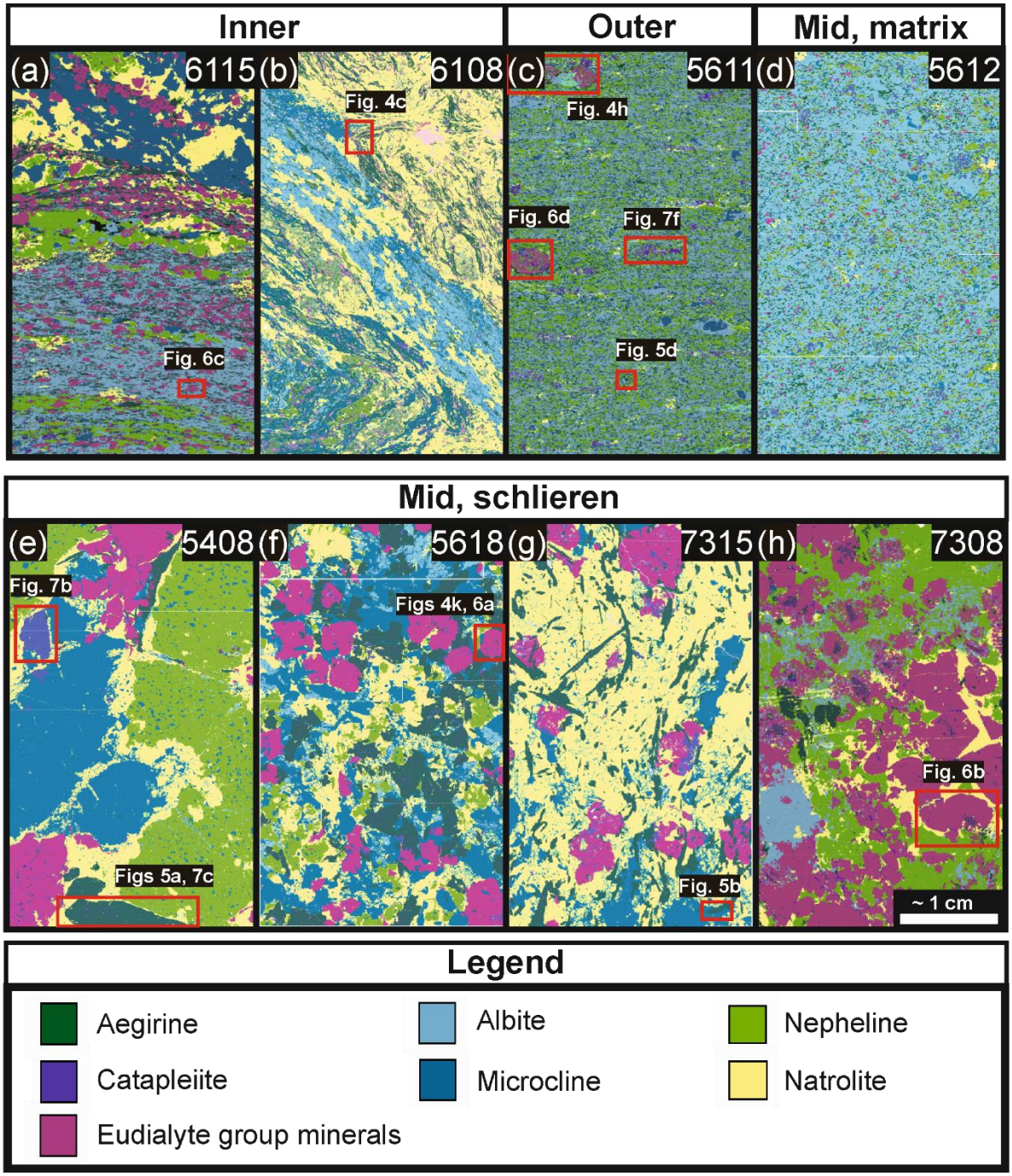

Fig.3. Mineral Liberation Analyzer (MLA) classified-color images (EDX-GXMAP mode) of the different subunits of Norra Kärr. Illustrated are characteristic textures of a) the incipient alignment and stretching of minerals and b) the macroscopic scale folding and alignment of minerals in the inner subunit; (c) poikilitic EGM in a fine grained matrix of the outer subunit; (d) homogeneous matrix of the mid subunit; (e)-(h) thoroughly preserved euhedral to subhedral EGM and clinopyroxene in leucocratic schlieren of the mid subunit. Nepheline is partly to strongly altered to natrolite. Areas marked as red boxes are enlarged in Figs 4, 5 and 6.

The schlieren (Figs 3e-h and 4i-k) generally follow the foliation and the folding of the rock. However, they also may be intercalated with the fine-grained matrix. The following types of schlieren can be distinguished:

(A) Fine-to-medium-grained schlieren with no alignment of crystals, mainly consisting of feldspar, clinopyroxene, euhedral to subhedral EGM and nepheline (e.g. Figs 3f and h, 4i, 6a and b and 7d and e). In general, the relative content of clinopyroxene increases towards the rims of these schlieren. Eudialyte-group minerals are medium-to-coarse-grained reaching several mm in size (Figs 3f and h, 4k and 6a and b). Larger crystals are commonly sector- or oscillatory-zoned. Porous and irregular zones in the central parts of euhedral crystals can be complexly overgrown by areas with lower BSE contrast and along the rims of such crystals flame textures with higher BSE contrast may be present (Figs 4k and 6a and b). Rims and cracks are commonly associated with catapleiite and britholite-group minerals, occurring as filling of interstitial spaces or replacing EGM (Fig. 6a and b). Catapleiite occurs as two textural varieties, (1) catapleiite spatially associated or intergrown with EGM, preferably occurring at the border area between clinopyroxene and EGM (Fig. 7e) and (2) catapleiite inclusions in fan-shaped sectors of radiating clinopyroxene aggregates (Figs 4i and 7d). These radial aggregates of subhedral clinopyroxenes (Fig. 7d) are unique to this schlieren type. They are irregularly rimmed by areas with darker BSE contrast.

(B) Medium-to-coarse-grained schlieren with no general alignment of crystals. They are mainly composed of subhedral to euhedral feldspar, nepheline, clinopyroxene and EGM (Figs 3e and g, 4j, 5a and b and 7c). Euhedral to subhedral eudialyte-group minerals mainly exhibit sector zoning. Similar to schlieren (A) these are overgrown and/or replaced by irregular or flamy areas with brighter BSE contrast (Fig. 4k). In cases EGM are extensively altered and replaced by catapleiite and britholite-group minerals (Fig. 3g). In contrast to schlieren (A), catapleiite is not necessarily spatially associated with EGM or clinopyroxene. It may form needles, laths (rarely with a bluish color in hand specimen) or subhedral crystals (Figs 3e and 7b). Clinopyroxene forms euhedral, coarse-grained and oscillatory- and/or sector-zoned crystals (Fig. 5a and b). An exceptionally large (> 1 cm) and euhedral clinopyroxene crystal was observed in sample 5408 (Figs 5a and 7c). This crystal exhibits a partly-resorbed Zr-rich core, surrounded by an area rich in anhedral catapleiite inclusions, followed by well-

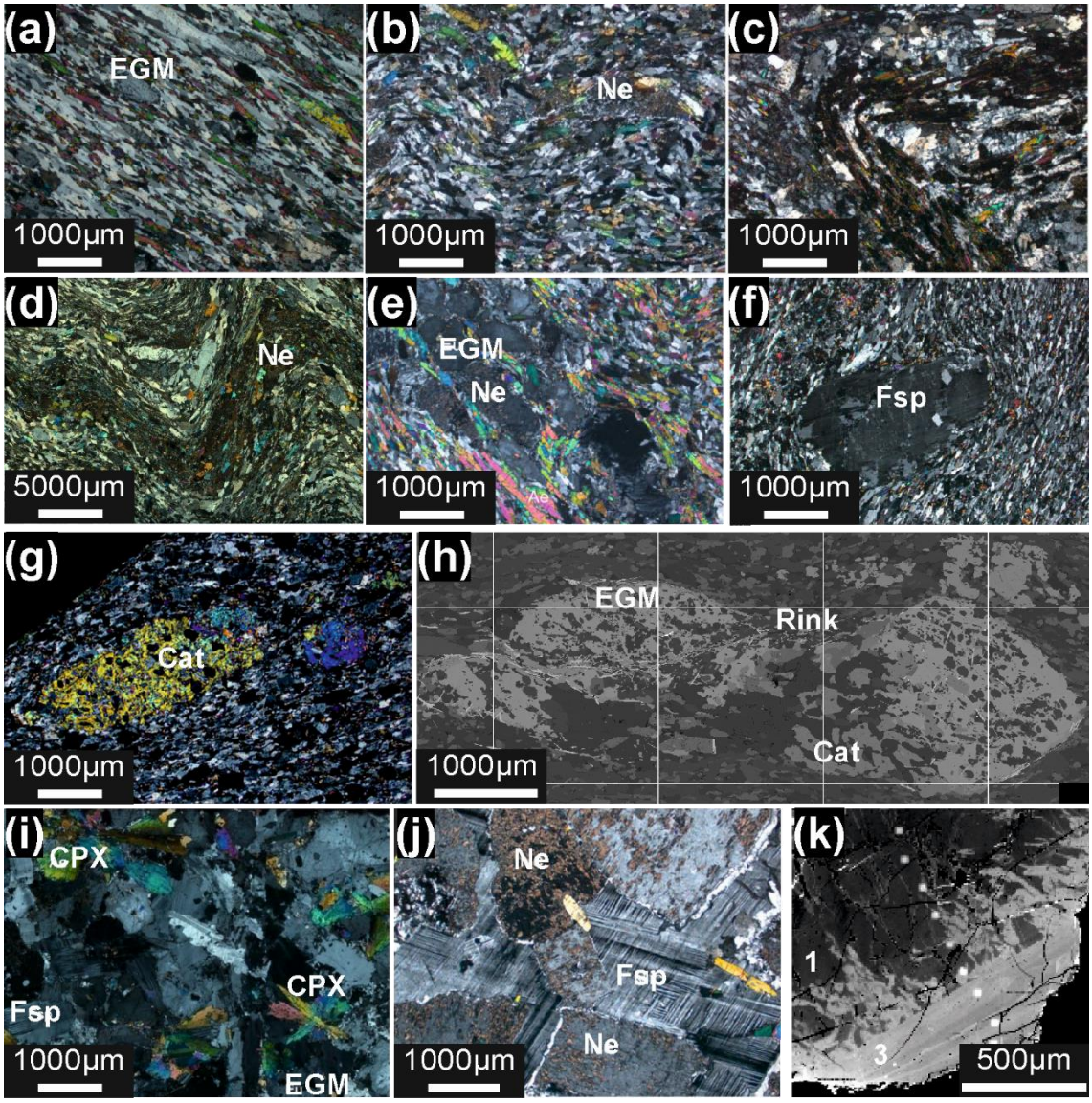

Fig.4. (a) Alignment of minerals as well as (b) and (c) microscopic to macroscopic scale folding as common features of the inner subunit; EGM crystals in (a) are slightly stretched. (d) Folding of the fluoro-leakeite-aegirine meta-nepheline syenite rock. (e) Fine-grained meta-nepheline syenite with a band of mid-to-coarse-grained nepheline and eudialyte. The nepheline crystals show alteration. (f) Microcline δ-clast, (g) catapleiite and (h) EGM (type (4)) porphyroclasts are characteristic for the outer subunit. EGM contain inclusions of catapleiite, feldspar, nepheline and clinopyroxene. Catapleiite (Cat) forms tails and replaces EGM mainly at the rim. EGM are surrounded by columnar rinkite-group minerals (Rink). (i) Medium-grained schlieren of the mid subunit with feldspar, aegirine and EGM show no particular alignment, aegirine crystals (CPX) form radiating aggregates. (i) Coarse-grained microcline and extensively altered nepheline from schlieren of the mid subunit. (k) EGM (3) overgrow and/or replace the compositionally different EGM (1) in schlieren of the mid subunit; visible white spots represent EPMA measurement locations.

developed Ti-rich sectors and late irregular rims of Al-rich aegirine. In both schlieren types, large, patchy aggregates composed of numerous euhedral fine-grained clinopyroxene crystals (Fig. 3e and h) occur. Nepheline and feldspar are extensively altered to natrolite (Figs 3e-h and 4e and j).

Outer subunit (catapleiite-bearing aegirine meta-nepheline syenite)

Both, magmatic and metamorphic terminology is used to describe the textural appearance of this subunit, although the classification of some of the features is not clear. This will be further commented in the discussion section.

This unit is up to several hundred meters in width, is schistose and fine-grained to aphanitic with porphyroclastic textures (Figs 3c and 4f-h). The contact towards the surrounding host rocks is characterized by an intense bleaching zone. Mineralogically, this rock type is very similar to the matrix of the mid subunit described above (Table 2), but is characterized by the absence of schlieren. Characteristic for this unit are medium-grained feldspars that form σ- and/or δ-clasts (Fig. 4f) as well as distinct EGM and catapleiite textures: In addition to fine-grained EGM in the matrix, larger poikilitic EGM porphyroclasts (Figs 3c, 4h and 6d) with abundant catapleiite (Figs 4h and 6d, Zr map), feldspar, nepheline and clinopyroxene inclusions occur, commonly surrounded by columnar rinkite-group minerals (Figs 4h and 6d). Furthermore, EGM in the outermost bleaching zones are partly to entirely replaced by zircon. Catapleiite forms up to 2 cm large, porphyroclasts (Fig. 4g) as well as elongated aggregates composed of anhedral, recrystallized catapleiite crystals (Fig. 7f). Clinopyroxene occurs as fine-grained euhedral to anhedral crystals rimed by a later clinopyroxene generation.

Other rock units

Arfvedsonite-aegirine meta-nepheline syenite (a.k.a. lakarpite)

Although being only a minor rock type restricted to the eastern contact of the mid subunit with the outer subunit (Fig. 2), this rock type is best known from the so-called *"discovery outcrop"* of the complex (Sjöqvist et al., 2013). This fine-to-medium-grained unit mainly consists of feldspar (35-60 wt.%), arfvedsonite (up to 20 wt.%), clinopyroxene (up to 15 wt.%) and EGM (up to 12 wt.%) with minor nepheline and natrolite. Feldspar-rich schlieren contain cm-sized, pinkish and mostly poikilitic EGM commonly surrounded by an amphibole- and clinopyroxene-rich matrix. Clinopyroxene forms elongated to euhedral crystals, most other minerals are anhedral to subhedral in their habit.

Table 1: List of investigated samples

Sample	Drill core	Position	Subunit	Analytical method (mineral)
5403	NKA 11054 P7	16.66-17.00m	Mid	MLA
5405	NKA 11054 P7	25.08-25.29m	Mid	MLA
5406	NKA 11054 P7	34.31-34.60m	Mid	MLA
5407-1	NKA 11054 P7	37.43-37.86m	Mid	MLA
5407-2	NKA 11054 P7	37.43-37.86m	Mid	MLA
5408	NKA 11054 P7	42.44-42.71m	Mid	MLA, EPMA (CPX, EGM, Cat, Ne, Fsp, Nat)
5409	NKA 11054 P7	45.85-46.20m	Mid	MLA
5411	NKA 11054 P7	54.56-54.78m	Mid	MLA
5611	NKA 11056 J1	110.20-110.34m	Outer	MLA, EPMA (CPX, EGM, Ne, Fsp)
5612	NKA 11056 J1	119.60-119.90m	Mid	MLA, EPMA (CPX, EGM, Ne, Fsp, Nat)
5613	NKA 11056 J1	126.00-126.25m	Mid	MLA, EPMA (CPX, EGM)
5618	NKA 11056 J1	198.60-198.86m	Mid	MLA, EPMA (CPX, EGM, Cat, Ne, Fsp, Nat)
5631	NKA 11056 J1	350.20-350.40m	Outer	MLA, EPMA (CPX)
6105	NKA 12061 J7	29.85-30.02m	Inner	MLA, EPMA (CPX, EGM)
6108	NKA 12061 J7	43.44-43.55m	Inner	MLA, EPMA (CPX, EGM)
6115	NKA 12061 J7	83.36-83.59m	Inner	MLA, EPMA (CPX, EGM, Ne, Fsp)
6123	NKA 12061 J7	163.61-163.80m	Outer	MLA, EPMA (CPX, EGM)
6124-1	NKA 12061 J7	182.30-182.56m	Outer	MLA, EPMA (CPX)
6124-2	NKA 12061 J7	182.30-182.56m	Outer	MLA
6125	NKA 12061 J7	189.90-190.30m	Outer	MLA
7305-1	NKA 12073 P5	~ 22.94m	Mid	MLA
7305-2	NKA 12073 P5	~26.50m	Mid	MLA
7308	NKA 12073 P5	52.81-52.97m	Mid	MLA, EPMA (CPX, EGM)
7310	NKA 12073 P5	64.37-64.51m	Mid	MLA
7311	NKA 12073 P5	71.35-71.43m	Mid	MLA
7314	NKA 12073 P5	89.44-89.57m	Mid	MLA
7315	NKA 12073 P5	91.50-91.61m	Mid	MLA, EPMA (CPX, EGM)
7320	NKA 12073 P5	156.31-156.44m	Outer	MLA

MLA = Mineral Liberation Analyzer; EPMA = Electron Probe Microanalyzer; CPX = clinopyroxene; EGM = Eudialyte-group minerals; Cat = catapleiite; Ne = nepheline; Fsp = feldspar; Nat = natrolite

Table 2: Modal mineralogy of subunits of the Norra Kärr complex

	Inner N=3				Mid (Matrix) N=1	Mid (Schlieren) N=17				Outer N=7			
	Mean	CI	95% Interval			Mean	CI	95% Interval		Mean	CI	95% Interval	
wt.%		(+/-)	Min	Max			(+/-)	Min	Max		(+/-)	Min	Max
Albite	22.88	4.15	13.27	31.66	57.87	4.43	0.84	0.00	21.83	39.66	1.44	29.73	53.85
Microcline	16.80	3.05	15.21	19.03	4.41	25.13	1.85	2.98	58.98	13.17	0.43	8.35	15.83
Aegirine	17.60	3.19	15.24	19.69	19.42	18.20	1.23	2.86	34.03	13.47	0.55	9.42	17.49
Nepheline	9.39	1.70	4.83	12.72	10.30	8.84	1.14	0.02	32.98	20.15	1.61	3.17	29.14
Natrolite	22.11	4.01	12.12	36.86	2.57	27.12	1.47	12.12	51.24	8.16	1.72	0.39	27.19
Catapleiite	1.74	0.32	0.94	2.19	2.97	2.45	0.23	0.10	6.29	1.13	0.14	0.14	2.63
Eudialyte	7.25	1.32	1.11	14.43	2.19	13.39	1.15	2.70	35.39	3.81	0.37	0.38	6.25
Other REE minerals	1.80	0.33	0.07	4.96	0.25	0.14	0.01	0.04	0.43	0.11	0.03	0.00	0.46

CI = confidential interval

Fluoro-leakeite-aegirine meta-nepheline syenite (a.k.a. kaxtorpite)

This fine-to-medium-grained rock with dark green to black colour was first described by (Adamson, 1944) and is located in the very centre of the intrusion (Fig. 2). The rock is variably deformed showing alignment of elongated minerals culminating in intense isoclinal folding and crenulated foliation (Fig. 4d). Most minerals are anhedral, elongated and aligned forming small alternating bands. The fine-grained matrix consists of albite, fluoro-leakeite (Oberti et al., 2015), pectolite, clinopyroxene, nepheline and natrolite (± catapleiite, titanite, fluorite and rosenbuschite) with large microcline augen preserved. The rock is commonly

interfolded with the surrounding inner subunit.

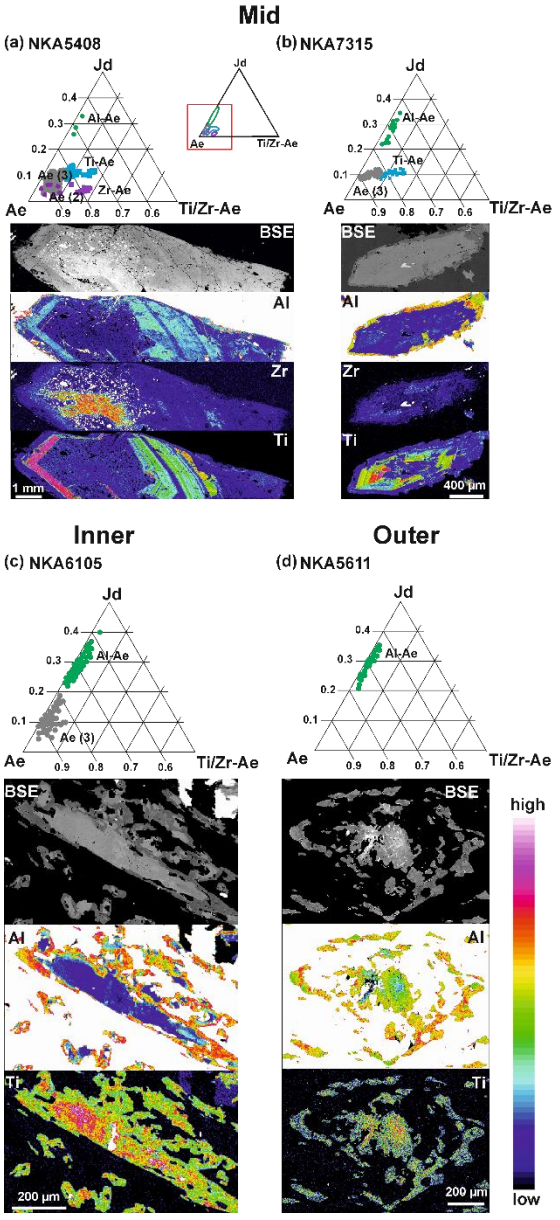

Fig.5. Compositional and textural characteristics of clinopyroxene from the Norra Kärr rocks. (a) Euhedral clinopyroxene from the mid subunit (sample 5408). The resorbed Zr-aegirine core (1) is irregularly rimmed by aegirine (2) rich in catapleiite inclusions. Both are overgrown by alternating sectors of inclusion-free titanoan-aegirine (4) and aegirine (3). Anhedral Al-aegirine (5) rims irregularly the crystal. (b) Subhedral clinopyroxene from the mid subunit exhibiting well defined Ti-rich sectors overgrown by Al-aegirine. In the center, a large catapleiite is enclosed. (c) Subhedral to anhedral clinopyroxene of the inner subunit; (d) Anhedral clinopyroxene from the outer subunit. See also detailed descriptions in the main text.

Aegirine-amphibole-biotite meta-nepheline syenite (a.k.a. pulaskite)

This rock is only present in the western and northern part of the complex, mostly forming elongated bodies in the outer subunit (catapleiite-bearing aegirine meta-nepheline syenite; Fig. 2). This unit is dark bluish and fine-to-coarse-grained with white to colourless feldspar schlieren and contains boudin-shaped pods (up to decimetre size) of mafic rocks not yet investigated in detail. The rock consists of large and anhedral microcline crystals embedded or engulfed in fine-to-medium-grained bands consisting of albite, clinopyroxene, biotite, amphibole ± fluorite. Most of these minerals are aligned, elongated and anhedral, only clinopyroxene and amphibole form euhedral crystals.

MINERAL COMPOSITIONS

Analytical techniques

Drill core samples were collected along two drill sections (J and P, nomenclature by Tasman Metals) at different depths of the intrusion (Fig. 2b and c). The investigated samples were selected to represent different styles of mineralization and degrees of alteration. Polished thick sections (120 µm) have been used for all analyses and a list of analyzed samples is given in Table 1.

Carbon-coated thick sections were studied by SEM-based Mineral Liberation Analyzer (MLA) and an Electron Probe Microanalyzer (EPMA) at the Helmholtz-Institute Freiberg for Resource Technology. The MLA studies used an FEI MLA Quanta 650F scanning electron microscope equipped with a field emission gun and two energy dispersive X-ray spectrometers (Bruker AXS Xflash® 5010) combined with image analysis software (Fandrich et al., 2007). Grain-based X-ray mapping (GXMAP) with resolution 500 x 500 pixels by a pixel size of 2µm with 5 pixel step size was applied at an acceleration voltage of 25 kV and a spot size of 5. The data was classified using the software package MLA Suite 3.0.

Electron Probe Microanalyzer measurements were performed with a JEOL JXA 8530F equipped with a field emission electron gun and five wavelength-dispersive spectrometers (WDS). Two of these spectrometers are provided with H-type crystals for high sensitivity and one with L-type crystals for good energy resolution. The X-ray element distribution maps were acquired with an acceleration voltage of 20 kV, a beam current of 50 nA, beam diameter of 14 µm and a dwell time of 140 ms. Aluminum, Y, Cl, and Ce were measured using the WDS, while Si, K, Ca, Mn, Zr, and Fe were measured with an energy dispersive spectrometer (EDS). Quantitative analyses of EGM were performed at an accelerating voltage of 20 kV and a beam current of 20 nA applying scanning mode as further details are described in Atanasova et al. (2015). Clinopyroxene, catapleiite, feldspar, nepheline and natrolite single point analyses were conducted at an accelerating voltage of 20 kV and a beam current of 20 nA. Only aggregated analytical results are reported in Tables 3-7. All detailed data is available on request by the senior author.

Clinopyroxene

Structural formula calculations for clinopyroxene are based on four cations and six oxygens, assuming stoichiometry. Average clinopyroxene analyses are given in Table 3. For classification we used the International Mineralogical Association (IMA/CNMMN) nomenclature (Morimoto et al., 1988; Rock, 1990) applying the classification diagram Jadeite (Jd) – Aegirine (Ae) – Quad (Q) with Quad (Q) being the sum of Ca-Mg-Fe pyroxene components (enstatite, ferrosilite, diopside and hedenbergite)

Table 3: Average compositions of the various clinopyroxene types of the Norra Kärr complex

	(1) Zr-aegirine				(2) Aegirine				(3) Aegirine				(4) Ti-aegirine				(5) Al-aegirine			
	Mean	CI	95% Interval		Mean	CI	95% Interval		Mean	CI	95% Interval		Mean	CI	95% Interval		Mean	CI	95% Interval	
wt.%	38		Min	Max	155		Min	Max	3053		Min	Max	541		Min	Max	1350		Min	Max
SiO_2	50.82	0.11	50.25	51.31	51.54	0.06	50.69	52.20	51.49	0.02	50.41	52.43	51.44	0.05	50.13	52.24	52.74	0.03	51.60	53.83
TiO_2	0.51	0.01	0.47	0.55	0.43	0.02	0.21	0.60	0.31	0.00	0.12	0.61	1.10	0.03	0.66	2.10	0.21	0.01	0.03	0.56
Al_2O_3	0.86	0.02	0.78	0.94	1.56	0.06	0.87	2.25	1.93	0.02	1.26	3.03	1.99	0.03	1.46	2.56	6.02	0.04	4.28	7.63
FeO	25.78	0.04	25.55	25.95	27.54	0.07	26.61	28.24	27.58	0.02	26.08	28.53	26.35	0.06	24.84	27.53	22.45	0.05	20.54	24.55
MnO	0.64	0.01	0.59	0.70	0.28	0.02	0.14	0.61	0.18	0.00	0.09	0.33	0.31	0.01	0.20	0.49	0.15	0.00	0.07	0.26
MgO	0.43	0.01	0.41	0.48	0.33	0.02	0.17	0.49	0.25	0.00	0.12	0.40	0.35	0.01	0.24	0.48	0.17	0.00	0.08	0.35
ZrO_2	3.20	0.02	3.11	3.28	0.44	0.03	0.15	0.94	0.29	0.01	0.05	0.92	0.53	0.03	0.08	1.69	0.08	0.00	0.02	0.20
CaO	1.61	0.03	1.50	1.77	1.02	0.04	0.61	1.57	0.81	0.01	0.34	1.53	0.60	0.02	0.36	1.01	0.74	0.01	0.32	1.31
Na_2O	11.84	0.05	11.54	12.13	12.32	0.04	11.73	12.95	12.43	0.01	11.86	12.90	12.52	0.02	12.11	12.86	12.76	0.01	12.20	13.26
K_2O	0.00	0.00	0.00	0.02	0.00	0.00	0.00	0.02	0.01	0.00	0.00	0.03	0.01	0.00	0.00	0.02	0.01	0.00	0.00	0.05
Total	95.69	0.14	94.98	96.39	95.45	0.08	94.48	96.35	95.27	0.02	93.78	96.44	95.19	0.06	93.52	96.56	95.33	0.04	93.87	96.50
Fe_2O_3	23.42	0.32	22.03	25.41	27.32	0.20	24.94	30.09	27.64	0.05	24.98	29.97	25.91	0.16	22.49	29.51	21.96	0.08	18.76	24.68
FeO	4.70	0.29	2.98	5.97	2.96	0.17	0.79	5.23	2.70	0.04	0.38	4.97	3.03	0.11	0.38	5.26	2.69	0.07	0.42	5.07
Ferric Total	98.04	0.14	97.31	98.94	98.19	0.08	97.22	99.19	98.04	0.02	96.59	99.22	97.79	0.06	96.37	99.00	97.53	0.04	96.04	98.73
Formulae based on 4 cations and 6 oxygens																				
Si	2.01	0.00	1.99	2.02	2.01	0.00	1.99	2.03	2.01	0.00	1.98	2.03	2.01	0.00	1.98	2.03	2.01	0.00	1.99	2.04
Al	0.04	0.00	0.04	0.04	0.07	0.00	0.04	0.10	0.09	0.00	0.06	0.14	0.09	0.00	0.07	0.12	0.27	0.00	0.19	0.34
Ti	0.02	0.00	0.01	0.02	0.01	0.00	0.01	0.02	0.01	0.00	0.00	0.02	0.03	0.00	0.02	0.06	0.01	0.00	0.00	0.02
Fe3+	0.70	0.01	0.66	0.75	0.80	0.01	0.73	0.88	0.81	0.00	0.73	0.88	0.76	0.00	0.66	0.87	0.63	0.00	0.54	0.71
Mg	0.03	0.00	0.02	0.03	0.02	0.00	0.01	0.03	0.01	0.00	0.01	0.02	0.02	0.00	0.01	0.03	0.01	0.00	0.00	0.02
Fe2+	0.16	0.01	0.10	0.20	0.10	0.01	0.03	0.17	0.09	0.00	0.01	0.16	0.10	0.00	0.01	0.17	0.09	0.00	0.01	0.16
Mn	0.02	0.00	0.02	0.02	0.01	0.00	0.00	0.02	0.01	0.00	0.00	0.01	0.01	0.00	0.01	0.02	0.00	0.00	0.00	0.01
Zr	0.06	0.00	0.06	0.06	0.01	0.00	0.00	0.02	0.01	0.00	0.00	0.02	0.01	0.00	0.00	0.03	0.00	0.00	0.00	0.00
Ca	0.07	0.00	0.06	0.08	0.04	0.00	0.03	0.07	0.03	0.00	0.01	0.06	0.02	0.00	0.01	0.04	0.03	0.00	0.01	0.05
Na	0.91	0.00	0.89	0.92	0.93	0.00	0.89	0.97	0.94	0.00	0.90	0.97	0.95	0.00	0.92	0.97	0.94	0.00	0.91	0.98
K	0.00	0.00	0.00	0.00	0.00	0.00	0.00	0.00	0.00	0.00	0.00	0.00	0.00	0.00	0.00	0.00	0.00	0.00	0.00	0.00
χ Ae	78.43	0.38	76.98	81.31	87.86	0.27	84.67	92.03	87.77	0.08	82.58	92.23	81.70	0.38	72.70	90.23	68.92	0.20	61.53	76.54
χ Jd	4.39	0.16	3.23	4.93	7.70	0.28	4.43	10.92	9.32	0.08	5.79	14.84	9.51	0.15	5.83	12.74	29.53	0.21	21.23	37.41
χ Ti-Zr-Ae	17.18	0.25	15.47	18.11	4.44	0.21	1.87	7.32	2.91	0.05	0.71	6.37	8.79	0.30	3.00	16.35	1.55	0.05	0.19	3.86

χ endmember composition of Ae (aegirine), Jd (jadeite and Ti/Zr-Ae (titanoan/zirkonian aegirine)

Table 4: Average compositions of the various types of eudialyte-group minerals in Norra Kärr rocks

	(1) Sector zoning				(2) Oscillatory zoning				(3) Irregular replacement textures				(4) Rims			
	Mean	CI	95% Interval		Mean	CI	95% Interval		Mean	CI	95% Interval		Mean	CI	95% Interval	
	321	(+/-)	Min	Max	180	(+/-)	Min	Max	374	(+/-)	Min	Max	139	(+/-)	Min	Max
SiO_2	51.56	0.05	50.59	52.36	51.09	0.04	50.49	51.57	51.20	0.08	49.95	52.55	50.91	0.11	49.69	51.85
TiO_2	0.16	0.00	0.08	0.22	0.09	0.00	0.06	0.14	0.16	0.00	0.07	0.21	0.12	0.01	0.04	0.20
ZrO_2	11.92	0.06	11.35	13.65	11.67	0.06	11.06	12.40	11.53	0.02	11.12	11.99	11.38	0.05	11.03	11.83
HfO_2	0.24	0.00	0.18	0.35	0.31	0.00	0.24	0.35	0.27	0.00	0.21	0.35	0.29	0.01	0.21	0.37
Al_2O_3	0.25	0.01	0.16	0.41	0.28	0.01	0.19	0.39	0.20	0.00	0.13	0.28	0.32	0.03	0.13	0.59
Nb_2O_5	0.50	0.02	0.21	0.85	0.74	0.02	0.47	1.07	0.94	0.03	0.44	1.54	0.89	0.05	0.30	1.36
La_2O_3	0.48	0.01	0.26	0.68	0.41	0.01	0.30	0.61	0.89	0.03	0.50	1.63	0.44	0.03	0.18	0.73
Ce_2O_3	1.32	0.02	0.79	1.63	0.95	0.03	0.74	1.45	2.01	0.05	1.07	2.86	0.98	0.07	0.40	1.63
Nd_2O_3+Pr_2O_3+Sm_2O_3	1.16	0.02	0.67	1.42	0.70	0.03	0.50	1.21	1.33	0.03	0.67	1.95	0.83	0.06	0.28	1.37
Tb_2O_3+Gd_2O_3+Dy_2O_3	0.69	0.01	0.32	0.88	0.68	0.01	0.56	0.79	0.67	0.01	0.48	0.89	1.03	0.03	0.76	1.29
Er_2O_3+Yb_2O_3	0.51	0.01	0.24	0.67	0.66	0.01	0.41	0.78	0.53	0.01	0.36	0.82	1.14	0.09	0.54	2.10
Y_2O_3	2.41	0.06	1.02	3.06	2.34	0.03	1.90	2.67	2.45	0.04	1.90	3.12	3.96	0.09	3.19	4.89
FeO	2.84	0.04	2.12	3.83	3.35	0.04	2.68	3.76	2.01	0.06	1.27	3.26	2.21	0.06	1.60	2.87
MnO	2.23	0.03	1.57	2.63	1.83	0.03	1.61	2.43	3.37	0.09	2.07	4.69	2.13	0.06	1.52	2.76
CaO	7.04	0.08	5.71	8.38	7.91	0.06	7.16	8.47	6.47	0.10	4.57	8.36	6.86	0.05	6.32	7.39
Na_2O	13.42	0.06	12.33	14.48	13.73	0.05	13.11	14.35	12.61	0.13	7.73	13.74	13.58	0.16	11.31	14.92
K_2O	0.46	0.01	0.19	0.63	0.35	0.01	0.21	0.51	0.50	0.01	0.26	0.95	0.46	0.02	0.28	0.73
Cl	0.36	0.01	0.29	0.59	0.68	0.03	0.31	0.93	0.35	0.01	0.28	0.88	0.41	0.02	0.23	0.56
O=Cl	0.08	0.00	0.07	0.13	0.15	0.01	0.07	0.21	0.08	0.00	0.06	0.20	0.09	0.00	0.05	0.13
Total, corrected	97.45	0.07	96.24	98.36	97.62	0.07	96.67	98.57	97.40	0.07	95.61	98.64	97.85	0.12	96.24	98.89
TREO total	4.16	0.06	2.79	4.89	3.40	0.05	2.98	4.45	5.43	0.09	3.76	6.97	4.41	0.08	3.52	5.22
Formula based on Σ(Si Al Zr Ti Hf Nb) normalized to 29 apfu																
Si	25.75	0.02	25.36	25.91	25.72	0.01	25.57	25.86	25.75	0.01	25.63	25.85	25.72	0.01	25.60	25.84
Ti	0.06	0.00	0.03	0.08	0.03	0.00	0.02	0.05	0.06	0.00	0.03	0.08	0.04	0.00	0.02	0.08
Zr	2.90	0.01	2.79	3.27	2.87	0.01	2.73	3.03	2.83	0.01	2.74	2.96	2.80	0.01	2.74	2.90
Hf	0.03	0.00	0.03	0.05	0.04	0.00	0.03	0.05	0.04	0.00	0.03	0.05	0.04	0.00	0.03	0.05
Al	0.15	0.00	0.09	0.23	0.17	0.00	0.12	0.23	0.12	0.00	0.07	0.16	0.19	0.02	0.08	0.35
Nb	0.11	0.00	0.05	0.19	0.17	0.01	0.11	0.25	0.21	0.01	0.10	0.35	0.20	0.01	0.07	0.31
La	0.09	0.00	0.05	0.12	0.08	0.00	0.06	0.11	0.17	0.01	0.09	0.30	0.08	0.01	0.03	0.14
Ce	0.24	0.00	0.14	0.30	0.18	0.00	0.14	0.27	0.37	0.01	0.20	0.54	0.18	0.01	0.07	0.30
Nd+Pr+Sm	0.21	0.00	0.12	0.26	0.13	0.00	0.09	0.22	0.24	0.01	0.12	0.36	0.15	0.01	0.05	0.25
Tb+Gd+Dy	0.06	0.00	0.03	0.07	0.06	0.00	0.05	0.07	0.06	0.00	0.04	0.07	0.09	0.00	0.06	0.11
Er+Yb	0.04	0.00	0.02	0.05	0.05	0.00	0.03	0.06	0.04	0.00	0.03	0.06	0.09	0.01	0.04	0.17
Y	0.64	0.01	0.27	0.81	0.63	0.01	0.51	0.72	0.66	0.01	0.51	0.83	1.07	0.03	0.85	1.32
Fe	1.19	0.02	0.88	1.59	1.41	0.02	1.13	1.59	0.85	0.02	0.54	1.38	0.93	0.03	0.67	1.20
Mn	0.94	0.01	0.67	1.11	0.78	0.01	0.68	1.04	1.43	0.04	0.90	2.02	0.91	0.03	0.65	1.17
Ca	3.77	0.04	2.98	4.49	4.27	0.03	3.84	4.60	3.48	0.05	2.50	4.55	3.72	0.03	3.40	4.03
Na	12.99	0.05	11.90	14.00	13.40	0.04	12.84	13.92	12.30	0.14	7.37	13.57	13.31	0.18	11.04	14.62
K	0.29	0.01	0.12	0.40	0.22	0.01	0.14	0.33	0.32	0.01	0.17	0.59	0.30	0.01	0.18	0.47
Cl	0.31	0.01	0.24	0.50	0.58	0.03	0.27	0.80	0.30	0.01	0.24	0.76	0.35	0.01	0.20	0.49

TREO total rare earth oxide

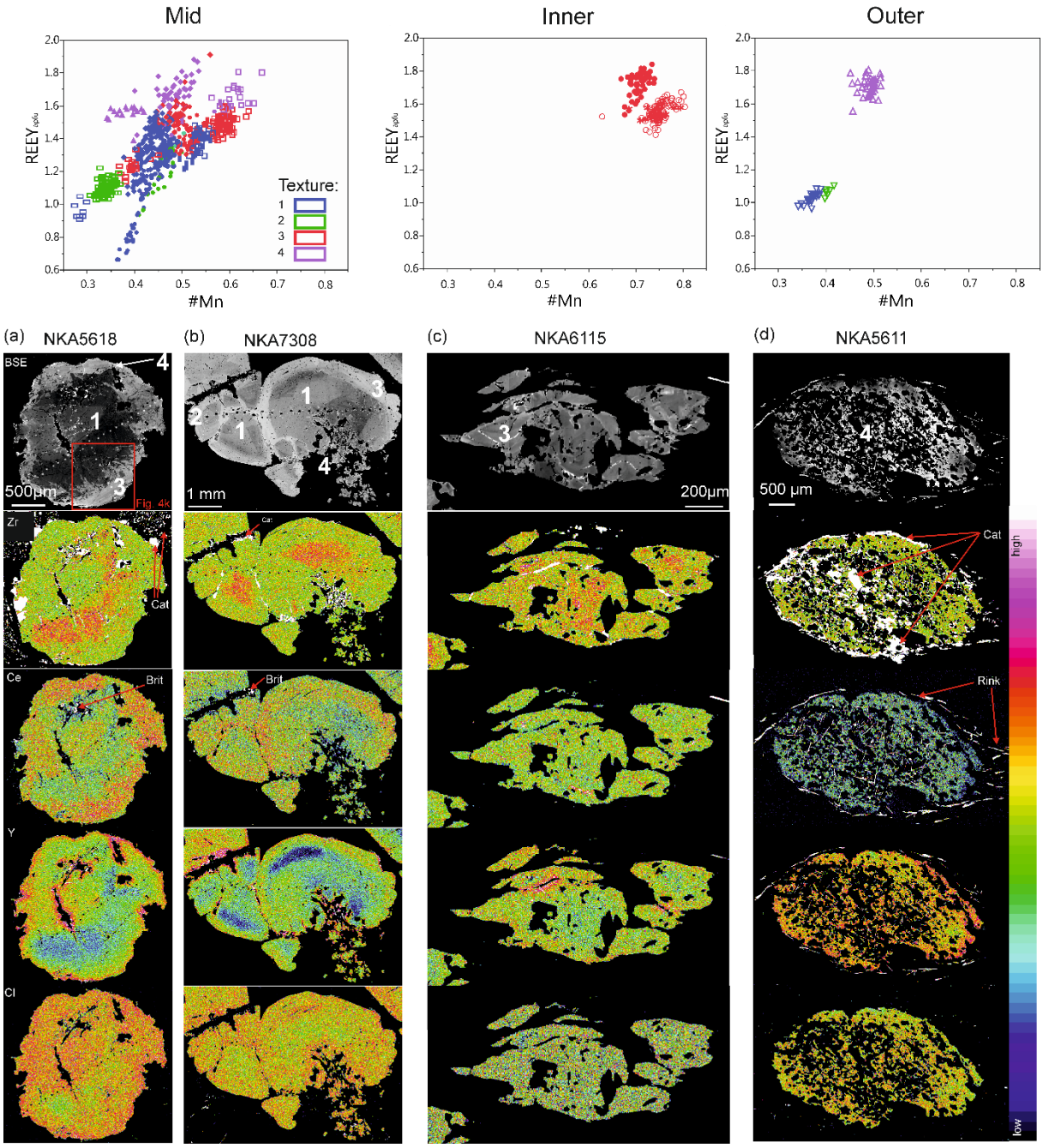

Fig.6. Compositional and textural characteristics of EGM from the Norra Kärr rocks. At the top of the diagram, textural varieties 1-4 from all EGM investigated are collated considering the #Mn and the REEYapfu. Representative grains of the different subunits are shown in (a)-(d). In the mid subunit (a) single EGM crystal (sample 5618) shows sectors (1) being Zr-rich, but REE-poor, overgrown by an irregular flamy area (3) of high BSE contrast, rich in REE and Y. Highest Y is detected along rims and cracks (4). The crystal is closely associated with catapleite (Cat) and britholite group minerals (Brit). Red box is enlarged in Fig. 4k. (b) Subhedral EGM featuring sector (1) and oscillatory (2) zoning, as well as irregular flamy textures (3) and poikilitic Y-rich areas (4). (c) EGM crystals from the inner subunit commonly show deformation features like stretching and alignment and are high in #Mn and REE. (d) Poikilitic EGM porphyroclast from the outer unit showing LREE depletion and Y enrichments at the rim. Catapleite (Cat) and rinkite group minerals (Rink) are visible as white areas in the Zr and Ce maps. Visible spots in (a) and (b) represent EPMA (white) and LA-ICP-MS (dark) measurement locations.

In the investigated samples, clinopyroxene is invariably sodic with a compositional range of $Jd_{2\text{-}40}Ae_{45\text{-}98}Q_{0\text{-}18}$ (Table 3, Fig. 8). Based on their textural

appearance (see above), we distinguish the following five varieties, showing distinct compositions in an aegirine – (Ti+Zr)aegirine – jadeite ternary (Fig. 5).

(1) Resorbed cores (Fig. 5a) of zirconian aegirine (Zr-Ae) with compositions of Ae_{68-75}Ti/Zr-$Ae_{14-16}Jd_{3-4}$ featuring high Zr (up to 0.06 apfu) but low Ti (<0.02 apfu) contents.

(2) Clinopyroxene areas containing anhedral catapleiite inclusions (Fig. 5a), having compositions of Ae_{77-88}Ti/Zr-$Ae_{2-7}Jd_{4-10}$ with low Zr and Ti (<0.01 apfu) contents.

(3) Subhedral to anhedral, needle- or columnar-shaped clinopyroxene (Fig. 5c) exhibiting compositions of Ae_{76-88}Ti/Zr-$Ae_{1-6}Jd_{5-14}$. Most of these data fall into the field for aegirine (sensu stricto) with Ae ≥ 80, some of the data indicate calcian aegirine (Q ≥10) and a notable number of analyzes represent aluminian aegirine (Jd >10; Fig. 8).

(4) Titanoan aegirine (Ti-Ae) with compositions of Ae_{67-87}Ti/Zr-$Ae_{3-15}Jd_{6-12}$ exhibiting low Zr (up to 0.03 apfu) but high Ti (up to 0.06 apfu) occurring as well-defined sectors and irregular areas (Fig. 5a-c).

(5) Aluminian aegirine (Al-Ae) with compositions of Ae_{56-75}Ti/Zr-$Ae_{1-5}Jd_{17-35}$ forming anhedral rims (Fig. 5a-c) and/or irregular patchy areas crosscutting clinopyroxene types (3) and (4).

The frequency of the different clinopyroxene types varies strongly throughout the complex: In the mid subunit (1)-(5) occur, but in samples from the inner and the outer subunits (1) and (2) are absent, while (4) is rarely present. While (3) and (5) occur in similar amounts in the inner unit, in the outer unit (5) predominates over (3) (Fig. 5d).The various clinopyroxene types are not only observed in the different subunits, but in single crystals too. As illustrated for samples 7315 and 6105 (Fig. 5b and c) from the inner unit, clinopyroxene (3) is anhedrally overgrown by (5). All five above-defined clinopyroxene types are present in a single crystal from the coarse-grained, undeformed schlieren (type B) of the mid subunit (sample 5408; Fig. 5a). Here, a Zr-aegirine core (1) is irregularly overgrown by aegirine (2) containing numerous anhedral catapleiite inclusions. Titanoan-aegirine sectors (4) and aegirine (3) overgrow this most central part of the crystal. Aluminian-aegirine (5) anhedrally rims the crystal.

Eudialyte-group minerals

Formula calculations for EGM were carried out by normalizing the sum of (Si + Zr + Ti + Nb + Al + Hf) to 29 apfu (Pfaff et al.,

2010). In total 91 EGM grains from 13 samples were analyzed.

The textural and compositional diversity of EGM analyzed is illustrated in Table 4 and Figs 3, 6 and 9. In common with clinopyroxene, four textural varieties of EGM, which show clear compositional differences are distinguished (Figs 6 and 9):

(1) Sector-zoned EGM enriched in Zr and depleted in REE and Nb.

(2) Oscillatory-zoned EGM that overgrow EGM (1); slightly enriched in Ca, Fe and Cl, but depleted in REE.

(3) Irregular, up to several tens of micrometers wide areas with bright BSE contrast, which replace and/or infiltrate EGM (1) and (2) (Fig. 4k). These are enriched in LREE and show highest #Mn and ∑REE.

(4) Few micrometers wide rims or areas around vugs and/or cracks being enriched in Y, HREE and #Mn, depleted in LREE with the highest ∑REEY and Nb.

In a given sample, sector and oscillatory-zoned EGM (1) and (2) are comparably REE-poor and exhibit low #Mn (defined as Mn/(Fe+Mn)), whereas types (3) and (4) are REE-rich and exhibit higher #Mn (Figs 6 and 9).

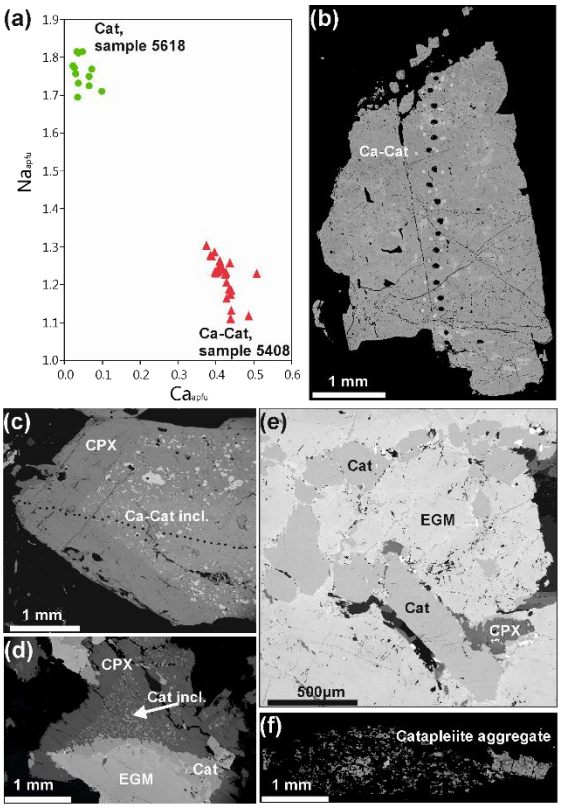

Fig.7. (a) Compositional and (b-f) textural characteristics of catapleite from the Norra Kärr rocks. (b) A single euhedral Ca-catapleiite crystal (Ca-Cat) and (c) Ca-catapleiite inclusions (Ca-Cat) in clinopyroxene (CPX), aegirine (2) (Fig. 4a) from schlieren of the mid subunit, sample 5408; (d) and (e) show characteristic catapleiite (Cat) and EGM textures in the mid subunit, sample 5618. Zones in radial aegirine (CPX), rich in catapleiite inclusions (Cat) are remarkably well defined. Catapleiite occurs enclosed in EGM, between and within EGM crystals and at the grain boundaries between clinopyroxene and EGM. (f) Catapleiite aggregates (Cat) from the outer subunit, sample 5611. Visible spots in (b) and (c) represent EPMA (white) and LA-ICP-MS (dark) measurement locations.

The most significant textural and compositional complexity is observed for EGM from schlieren of the mid subunit, as it was the case for clinopyroxene (see above). Sector-zoned EGM (1) is observed in samples 7308 and 5618 (Figs. 6a and b), where sectors with high BSE contrast are

richer in Zr, REE and Y compared to sectors with low BSE contrast. These most central parts of the crystals are overgrown either by oscillatory-zoned EGM (2) with comparably higher Si, Ca, MREE and HREE but low LREE (Fig. 6b) or by irregular shaped areas of type (3) with very high BSE contrast being enriched in REE and Y. Higher Y contents are documented at the rim of the crystals as well as in poikilitic areas of type (4).

EGM type (3) mainly occurs in the inner subunit. These are fine-grained, deformed and texturally less complex crystals with no significant compositional variation (Fig. 6c). They coexist with clinopyroxene types (3) and (5) (Fig. 5c) and have the highest LREE and Mn enrichments (Fig. 9). EGM in the outer subunit are fine-grained of types (1) and (2) or poikilitic type (4) (Fig. 6d). Poikilitic EGM have the lowest LREE content compared to all EGM studied and show a particular depletion of REE at the rims (Fig. 6d, BSE and Ce map).

Furthermore, regional compositional differences in EGM exist for Ca, Na, Y and the ΣHREE, where a general decrease from the outer to the inner subunit is present (Fig. 9). The opposite trend is noted for #Mn, ΣREE and ΣLREE, which increase from the border to the centre of the intrusion (Fig. 9). Niobium (apfu) and Zr/Hf ratios however, do not show such systematic changes, and Cl contents are mostly relatively low (Cl_{apfu} < 0.5), with one sample containing exceptionally Cl-rich EGM. These observations are in accordance with observations made by Sjöqvist et al. (2013).

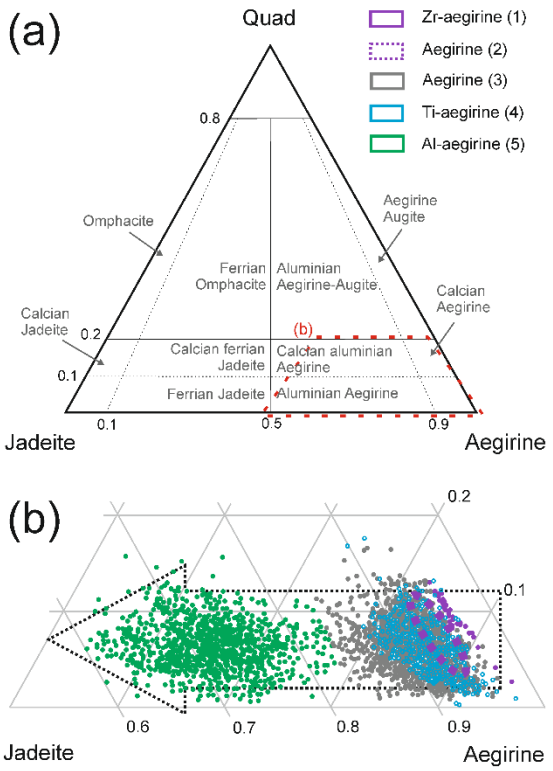

Fig.8. (a) Classification diagram for Ca-Na and Na pyroxenes with the endmembers Jadeite (Jd) – Aegirine (Ae) – Quad (Q) (modified after Morimoto et al., 1988; Rock, 1990). The marked area is enlarged in (b) showing that pyroxene compositions from Norra Kärr include aegirine s.s., zirconian aegirine, calcian aegirine, titanoan aegirine and aluminian aegirine.

Table 5: Catapeliite compositions from the Norra Kärr complex

	Ca-Catapleiite sample 5408, n=24				Catapleiite sample 5618, n=12			
	Mean	CI	95% Interval		Mean	CI	95% Interval	
wt %		(+/-)	Min	Max		(+/-)	Min	Max
SiO_2	45.85	0.18	45.04	46.53	46.54	0.16	46.18	46.93
TiO_2	0.02	0.00	0.01	0.03	0.03	0.01	0.02	0.05
ZrO_2	29.07	0.09	28.61	29.39	29.92	0.37	27.80	29.56
HfO_2	0.59	0.07	0.47	0.91	0.69	0.06	0.54	0.83
$REEY_2O_3$	0.41	0.03	0.30	0.56	0.46	0.05	0.31	0.58
FeO	0.20	0.13	0.04	0.95	1.10	0.55	0.10	2.80
CaO	5.99	0.18	5.41	6.99	0.68	0.20	0.35	1.30
Na_2O	9.55	0.16	8.75	10.14	13.83	0.23	13.30	14.33
K_2O	0.04	0.01	0.01	0.09	0.05	0.02	0.02	0.10
Total	91.71	0.31	90.63	93.14	92.30	0.38	91.66	93.27
H_2O (calc)	7.44	0.02	7.37	7.49	7.76	0.02	7.70	7.78
Total (incl H_2O)	99.15	0.31	98.10	100.56	100.06	0.39	99.37	101.08
Formulae based on 10 cations and 11 oxygens								
Si	3.02	0.00	3.00	3.04	3.06	0.01	3.05	3.07
Ti	0.00	0.00	0.00	0.00	0.00	0.00	0.00	0.00
Zr	0.93	0.00	0.92	0.94	0.93	0.01	0.89	0.95
Hf	0.01	0.00	0.01	0.02	0.01	0.00	0.01	0.02
REEY	0.01	0.00	0.01	0.01	0.01	0.00	0.01	0.01
Fe	0.01	0.01	0.00	0.05	0.06	0.03	0.01	0.15
Ca	0.42	0.01	0.38	0.50	0.05	0.01	0.02	0.09
Na	1.22	0.02	1.11	1.29	1.76	0.03	1.70	1.82
K	0.00	0.00	0.00	0.01	0.00	0.00	0.00	0.01
H (calc)	3.76	0.01	3.72	3.78	3.92	0.01	3.89	3.95

CI = confidential interval

Table 6: Average feldspar compositions in metasyenites from the Norra Kärr complex

	Microcline n=338				Albite n=122			
	Mean	CI	95% Interval		Mean	CI	95% Interval	
wt %		(+/-)	Min	Max		(+/-)	Min	Max
SiO_2	65.03	0.03	64.39	65.44	69.44	0.04	68.92	69.87
Al_2O_3	18.99	0.01	18.76	19.18	19.54	0.02	19.32	19.72
FeO	0.10	0.01	0.01	0.34	0.09	0.01	0.00	0.23
BaO	0.06	0.00	0.00	0.12	0.03	0.00	0.00	0.07
CaO	0.00	0.00	0.00	0.01	0.00	0.00	0.00	0.01
Na_2O	0.38	0.02	0.06	0.60	11.85	0.03	11.56	12.11
K_2O	17.15	0.03	16.81	17.64	0.10	0.01	0.05	0.17
TOTAL	101.70	0.04	100.81	102.26	101.06	0.06	100.36	101.70
Formulae based on 32 oxygens								
Si	12.03	0.01	11.92	12.11	12.74	0.01	12.64	12.82
Al	4.14	0.00	4.09	4.18	4.22	0.00	4.18	4.26
Fe^{2+}	0.02	0.00	0.00	0.05	0.01	0.00	0.00	0.03
Ca	0.00	0.00	0.00	0.00	0.00	0.00	0.00	0.00
Na	0.14	0.01	0.02	0.21	4.22	0.01	4.11	4.31
K	4.05	0.01	3.97	4.16	0.02	0.00	0.01	0.04
Ba	0.00	0.00	0.00	0.01	0.00	0.00	0.00	0.01
X_{An}	0.01	0.00	0.00	0.05	0.02	0.00	0.00	0.06
X_{Ab}	3.23	0.15	0.52	5.12	99.42	0.05	99.08	99.69
X_{Or}	96.76	0.15	94.88	99.45	0.56	0.05	0.28	0.91

X endmember composition of An (anorthite), Ab (albite) and Or (orthoclase)

Table 7: Average nepheline, natrolite and analcime compositions from Norra Kärr rocks

	Nepheline N=108				Natrolite N=104				Analcime N=4			
	Mean	CI	95% Interval		Mean	CI	95% Interval		Mean	CI	95% Interval	
wt %		(+/-)	Min	Max		(+/-)	Min	Max		(+/-)	Min	Max
SiO_2	42.23	0.16	41.45	43.25	47.66	0.06	47.18	48.99	50.17	7.24	46.77	52.30
Al_2O_3	34.27	0.13	33.41	34.92	27.39	0.09	26.69	28.11	26.30	4.60	25.12	28.35
Fe_2O_3	0.12	0.02	0.04	0.33	0.13	0.04	0.00	0.44	0.13	0.23	0.04	0.23
BaO	0.04	0.00	0.00	0.09	0.03	0.00	0.00	0.07	0.04	0.07	0.01	0.06
CaO	0.02	0.02	0.00	0.27	0.01	0.01	0.00	0.06	0.03	0.03	0.02	0.03
Na_2O	16.08	0.10	14.92	16.52	15.24	0.04	14.92	15.60	13.50	2.64	12.25	14.17
K_2O	7.59	0.10	6.87	8.03	0.06	0.01	0.01	0.15	0.53	1.49	0.05	1.10
Total	100.35	0.09	99.66	101.07	90.53	0.12	89.52	91.66	90.71	5.05	88.51	92.52
	Formulae based on 16 oxygens				Formulae based on 10 oxygens				Formulae based on 6 oxygens			
Si	0.70	0.00	0.69	0.72	3.01	0.00	2.98	3.03	1.90	0.27	1.77	1.98
Al	0.67	0.00	0.66	0.69	2.04	0.01	1.99	2.09	1.17	0.21	1.12	1.27
Fe^{3+}	0.00	0.00	0.00	0.00	0.01	0.00	0.00	0.02	0.00	0.01	0.00	0.01
Ca	0.00	0.00	0.00	0.00	0.00	0.00	0.00	0.00	0.00	0.00	0.00	0.00
Na	0.52	0.00	0.48	0.53	1.87	0.01	1.83	1.91	0.99	0.19	0.90	1.04
K	0.16	0.00	0.15	0.17	0.00	0.00	0.00	0.01	0.03	0.07	0.00	0.05
B	-	-	-	-	0.00	0.00	0.00	0.00	0.00	0.00	0.00	0.00

CI = confidential interval

Catapleiite

Structural formula calculations for catapleiite are based on 10 cations and 11 oxygens, assuming stoichiometry. Representative compositions are given in Table 5 and Fig. 7a. Catapleiites from two samples of the mid subunit were analyzed. In sample 5408 both textural varieties of Ca-catapleiite, namely coarse-grained subhedral crystals (Fig. 7b) and fine-grained anhedral inclusions in clinopyroxene (Fig. 7c) have very similar compositions with up to 7 wt.% CaO (Table 5). Similarly, in sample 5618 catapleiite occurrences at the border area between clinopyroxene and EGM and catapleiite inclusions in clinopyroxene (Fig. 7d and e) exhibit quite similar compositions with CaO between 0.3 and 1.3 wt.% and Na_2O between 13.0 and 14.0 wt.% (Table 5).

Feldspars, feldspathoids and zeolithes

Feldspars occur in all investigated samples as distinct albite and microcline grains and no perthitic exsolution textures were observed. There are no significant differences between the various samples and units with albite being almost pure (< 1 mol.% microcline) and microcline containing up to 5 mol.% albite (Table 6).

Nepheline compositions ($Ne_{74-77}Ks_{21-25}An_0Qz_{0-1}$) in all samples are very similar (Table 7). According to the diagram (Hamilton, 1961), the majority of analyses plot between the ideal compositions of Morosewicz (M) and Buerger (B) (Fig. 10) and generally fall below the isotherm at T = 700ºC, with two exceptional analyses indicating T > 775ºC.

Albite and nepheline are variably replaced by zeolithes. Natrolite is largely dominant and shows a very restricted compositional variation. Analcime was found only in one sample (Table 7).

DISCUSSION

The aim of this study is to distinguish the magmatic signature of an agpaitic complex from features related to subsequent deformation and metamorphism using mineral textures and compositions. In the course of the study, minerals of the feldspar-group and nepheline were proven less beneficial probably due to their relatively simple structure and composition. In contrast, structurally and compositionally more complex minerals of the eudialyte-group, catapleiite as well as clinopyroxene appeared more appropriate to reflect physico-chemical changes.

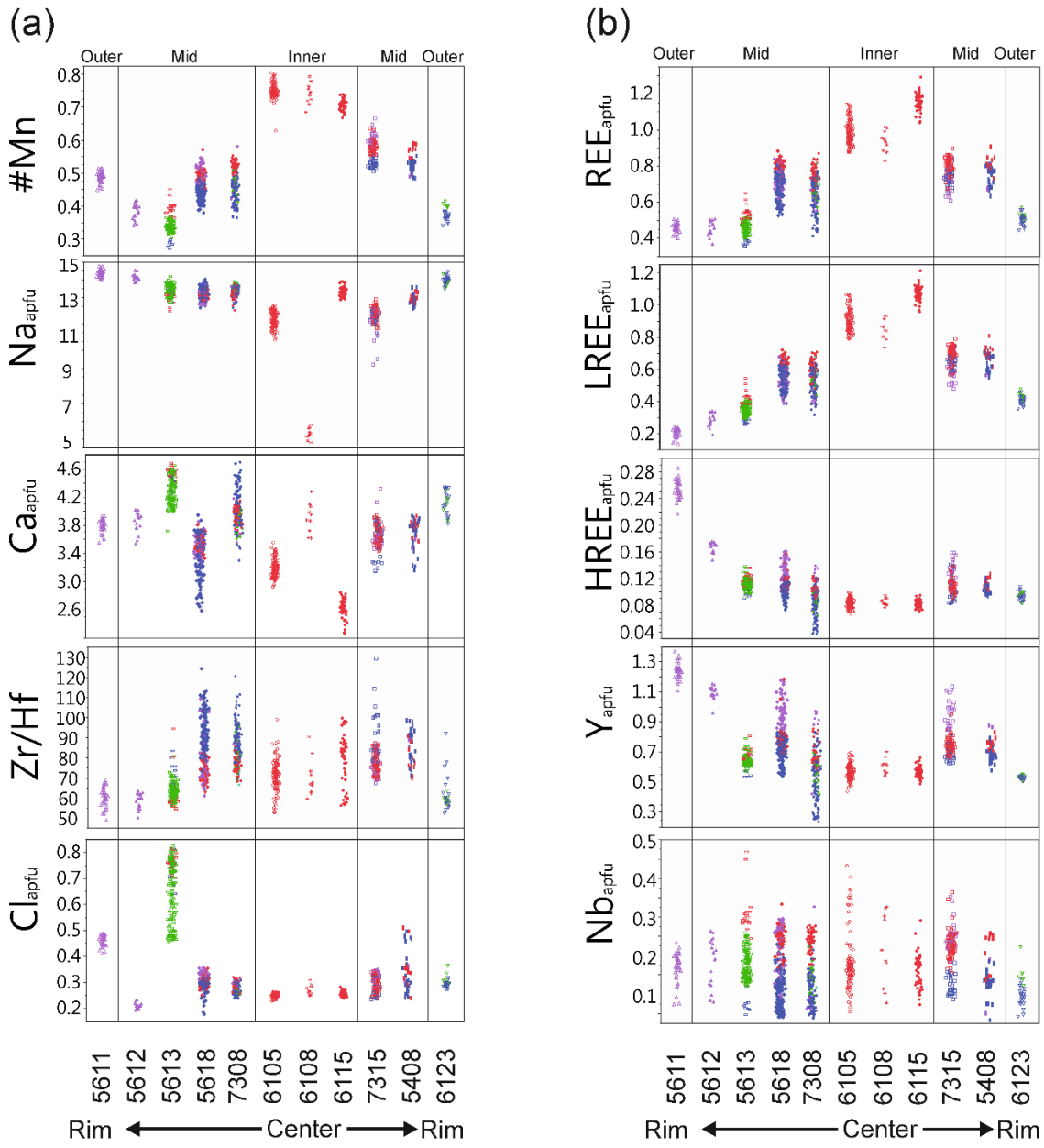

Fig.9. Distribution of (a) major and (b) minor elements in EGM according to the relative sampling location within the fold structure. Colour coding displays EGM textural varieties 1-4 as defined in Fig. 5 and I the main text.

Discrimination between magmatic and metamorphic features

The agpaitic Norra Kärr complex was subsequently overprinted and deformed during two successive orogenic events and is now preserved in a well-defined syncline with near parallel occurrence of major rock units (Fig. 2b und c). In the following we assign the various textures and compositions of the rock forming minerals to either magmatic relics or metamorphic features in order to reconstruct the

magmatic and the subsequent metamorphic history of the Norra Kärr rocks.

Preserved magmatic features

Feldspars from the Norra Kärr rocks do not exhibit perthite or antiperthite textures preserved (in agreement with Adamson, 1944). We take this as evidence for the crystallization from a subsolvus (low T) syenite (Chakrabarty et al., 2016a; Larsen and Sørensen, 1987; Markl et al., 2001; Markl and Baumgartner, 2002; Sood and Edgar, 1970). Alternatively, this could also reflect the metamorphic recrystallization, but considering the observation that even feldspar inclusions in EGM and clinopyroxene represent near end member compositions, a primary subsolvus origin is considered most probable. This hypothesis is further supported by temperatures derived from nepheline compositions, which generally do not exceed 700ºC (Fig. 10). The two exceptional nepheline compositions that indicate T > 775°C might represent early magmatic (phenocrystic) relict nepheline.

Relics of an early magmatic crystallization stage of the Norra Kärr rocks might be represented by the Zr-aegrine cores of clinopyroxene (1) (Figs 5a and 7c). At constant P and T, Zr-aegirine is stable at moderate a_{Nds} (activity of $Na_2Si_2O_5$) and under relatively reducing conditions (Andersen et al., 2012). At this stage clinopyroxene could act as a sink for Zr, preventing the crystallisation of early magmatic Zr-silicates. Similar relic clinopyroxene crystals were reported from the deformed Red Wine intrusion (Currie and Curtis, 1976), resulting from the large stabilitiy field of clinopyroxene and its ability to adapt its composition to the prevailing P-T-X conditions.

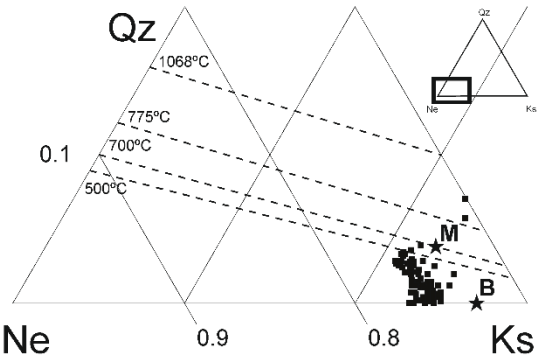

Fig.10. Diagram of the system nepheline-kalsilite-silica (wt.%) with isotherms showing the limit of nepheline solid solution at the indicated temperatures (Hamilton, 1961). The majority of analyses plot within the Morosewicz (M) – Buerger (B) convergence field (Tilley, 1954). Most of the analyses indicate T ≤ 500ºC. Only two analyses indicate T ≥ 700ºC.

Table 8: Reintegrated compositions of Zr-aegirine (based on the composition, frequency and molar volumes of catapleite and aegirine s.str.) compared with measured compositions of Zr-aegirine core from sample 5408

		Reintergrated	Measured
Vol %	1	2	
Cpx	89	84	
Catapleiite	11	16	
SiO_2	51.07	50.94	50.83
TiO_2	0.51	0.49	0.50
Al_2O_3	1.13	1.10	0.85
FeO	25.93	25.15	25.78
MnO	0.34	0.33	0.64
ZrO_2	2.11	2.96	3.21
CaO	1.20	1.17	1.63
Na_2O	12.25	12.30	11.83
K_2O	0.01	0.01	0.00
Total	94.55	94.46	95.27

Subsequent destabilization of Zr-aegirine (Fig. 7c and d) results in the exsolution of catapleiite and Zr-poor clinopyroxene (2). The catapleiite inclusions occur in well-defined areas in clinopyroxene and are characterized by irregular shapes (Figs 5a and 7c). This process happened probably due to an increase of a_{Nds}, a_{H2O} or f_{O2} during a later crystallization stage and can be described by the schematic reaction:

$4Na[Zr_{0.5}\ Fe_{0.5}]Si_2O_6$ (Zr-Aegirine) + $Na_2Si_2O_5$ + $½O_2$ + $4H_2O$ = $2NaFeSi_2O_6$ (Aegirine) + $2Na_2ZrSi_3O_9 * 2H_2O$ (Catapleiite) (1)

This hypothesis was tested by reintegrating the Zr-aegirine composition, using the molar volumes of catapleite inclusions contained in well-defined areas of aegirine (2) (Fig. 7d) as well as measured mineral compositions (Tables 3 and 5). Reintegrated Zr-aegirine compositions correspond very well with measured compositions (Table 8) supporting the argument for catapleiite formation by Zr-aegirine destabilization and subsequent exsolution. Considering the textural relationships illustrated in Fig. 7e, we further assume that catapleiite crystallized prior to EGM, forming euhedral crystals, which were later encased in EGM. In contrast, the textural relationships illustrated in Fig. 7d provide evidence that both minerals may have replaced each other. In addition, it is not clear, if the above-described catapleite exsolutions in clinopyroxene and coarse, euhedral catapleite intergrown with EGM represent different stages during the magmatic evolution of these rocks. Indeed, they may be two different generations. Compositionally, however, there are no differences between these two types of catapleiite (Fig. 7a). In general, both catapleiite and EGM occur in Zr-rich peralkaline magmatic systems. However, the formation of magmatic EGM seems to require relatively low water activities, but high Cl activities, conditions that are typically met in reduced nepheline syenitic systems, whereas magmatic catapleiite seems to be restricted to peralkaline (granitic) systems being relatively H_2O-rich (Andersen et al., 2010; Andersen and Friis, 2015; Marks et al., 2011). Note that catapleiite can also form (along with many other phases) during the hydrothermal alteration of EGM (Borst et al., 2016; Karup-Møller et al., 2010; Karup-Møller and Rose-Hansen, 2013; Salvi et al., 2000). The catapleiite-eudialyte equilibrium can be expressed by the following schematic reaction:

$3Na_2ZrSi_3O_9$ (Catapleiite) * $2H_2O$ + $6CaO$ + $4Na_2O$ + $NaCl$ + $3FeO$ + $17SiO_2$ =

$Na_{15}Ca_6Fe_3Zr_3Si_{26}O_{72}(OH)_4Cl$ (Eudialyte) + $4H_2O$ (2).

The Cl contents in EGM from the Norra Kärr rocks mostly vary between 0.2-0.4 apfu (Fig. 9a) and are relatively low compared to EGM in other alkaline complexes with Cl_{apfu} up to 1.9 (J Schilling et al., 2011). EGM from Norra Kärr may contain up to about 3 wt.% H_2O (Atanasova et al., 2015). This implies that EGM may be stable even at relatively low a_{HCl} but relatively high a_{H2O}. We propose that in the case of Norra Kärr a_{H2O} was not high enough to stabilize catapleiite over a long crystallization interval. In addition, initial catapleiite formation lead to subsequent REE enrichment of the melt, which probably was the crucial promoting factor stabilizing EGM in this relatively Cl-poor environment.

On the deposit scale, we observe a continuous decrease in Ca, Na, Y and the HREE with increasing #Mn, ΣREE and LREE in EGM from the outer to the inner subunit as demonstrated in Fig. 9. Such compositional changes of EGM are attributed to primary magmatic evolution (Sjöqvist et al., 2013) also known from EGM-bearing layered intrusions (Lindhuber et al., 2015; Möller and Williams-Jones, 2016; Pfaff et al., 2008; Ratschbacher et al., 2015; Julian Schilling et al., 2011a; Sheard et al., 2012). Early magmatic EGM are enriched in Fe and the HREE, which leads to subsequent Mn- and-LREE-enrichment of the residual melt and to crystallization of late magmatic Mn- and LREE-dominated EGM. The compositional evolution in terms of the Mn/(Fe+Mn) ratio as well as the content of the different REE are both considered to be the result of fractional crystallization during primary, magmatic layering of agpaitic intrusions(Lindhuber et al., 2015; Möller and Williams-Jones, 2016; Pfaff et al., 2008; Ratschbacher et al., 2015; Julian Schilling et al., 2011a; Sheard et al., 2012). Similarly, primary layering of the Norra Kärr complex (Fig. 11), as indicated by early Fe- and- HREE-dominated EGM from the outer subunit as well as by continuous Mn and LREE enrichment in the mid and inner subunits (Fig. 11) and are still preserved within the fold structure.

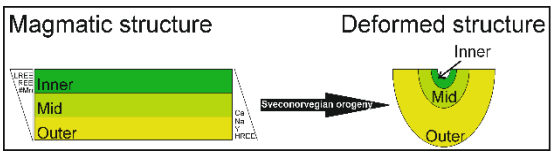

Fig.11. Suggested primary magmatic layering of the intrusion with upwards enrichment of REE, LREE and #Mn, preserved within the present fold structure.

Textures assigned to metamorphic overprint

The magmatic textures described above such as sector and oscillatory zoning in clinopyroxene and EGM are partly-

overgrown and/or replaced by late anhedral Al-aegirine and REE-enriched EGM, respectively. The formation of Al-aegirine is a general feature of metamorphosed syenites (Woolley et al., 1996) and is probably formed by the following schematic reaction (Curtis and Gittins, 1979):

$NaAlSiO_4$ (Nepheline) + $NaAlSi_3O_8$ (Albite) = 2 $NaAlSi_2O_6$ (Jadeite) (3).

Same reaction is observed in samples studied from Norra Kärr as well. According to Curtis and Gittins (1979) equation (3) could take place in a huge P- and T-range of conditions, between 450-700°C and 2-10 kbars, covering both, higher greenshist and lower-to-moderate amphibolite facies conditions. In contrast to Red Wine, where amphibolite facies conditions are reported, at Norra Kärr moderate-to-high greenshist facies conditions are only roughly estimates. These estimates are supported by the observation that relic magmatic textures are preserved due to assumed relatively low P and T during deformation of the rocks (Woolley et al., 1996).

In EGM, flamy BSE textures (Figs 4k, 6a and b) as well as very late Y enrichments and LREE depletions at the rim of crystals, along cracks, vugs (Figs 6a, b and d) and in highly poikilitic areas (Figs 6b and d) are observed. Flamy textures as shown in Fig. 4k indicate both, new formation of compositionally different EGM of type 3, (straight boundaries between EGM (1) and (3)) as well as recrystallization or replacement of EGM types (1) and/or (2) by EGM of type (3) (flamy EGM (3) permeating EGM (1) and/or (2)). Both can be explained by the interaction with fluids, presumably generated during the metamorphic overprint of the rocks. Yttrium and HREE enrichments accompanied by LREE depletion at the rims of crystals (Fig. 6a, b and d) might document an even later event causing further compositional adaptation of EGM, in this case accompanied by the re-distribution of REE and Y, spatially-associated with the formation of late catapleiite and secondary LREE-rich minerals (Fig. 6a, Ce map). We suggest that these textures could potentially be caused by recrystallization of EGM in response to metamorphic deformation.

The widespread alteration of albite and nepheline to natrolite (Fig. 3) is also a late process, probably related to fluid-assisted overprint during deformation. Importantly, analcime is only very rarely observed (actually in only one sample, see above). This corresponds to observations from the Mont Saint-Hilaire complex (Julian

Schilling et al., 2011a) and Shushina Hill (Chakrabarty et al., 2016b), where it was suggested that under such conditions analcime is only stable at low T < 150°C. Accordingly, this argues for higher temperatures for natrolite formation. In the case of Norra Kärr a further indication for the "metamorphic" origin is given by the spatial distribution of natrolite alteration, which preferably occurs in the mid and inner units, while the very fine-grained rocks from the outer unit are less affected, although these rocks are in direct contact with the granitic country rock.

Thermodynamic modelling to constrain the p-T-conditions

The albite – nepheline – aegirine assemblage of the Norra Kärr rocks permit estimations of temperature and silica activity at the assumed pressure of the magmatic stage (Markl et al., 2001; Mitchell and Platt, 1978; Julian Schilling et al., 2011b) and may shed light into the so far poorly constrained conditions during metamorphic overprint during the Sveconorvegian (Grenvillian) orogeny. We performed thermodynamic calculations applying the GEOCALC software of Berman et al. (1987) and Liebermann and Petrakakis (1991) with the database of Berman (1988) using the following three schematic equilibria.

$NaAlSiO_4$ (Nepheline) + SiO_2 (liq) = $NaAlSi_2O_6$ (Jadeite) (4)

$NaAlSi_2O_6$ (Jadeite) + SiO_2 (liq) = $NaAlSi_3O_8$ (Albite) (5)

$NaAlSiO_4$ (Nepheline) + $2SiO_2$ (liq) = $NaAlSi_3O_8$ (Albite) (6)

End member activities were calculated using a one-site mixing model for nepheline and applying the solution activity formulations of Green et al. (2007) Holland and Powell (2003) for clinopyroxene and feldspar, respectively.

Assuming typical emplacement pressures of 1-2 kbars for syenitic peralkaline intrusions (Konnerup-Madsen and Rose-Hansen, 1982; Salvi et al., 2000) and using the mean compositions of Zr-aegirine (1), which we interpret as early magmatic clinopyroxene (see above), equilibrium conditions of 600 - 700°C at aSiO2 values of 0.5-0.6 are indicated (Fig. 12a). Such conditions are consistent with estimations for other peralkaline complexes and are in agreement with the absence of perthitic alkali feldspar (see above) and the temperature estimates based on nepheline thermometry (Fig. 10). Compositions of presumably late-magmatic aegirine (2) and (3) indicate equilibration to lower temperatures (< 450°C) and a_{SiO2} values of < 0.3 (Fig. 12a).

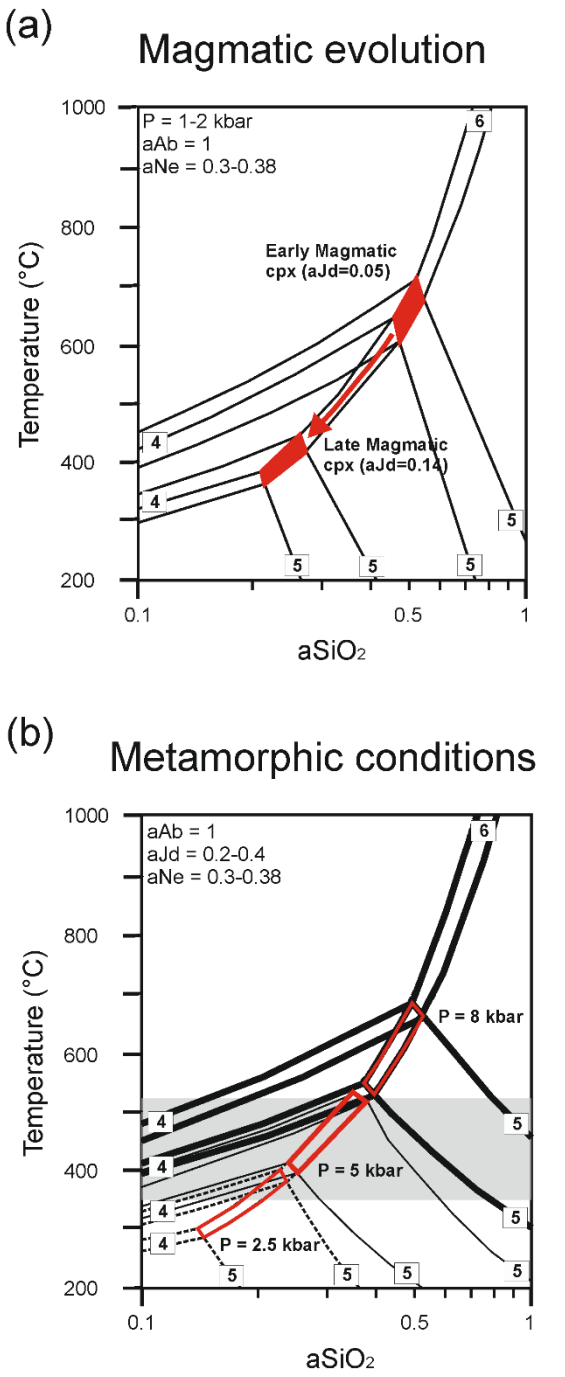

Fig.12. Two silica activity (aSiO2) - temperature diagrams calculated based on equilibria (4)-(6). Different sets of conditions (different lines in (b)) are calculated due to variable activities of nepheline (aNe) and jadeite (aJd), while the activity of albite (aAb) is 1 for all reactions. (a) Magmatic conditions are estimated for 1-2 kbars using early- and late-magmatic clinopyroxene compositions, respectively. (b) The metamorphic evolution of the Norra Kärr complex is illustrated for pressures representing general greenshist (grey area) to lower amphibolite facies conditions, considering compositions of metamorphic clinopyroxene. Details are given in the main text.

Taken together, we interpret these data as representing the magmatic evolution of the Norra Kärr rocks, indicating a relatively low liquidus temperature of <700°C and a relatively extensive crystallization interval down to temperatures < 400°C, which has been demonstrated before, based on both field studies (Markl et al., 2001; Marks et al., 2003; Marks and Markl, 2003) and experimental work (Giehl et al., 2014, 2013; Piotrowski and Edgar, 1970; Sood and Edgar, 1970).

To constrain the metamorphic conditions of the Norra Kärr rocks during the Sveconorvegian orogeny, we used the mean compositions of Al-aegirine (clinopyroxene 4; see above) computed at pressures of 2.5, 5 and 8 kbars to represent general greenshist as well as lower amphibolite facies conditions (Fig. 12b). The calculated equilibrium temperatures range from 350 to 650°C with a_{SiO2} values from 0.55 to 0.15, with both T and a_{SiO2} decreasing with decreasing pressure. Comparing these estimates with proposed moderate-to-high greenschist facies conditions, temperatures from 400 to 550°C at pressure of 5 kbars with an a_{SiO2} range between 0.25 and 0.4 are considered as most reasonable. These values are similar to those estimated for late magmatic conditions. This might indicate that a_{SiO2} during the metamorphic stage did not essentially change, suggesting that fluid-rock interaction during this stage was

largely (locally) rock-buffered and that the responsible fluids were not especially SiO_2-rich, as there is no late-stage quartz formed as might be expected from fluids derived from granitic country rocks.

CONCLUSIONS

Even after metamorphic overprint and deformation, it remains possible to identify primary magmatic textures and compositions in EGM and clinopyroxene from peralkaline rocks and to find evidence for primary magmatic layering of the intrusion with continuous enrichment of REE, LREE and Mn from the outer to the inner subunit. The multi-stage evolution of such rocks can be reconstructed using clinopyroxene and EGM, as both minerals cover a large stability range (in term of P and T) and are able to adapt their composition to changing conditions, thereby recording the magmatic and metamorphic history of the complex.

The minerals investigated probably crystallized from a subsolvus syenite and crystallization took place during a relatively extensive temperature interval from about 700ºC to 450ºC with a correspondent decrease in a_{SiO2} from 0.6 to about 0.3. Initially, Zr-aegirine crystallized at relatively low peralkalinity and reducing conditions. Due to an increase in a_{Nds} and at moderate-to-high f_{O2} and a_{H2O}, Zr-aegirine was destabilized and crystallization continued forming aegirine (2) of sensu stricto compositions and catapleiite as the main Zr-bearing silicate mineral. Due to the absence of sodalite and the very early formation of catapleiite, a_{HCl} further increased and REE and HFSE were enriched in the residual melt, promoting EGM crystallization. Crystallization of EGM seems not necessarily restricted to specific conditions, forming even at very low a_{HCl} and at relatively high a_{H2O}, but to the availability of specific elements in the melt.

During the Sveconorvegian / Grenvillian orogeny, the Norra Kärr rocks were deformed and folded at presumably moderate greenshist facies conditions (Fig. 12) and late EGM and Al-aegirine formed at 400 - 550ºC and in an a_{SiO2} range of 0.25-0.4 at pressures not exceeding 5 kbars. We suggest that during this deformation event EGM interacted with metamorphic fluids, either changing its composition or being partly-destabilized to catapleiite and secondary REE-bearing minerals. During the whole history of the complex, a_{SiO2} remains very similar, indicating very little interaction with the surrounding granitic rocks. This assumption is confirmed by the relatively restricted occurrence of natrolite

alteration, preferably occupying the more central part of the intrusion.

ACKNOWLEDGEMENTS

Research for this study was supported by and benefited from numerous discussions with Max Frenzel, Axel Sjöqvist, Johan Berg and Magnus Leijd. Bernhard Schulz assisted with the classification of meta-nepheline syenites and Kai Bachmann performed the high resolution BSE images. The authors are deeply grateful for their support. Furthermore, the authors are indebted to Tasman Metals Ltd. for supporting field work, providing rock samples, geological maps and cross sections. The manuscript was improved by the reviews of Roger Mitchell and Stefano Salvi. Their comments and suggestions are greatly appreciated. The authors thank A. Skelton for the editorial handling.

REFERENCES

Åberg, G., 1988. Middle Proterozoic anorogenic magmatism in Sweden and worldwide. Lithos 21, 279–289.

Åberg, G., Kornfält, K.-A., Nord, A.G., 1985a. Further radiometric dating of the Karlshamn granite, south Sweden. GFF 107, 197–202.

Åberg, G., Kornfält, K.-A., Nord, A.G., 1985b. The Vånga granite, south Sweden-a complex granitic intrusion. GFF 107, 153–159.

Åberg, G., Löfvendahl, R., Levi, B., 1984. The Götemar granite—isotopic and geochemical evidence for a complex history of an anorogenic granite. GFF 106, 327–333.

Adamson, O.J., 1944. The petrology of the Norra Kärr district: An occurrence of alkaline rocks in southern Sweden. GFF 66, 113–255.

Andersen, T., Carr, P., Erambert, M., 2012. Late-magmatic mineral assemblages with siderite and zirconian pyroxene and amphibole in the anorogenic Mt Gibraltar microsyenite, New South Wales, Australia, and their petrological implications. Lithos 151, 46–56.

Andersen, T., Erambert, M., Larsen, A.O., Selbekk, R.S., 2010. Petrology of nepheline syenite pegmatites in the Oslo Rift, Norway: Zirconium silicate mineral assemblages as indicators of alkalinity and volatile fugacity in mildly agpaitic magma. J. Petrol. 51, 2303–2325.

Andersen, T., Friis, H., 2015. The transition from agpaitic to hyperagpaitic magmatic crystallization in the Ilímaussaq alkaline complex, South Greenland. J. Petrol. 56, 1343–1364.

Andersson, U.B., Rutanen, H., Johansson, Å., Mansfeld, J., Rimša, A., 2007. Characterization of the Paleoproterozoic mantle beneath the Fennoscandian Shield: Geochemistry and isotope geology (Nd, Sr) of~ 1.8 Ga mafic plutonic rocks from the Transscandinavian Igneous Belt in southeast Sweden. Int. Geol. Rev. 49, 587–625.

Andréasson, P., Rodhe, A., 1994. Ductile and brittle deformation within the Protogine Zone, southern Sweden: a discussion. GFF 116, 115–117.

Arzamastsev, A.A., Bea, F., Glaznev, V.N., Arzamastseva, L. V, Montero, P., 2001. Kola alkaline province in the Paleozoic: evaluation of primary mantle magma composition and magma generation conditions. Russ. J. Earth Sci. 3, 3–24.

Arzamastsev, A.A., Belyatsky, B. V, Travin, A. V, Arzamastseva, L. V, Tsarev, S.E., 2005. Dike Rocks in the Khibina Massif: Relations with the Plutonic Series, Age, and Characteristics of the Mantle Source. Petrology 13, 267–288.

Atanasova, P., Krause, J., Möckel, R., Osbahr, I., Gutzmer, J., 2015. Electron Probe Microanalysis of REE in Eudialyte Group Minerals: Challenges and Solutions. Microsc. Microanal. 21, 1096–1113.

Berman, R.G., 1988. Internally-consistent thermodynamic data for minerals in the system Na2O-K2O-CaO-MgO-FeO-Fe2O3-Al2O3-SiO2-TiO2-H2O-CO2. J. Petrol. 29, 445–522.

Berman, R.G., Brown, T.H., Perkins, E.H., 1987. GeO-calc–software for calculation and display of P–T–X phase diagrams. Am. Mineral. 72, 861–862.

Bingen, B., Nordgulen, O., Viola, G., 2008. A four-phase model for the Sveconorwegian orogeny, SW Scandinavia. Nor. Geol. Tidsskr. 88, 43.

Bingen, B., Stein, H.J., Bogaerts, M., Bolle, O., Mansfeld, J., 2006. Molybdenite Re–Os dating constrains gravitational collapse of the Sveconorwegian orogen, SW Scandinavia. Lithos 87, 328–346.

Borst, A.M., Friis, H., Andersen, T., Nielsen, T.F.D., Waight, T.E., Smit, M.A., 2016. Zirconosilicates in the kakortokites of the Ilímaussaq complex, South Greenland: Implications for fluid evolution and high-field-strength and rare-earth element mineralization in agpaitic systems. Mineral. Mag. 80, 5–30.

Brander, L., 2011. The Mesoproterozoic Hallandian event-a region-scale orogenic event in the Fennoscandian Shield.

Brander, L., Söderlund, U., 2009. Mesoproterozoic (1.47–1.44 Ga) orogenic magmatism in Fennoscandia; Baddeleyite U–Pb dating of a suite of massif-type anorthosite in S. Sweden. Int. J. Earth Sci. 98, 499–516.

Breemen, O. van, Currie, K.L., 2004. Geology and U Pb geochronology of the Kipawa Syenite Complex a thrust related alkaline pluton and adjacent rocks in the Grenville Province of western Quebec. Can. J. Earth Sci. 41, 431–455.

Chakrabarty, A., Mitchell, R.H., Ren, M., Saha, P.K., Pal, S., Pruseth, K.L., Sen, A.K., 2016a. PREPUBLICATION: Magmatic, hydrothermal and subsolidus evolution of the agpaitic nepheline syenites of the Sushina Hill Complex, India: implications for the metamorphism of peralkaline syenites. Mineral. Mag.

Chakrabarty, A., Mitchell, R.H., Ren, M., Saha, P.K., Pal, S., Pruseth, K.L., Sen, A.K., 2016b. Magmatic, hydrothermal and subsolidus evolution of the agpaitic nepheline syenites of the Sushina Hill Complex, India: implications for the metamorphism of peralkaline syenites. Mineral. Mag. 80, 1161–1193. https://doi.org/10.1180/minmag.2016.080.057

Currie, K.L., Breemen, O. van, 1996. The Origin of Rare Minerals in the Kipawa Syenite Complex Western

Quebec. Can. Mineral. 34, 435–451.

Currie, K.L., Curtis, L.W., 1976. An application of multicomponent solution theory to jadeitic pyroxenes. J. Geol. 179–194.

Curtis, L.W., Currie, K.L., 1981. Geology and petrology of the Red Wine alkaline complex, central Labrador. Geological Survey of Canada.

Curtis, L.W., Gittins, J., 1979. Aluminous and titaniferous clinopyroxenes from regionally metamorphosed agpaitic rocks in central Labrador. J. Petrol. 20, 165–186.

Dostal, J., 2015. Rare Metal Deposits Associated with Alkaline/Peralkaline Igneous Rocks. Rev. Econ. Geol. 18.

Fandrich, R., Gu, Y., Burrows, D., Moeller, K., 2007. Modern SEM-based mineral liberation analysis. Int. J. Miner. Process. 84, 310–320.

Giehl, C., Marks, M., Nowak, M., 2013. Phase relations and liquid lines of descent of an iron-rich peralkaline phonolitic melt: an experimental study. Contrib. to Mineral. Petrol. 165, 283–304.

Giehl, C., Marks, M.A.W., Nowak, M., 2014. An experimental study on the influence of fluorine and chlorine on phase relations in peralkaline phonolitic melts. Contrib. to Mineral. Petrol. 167, 1–21.

Gillespie, M., Styles, M., 1999. BGS rock classification scheme, Volume 1. Classification of igneous rocks.

Goodenough, K.M., Schilling, J., Jonsson, E., Kalvig, P., Charles, N., Tuduri, J., Deady, E.A., Sadeghi, M., Schiellerup, H., Müller, A., Bertrand, G., Arvanitidis, N., Eliopoulos, D.G., Shaw, R.A., Thrane, K., Keulen, N., 2016. Europe's rare earth element resource potential: An overview of REE metallogenetic provinces and their geodynamic setting. Ore Geol. Rev. 72, Part 1, 838–856. https://doi.org/http://dx.doi.org/10.1016/j.oregeorev.2015.09.019

Goswami, B., Basu, S.K., 2013. Metamorphism of Proterozoic agpaitic nepheline syenite gneiss from North Singhbhum Mobile Belt, eastern India. Mineral. Petrol. 107, 517–538.

Green, E., Holland, T., Powell, R., 2007. An order-disorder model for omphacitic pyroxenes in the system jadeite-diopsidehedenbergite-acmite, with applications to eclogitic rocks. Am. Mineral. 92, 1181–1189.

Hamilton, D.L., 1961. Nephelines as crystallization temperature indicators. J. Geol. 321–329.

Högdahl, K., Andersson, U.B., Eklund, O., 2004. The Transscandinavian Igneous Belt (TIB) in Sweden: a review of its character and evolution. Geological survey of Finland.

Holland, T., Powell, R., 2003. Activity–composition relations for phases in petrological calculations: an asymmetric multicomponent formulation. Contrib. to Mineral. Petrol. 145, 492–501.

Karup-Møller, S., Rose-Hansen, J., 2013. New data on eudialyte decomposition minerals from kakortokites and associated pegmatites of the Ilímaussaq complex, South Greenland. Geol. Soc. Denmark. Bull. 61, 47–70.

Karup-Møller, S., Rose-Hansen, J., Sørensen, H., 2010. Eudialyte decomposition minerals with new hitherto undescribed phases from the Ilímaussaq complex, South Greenland. Geol. Soc. Denmark. Bull. 58, 75–88.

Kogarko, L.N., 1990. Ore-forming potential of alkaline magmas. Lithos 26, 167–175.

Kogarko, L.N., 1987. Alkaline rocks of the eastern part of the Baltic Shield (Kola Peninsula). Geol. Soc. London, Spec. Publ. 30, 531–544.

Kogarko, L.N., Lazutkina, L.N., Romanchev, B.P., 1982. Problems of Genesis of Eudialyte Mineralization. Geokhimiya 1415–1432.

Konnerup-Madsen, J., Rose-Hansen, J., 1982. Volatiles associated with alkaline igneous rift activity: fluid inclusions in the Ilímaussaq intrusion and the Gardar granitic complexes (South Greenland). Chem. Geol. 37, 79–93.

Larsen, L.M., Sørensen, H., 1987. The Ilímaussaq intrusion—progressive crystallization and formation of layering in an agpaitic magma. Geol. Soc. London, Spec. Publ. 30, 473–488.

Liebermann, J., Petrakakis, K., 1991. TWEEQU Thermobarometry: Analysis of Uncertainties and Applications to Granulites from Western Alaska and Austria. Can. Mineral. 29, 857–887.

Lindhuber, M.J., Marks, M.A.W., Bons, P.D., Wenzel, T., Markl, G., 2015. Crystal mat-formation as an igneous layering-forming process: Textural and geochemical evidence from the 'lower layered'nepheline syenite sequence of the Ilímaussaq complex, South Greenland. Lithos 224, 295–309.

Markl, G., Baumgartner, L., 2002. pH changes in peralkaline late-magmatic fluids. Contrib. to Mineral. Petrol. 144, 331–346.

Markl, G., Marks, M., Wirth, R., 2001. The influence of T, $aSiO_2$, and fO_2 on exsolution textures in Fe-Mg olivine: An example from augite syenites of the Ilimaussaq Intrusion, South Greenland. Am. Mineral. 86, 36–46.

Marks, M., Markl, G., 2003. Ilímaussaq 'en miniature': closed-system fractionation in an agpaitic dyke rock from the Gardar Province, South Greenland (contribution to the mineralogy of Ilímaussaq no. 117). Mineral. Mag. 67, 893–919.

Marks, M., Vennemann, T.W., Siebel, W., Markl, G., 2003. Quantification of magmatic and hydrothermal processes in a peralkaline syenite–alkali granite complex based on textures, phase equilibria, and stable and radiogenic isotopes. J. Petrol. 44, 1247–1280.

Marks, M.A.W., Hettmann, K., Schilling, J., Frost, B.R., Markl, G., 2011. The mineralogical diversity of alkaline igneous rocks: critical factors for the transition from miaskitic to agpaitic phase assemblages. J. Petrol. 52, 439–455.

Marks, M.A.W., Markl, G., 2015. The Ilímaussaq alkaline complex, South Greenland, in: Layered Intrusions. Springer, pp. 649–691.

McLelland, J.M., 1989. Crustal growth associated with anorogenic, mid-Proterozoic anorthosite massifs in northeastern North America. Tectonophysics 161, 331–341.

Mitchell, R.H., 2015. Primary and secondary niobium mineral deposits associated with carbonatites. Ore Geol. Rev. 64, 626–641.

Mitchell, R.H., Platt, R.G., 1978. Mafic mineralogy of ferroaugite syenite from the Coldwell alkaline complex, Ontario, Canada. J. Petrol. 19, 627–651.

Möller, C., Andersson, J., Lundqvist, I., Hellström, F., 2007. Linking deformation, migmatite formation and zircon U–Pb geochronology in polymetamorphic orthogneisses, Sveconorwegian Province, Sweden. J. Metamorph. Geol. 25, 727–750.

Möller, V., Williams-Jones, A.E., 2016. Petrogenesis of the Nechalacho Layered Suite, Canada: Magmatic Evolution of a REE–Nb-rich Nepheline Syenite Intrusion. J. Petrol. 57, 229–276.

Morimoto, N., Fabries, J., Ferguson, A.K., Ginzburg, I. V, Ross, M., Seifert, F.A., Zussman, J., Aoki, K., Gottardi, G., 1988. Nomenclature of pyroxenes. Am. Mineral. 73, 1123–1133.

Nanda, J., Gupta, S., Dobmeier, C.J., 2008. Metamorphism of the Koraput Alkaline Complex, Eastern Ghats Province, India—evidence for reworking of a granulite terrane. Precambrian Res. 165, 153–168.

Oberti, R., Boiocchi, M., Hawthorne, F.C., Ball, N.A., Harlow, G.E., 2015. Eckermannite revised: The new holotype from the Jade Mine Tract, Myanmar—crystal structure, mineral data, and hints on the reasons for the rarity of eckermannite. Am. Mineral. 100, 909–914.

Pekov, I. V, 1998. Yttrium mineralization in the Khibiny–Lovozero alkaline complex (Kola Peninsula). Zap. VMO 5, 66–85.

Pfaff, K., Krumrei, T., Marks, M., Wenzel, T., Rudolf, T., Markl, G., 2008. Chemical and physical evolution of the ‘lower layered sequence’from the nepheline syenitic Ilímaussaq intrusion, South Greenland: Implications for the origin of magmatic layering in peralkaline felsic liquids. Lithos 106, 280–296.

Pfaff, K., Wenzel, T., Schilling, J., Marks, M.A.W., Markl, G., 2010. A fast and easy-to-use approach to cation site assignment for eudialyte-group minerals. Neues Jahrb. für Mineral. J. Mineral. Geochemistry 187, 69–81.

Piotrowski, J.M., Edgar, A.D., 1970. Melting relations of undersaturated Alkaline rocks from south Greenland compared to those of Africa and Canada. Meddelelser om Grönl. 181, 1–62.

Rankin, L.R., 2011. Structural setting of the Norra Kärr intrusive complex, Central Sweden. Geointerp Confidential Report 2011/14.

Ratschbacher, B.C., Marks, M.A.W., Bons, P.D., Wenzel, T., Markl, G., 2015. Emplacement and geochemical evolution of highly evolved syenites investigated by a combined structural and geochemical field study: The lujavrites of the Ilímaussaq complex, SW Greenland. Lithos 231, 62–76.

Rock, N.M.S., 1990. The International Mineralogical Association (IMA/CNMMN) pyroxene nomenclature scheme: computerization and its consequences. Mineral. Petrol. 43, 99–119.

Salvi, S., Fontan, F., Monchoux, P., Williams-Jones, A.E., Moine, B., 2000. Hydrothermal mobilization of high field strength elements in alkaline igneous systems: evidence from the Tamazeght Complex (Morocco). Econ. Geol. 95, 559–576.

Schilling, Julian, Marks, M.A.W., Wenzel, T., Vennemann, T., Horváth, L., Tarassoff, P., Jacob, D.E., Markl, G., 2011a. The magmatic to hydrothermal evolution of the intrusive mont saint-hilaire complex: Insights into the late-stage evolution of peralkaline rocks. J. Petrol. 52, 2147–2185.

Schilling, Julian, Ronald Frost, B., Marks, M.A.W., Wenzel, T., Markl, G., 2011b. Fe-Ti oxide-silicate (QUIlF-type) equilibria in feldspathoid-bearing systems. Am. Mineral. 96, 100–110.

Schilling, J, Wu, F.-Y., McCammon, C., Wenzel, T., Marks, M.A.W., Pfaff, K., Jacob, D.E., Markl, G., 2011. The compositional variability of eudialyte-group minerals. Mineral. Mag. 75, 87–115.

Sheard, E.R., Williams-Jones, A.E., Heiligmann, M., Pederson, C., Trueman, D.L., 2012. Controls on the Concentration of Zirconium, Niobium, and the Rare Earth Elements in the Thor Lake Rare Metal Deposit, Northwest Territories, Canada. Econ. Geol. 107, 81–104. https://doi.org/10.2113/econgeo.107.1.81

Sjöqvist, A.S.L., 2015. Agpaitic rocks of the Norra Kärr alkaline complex. Earth Sci. University of Gothenburg.

Sjöqvist, A.S.L., Cornell, D.H., Andersen, T., Andersson, U.B., Christensson, U.I., Ranjer, S.J.E., Holtstam, D., Leijd, M., 2014. Geochronology of the Norra Kärr alkaline complex, southern Sweden, in: 31st Nordic Geological Winter Meeting, Lund, Sweden.

Sjöqvist, A.S.L., Cornell, D.H., Andersen, T., Erambert, M., Ek, M., Leijd, M., 2013. Three compositional varieties of rare-earth element ore: eudialyte-group minerals from the Norra Kärr Alkaline Complex, Southern Sweden. Minerals 3, 94–120.

Smellie, J.A.T., Stuckless, J.S., 1985. Element mobility studies of two drill-cores from the Goetemar Granite (Kraakemaala test site), Southeast Sweden. Chem. Geol. 51, 55–78.

Smith, M.P., Moore, K., Kavecsánszki, D., Finch, A.A., Kynicky, J., Wall, F., 2016. From mantle to critical zone: A review of large and giant sized deposits of the rare earth elements. Geosci. Front.

Söderlund, U., Möller, C., Andersson, J., Johansson, L., Whitehouse, M., 2002. Zircon geochronology in polymetamorphic gneisses in the Sveconorwegian orogen, SW Sweden: ion microprobe evidence for 1.46–1.42 and 0.98–0.96 Ga reworking. Precambrian Res. 113, 193–225.

Söderlund, U., Patchett, P.J., Vervoort, J.D., Isachsen, C.E., 2004. The 176 Lu decay constant determined by Lu–Hf and U–Pb isotope systematics of Precambrian mafic intrusions. Earth Planet. Sci. Lett. 219, 311–324.

Sood, M.K., Edgar, A.D., 1970. Melting Relations of Undersaturated Alkaline Rocks from the Ilímaussaq Intrusion and Grønnedal-Íka Complex, South Greenland. Meddelelser om Grönl. 181, 41.

Sørensen, H., 1997. The agpaitic rocks; an overview. Mineral. Mag. 61, 485–498.

Sørensen, H., 1960. On the agpaitic rocks. Grønlands geologiske undersøgelse.

Sørensen, H., Bohse, H., Bailey, J.C., 2006. The origin and mode of emplacement of lujavrites in the Ilímaussaq alkaline complex, South Greenland. Lithos 91, 286–300. https://doi.org/10.1016/j.lithos.2006.03.021

Tilley, C.E., 1954. Nepheline-alkali feldspar parageneses. Am. J. Sci. 252, 65–75.

Törnebohm, A.E., 1906. Katapleiite-syenit, en nyupptäckt varietet af nefelinsyenit i Sverige. SGU Ser. C 1–54.

Upton, B.G.J., 2013. Tectono-magmatic evolution of the younger Gardar southern rift, South Greenland. Geol. Surv. Denmark Greenl. Bull.

Ussing, N.V., 1912. Geology of the country around Julianehaab, Greenland. I commission hos CA Reitzel.

von Eckermann, H., 1968. New contributions to the interpretation of the genesis of the Norra Kärr alkaline body in Southern Sweden. Lithos 1, 76–88.

Wahlgren, C.-H., Cruden, A.R., Stephens, M.B., 1994. Kinematics of a major fan-like structure in the eastern part of the Sveconorwegian orogen, Baltic Shield, south-central Sweden. Precambrian Res. 70, 67–91.

Woolley, A.R., Platt, R.G., Eby, G.N., 1996. Relatively Aluminous Alkali Pyroxene in Nepheline Syenite from Malawi. Can. Mineral. 34, 423–434.

Appendix C

This is a pre-print, author-produced version of an article submitted for publication in Lithos. This article is not yet accepted for publication.

Fractionation of geochemical twins (Zr/Hf, Nb/Ta and Y/Ho) and HREE-enrichment during magmatic and metamorphic processes in peralkaline nepheline syenites from Norra Kärr (Sweden).

Petya Atanasova[1, 2], Michael A.W. Marks[2], Max Frenzel[1], Jens Gutzmer[1], Joachim Krause[1], Gregor Markl[2]

[1]Helmholtz-Zentrum Dresden - Rossendorf, Helmholtz Institute Freiberg for Resource Technology, 09599 Freiberg, Saxony, Germany

[2]Universität Tübingen, Fachbereich Geowissenschaften, 72074 Tübingen, Germany

Keywords: fractionation, geochemical twins, rare earth elements, clinopyroxene, eudialyte-group minerals, nepheline syenite

Abstract

The Norra Kärr complex (Sweden) consists of deformed and metamorphosed peralkaline nepheline syenites that contain eudialyte-group minerals as the major host of high field strength elements and rare earth elements. Petrographic studies have revealed the presence of paragenetically distinct generations of eudialyte-group minerals and clinopyroxene of magmatic and metamorphic origin. In this study, we present the trace element characteristics of these different generations of rock-forming minerals in the three major lithological subunits of the Norra Kärr complex.

The trace element chemistry of eudialyte-group minerals mimic whole-rock compositions and display well-developed negative Eu-anomalies and strong Sr- and Ba-depletions in chondrite-normalized diagrams. They imply that the Norra Kärr rocks developed by intense fractional crystallization from an alkali basaltic parental magma. Our data also illustrate that eudialyte-group minerals do not significantly fractionate the geochemical twins Zr/Hf, Y/Ho and Nb/Ta during magmatic processes. In contrast, magmatic clinopyroxene shows a clear preference for Hf over Zr.

The transition from magmatic to metamorphic crystallization is clearly marked in the trace element chemistry of clinopyroxene by decreasing Zr/Hf and Y/Ho ratios. This accompanies the change in major element composition from aegirine *sensu strictu* to Al-aegirine. The transition from a magmatic to a metamorphic environment is also recorded by an increase of the rare earth element content of eudialyte-group minerals, especially the heavy rare earth elements. The exceptional enrichment of heavy rare earth elements in late metamorphic eudialyte may result from residual enrichment, whereby light rare earth elements were preferentially mobilized to form local secondary light rare earth-rich rinkite-group mineral assemblages.

Introduction

Peralkaline (molar (Na + K)/Al) ratio > 1) nepheline syenites generally consist of minerals such as alkali feldspar, feldspathoids, sodic amphibole/clinopyroxene and in some cases eudialyte-group minerals (EGM) (Marks and Markl, 2017). They are also typically enriched in high field strength elements (HFSE) and form one of the most promising resources for future REE supply (e.g. Goodenough et al., 2016; Mitchell, 2015; Smith et al., 2016). Within this context, the mineral chemistry of the EGM is of particular interest because they are often regarded as the primary host of HFSE. Yet,

this complex group of minerals is also well known to contain variable amounts of Zr, Nb, REE and Y (e.g., Johnsen et al., 2003; Pfaff et al., 2010; Rastsvetaeva, 2007; Schilling et al., 2011).

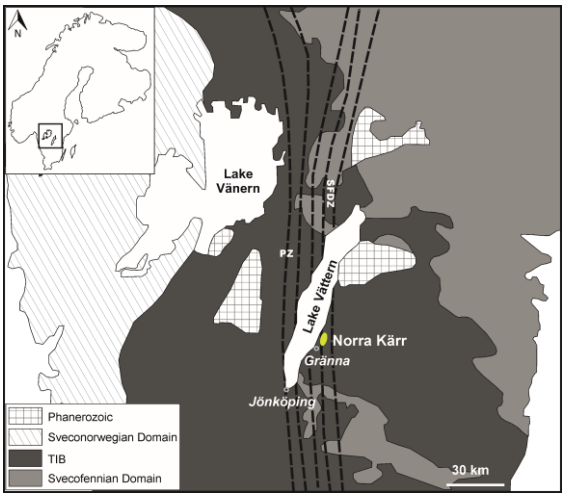

Fig.1. Simplified regional geological map illustrating major lithological units (modified after Söderlund et al., 2002; Wahlgren et al., 1994). Yellow ellipse resembles the Norra Kärr complex. Dashed lines – major tectonic lineaments; PZ - Protogine Zone, SFDZ - Sveconorwegian Frontal Deformation Zone.

The formation of EGM in the peralkaline melts is favored by low fO_2 conditions and low H_2O activities (Marks and Markl, 2017 and references therein). Importantly, EGM inherit characteristics from their parental melts (or fluids), which in turn are controlled by source characteristics and fractionation of previously crystallizing phases (e.g., Schilling et al., 2011). In addition, crystal chemical effects likely contribute to trace-element incorporation into EGM. Magmatic EGM are easily altered; metamorphic and hydrothermal overprints result in complex REE-redistribution processes and the formation of separate REE-, Zr- and Nb- minerals (e.g., Borst et al., 2016; Karup-Møller et al., 2010; Karup-Møller and Rose-Hansen, 2013; Möller and Williams-Jones, 2017; Salvi et al., 2000). Based on studies comparing whole-rock and eudialyte compositions, REE are moderately compatible in EGM. To date, there is no conclusive evidence that EGM strongly fractionate the HFSE and the REE from each other (e.g.,Marks et al., 2008; Möller and Williams-Jones, 2016; Pfaff et al., 2008; Julian Schilling et al., 2011).

Sodic clinopyoxene (cpx, aegirine-augite to aegirine) is often intimately associated with EGM in peralkaline nepheline syenites (REF). Based on field studies and experimental data, however, sodic clinopyroxene does not show strong affinity for the REE (e.g.,Beard, 2018; Marks et al., 2004), though they may incorporate significant amounts of trace elements, including REE and HFSE. As key fractionating minerals in alkaline magmatic systems, cpx are relevant for the interpretation of magmatic processes (e.g. Kogarko, 2015; Marks et al., 2004; Möller and Williams-Jones, 2016; Wood and Blundy, 1997). However, the influence of cpx on the formation of REE and HFSE mineralization in peralkaline systems is not well understood. Although systematic

changes in major element composition of cpx are obvious in post-magmatic alteration, little is known about trace element behavior during such overprints.

The EGM-bearing nepheline syenites of the Norra Kärr alkaline complex in Sweden (Fig. 1) have been extensively studied, as they are known to host very high concentrations especially of heavy REE (HREE) (Atanasova et al., 2017; Sjöqvist, 2015; Sjöqvist et al., 2014, 2013). The complex is an excellent case study to distinguish the effects of magmatic and hydrothermal processes in nepheline syenites (e.g.,Schilling et al., 2011; Sjöqvist et al., 2013) and to build a model for local HREE enrichment under magmatic and metamorphic conditions. Trace elements signatures of EGM and cpx are used to infer source characteristics of the mantle source for alkaline magmatism as well as to distinguish between HFSE and REE partitioning under magmatic and metamorphic conditions.

Samples and methods

Trace element compositions for eudialyte and clinopyroxene were acquired by Laser Ablation inductively coupled Plasma Mass Spectrometry (LA-ICP-MS) with a 193 nm Photon Machines Analyte G2 excimer laser ablation system coupled to a Thermo Finnegan Element 2 sector field ICP-MS at the Institute for Mineralogy of the Westfälische Wilhelms-Universität Münster, Germany. A frequency of 10 Hz, a fluence of 4 J/cm^2 and a spot size of 40 µm were chosen for analysis. Helium was used as carrier gas. The ablated material was analyzed in the ICP-MS in low-resolution mode with a dwell time of 20 s for the gas blank and 50 s on the sample. The wash-out period between two analyses was 20 s.

Table 1: List of samples and minerals analyzed

Sample	Drill core	Position	Subunit	Mineral analyzed
5408	NKA 11054 P7	42.44-42.71m	Mid	cpx, EGM
5611	NKA 11056 J1	110.20-110.34m	Outer	cpx, EGM
5612	NKA 11056 J1	119.60-119.90m	Mid	cpx, EGM
5613	NKA 11056 J1	126.00-126.25m	Mid	cpx, EGM
5618	NKA 11056 J1	198.60-198.86m	Mid	cpx, EGM
5631	NKA 11056 J1	350.20-350.40m	Outer	cpx
6105	NKA 12061 J7	29.85-30.02m	Inner	cpx
6108	NKA 12061 J7	43.44-43.55m	Inner	cpx
6115	NKA 12061 J7	83.36-83.59m	Inner	cpx, EGM
6123	NKA 12061 J7	163.61-163.80m	Outer	cpx, EGM
6124-1	NKA 12061 J7	182.30-182.56m	Outer	cpx
7308	NKA 12073 P5	52.81-52.97m	Mid	cpx, EGM
7315	NKA 12073 P5	91.50-91.61m	Mid	cpx, EGM

cpx = clinopyroxene; EGM = Eudialyte-group minerals.

NIST SRM 612 was used for the calibration of the instrument, as reference material for the quantification of the measured intensities and to monitor instrumental drift. BIR-1G was measured as an unknown to assess the quality of the analysis (see electronic supplement A). Data reduction was performed using a programmed Microsoft Excel spreadsheet. Silicon concentrations determined by EPMA (Atanasova et al., 2017, 2015) are applied

as internal standard. Blank-corrected count rates were calculated relative to the internal standard (29Si) in order to compensate for the intensity decrease during ablation. Obvious outliers were subsequently rejected from the dataset subequently elemental concentrations calculated using drift corrected relative sensitivity factors derived from the analyses of NIST SRM 612 (see electronic supplement A). Further details of the analytical procedure are given in Jochum et al. (2007, 2006). The detection limits where between 0.2 µg/g to 2.0 µg/g for REE, and 10 µg/g for Y. All limits of detection for cpx and limits of quantitation for EGM are listed in electronic supplement B.

The investigated samples (Table 1; Fig. 2) represent a subset of the material used in Atanasova et al. (2017). They derive from four diamond drill cores (NKA 11054, 11056, 12061 and 12073) and include three samples from the inner subunit, six samples from the mid subunit and four samples from the outer subunit (Fig. 2).

Averaged whole-rock geochemical data of 8,100 drill core samples from the outer, mid and inner subunits were kindly provided by Leading Edge Materials (formerly Tasman Metals Ltd.). The data is summarized in Table 2 and mainly used to calculate the ratios Zr/Hf, Y/Ho, Nb/Ta and La/Lu of the three subunits for comparison.

Table 2: Average whole-rock geochemical data for main and trace elements of the three major subunits of the Norra Kärr alkaline complex

	Outer subunit	Mid subunit	Inner subunit
wt.%	n=82	n=87	n=22
SiO_2	56.17	55.59	56.80
TiO_2	0.06	0.07	0.11
ZrO_2	1.44	2.01	1.48
Al_2O_3	18.07	16.49	17.17
Fe_2O_3	5.04	6.41	5.26
MnO	0.12	0.23	0.40
MgO	0.14	0.22	0.30
CaO	1.28	1.30	1.60
Na_2O	11.01	10.84	10.18
K_2O	3.65	3.64	3.80
Cl	0.01	0.02	0.01
S*	0.002	0.005	0.008
mg/g	n=3086	n=3891	n=1123
La_2O_3	218.51	547.01	688.12
Ce_2O_3	484.00	1252.17	1400.20
Pr_2O_3	64.35	165.32	167.33
Nd_2O_3	263.00	675.49	610.46
Sm_2O_3	78.94	190.83	138.21
Eu_2O_3	10.46	23.28	16.01
Gd_2O_3	96.98	211.86	141.64
Tb_2O_3	21.60	42.98	27.51
Dy_2O_3	156.96	290.46	185.31
Ho_2O_3	37.28	64.45	41.44
Er_2O_3	121.60	197.39	129.66
Tm_2O_3	19.52	30.18	20.20
Yb_2O_3	123.22	184.71	126.03
Lu_2O_3	17.54	25.29	17.50
Y_2O_3	1138.15	2317.22	1525.98
Ba	97.94	89.85	110.51
Cs	4.30	6.85	28.51
Co*	0.30	0.40	0.90
Cr	48.00	35.10	36.10
Ga	80.46	91.27	102.52
Hf	257.03	313.58	241.89
Nb	200.88	455.75	288.34
Ni*	3.40	3.00	3.10
P*	130.26	25.63	32.06
Pb	75.96	436.01	350.08
Rb	272.36	298.10	437.29
Sn	57.19	112.92	122.38
Sr	68.29	120.99	156.23
Ta	20.20	28.93	19.34
Th	5.18	5.57	11.00
U	6.21	12.08	20.70
V*	4.14	3.83	4.73
W	3.25	4.18	3.32
Zn	104.71	89.50	136.10
ppb			
Be*	5836.00	8065.83	25153.29
Bi*	385.80	356.71	539.15
Ge*	564.31	2095.68	1858.09
Li*	60029.89	112901.05	118016.12
Sb*	51.82	115.93	96.01
Sc*	6700.00	9849.77	6641.66
Zr/Hf	41.54	47.53	45.40
Y/Ho	27.54	32.43	33.22
Nb/Ta	9.94	15.75	14.91
La/Lu	1.25	2.17	3.95

* less Nr of analyses

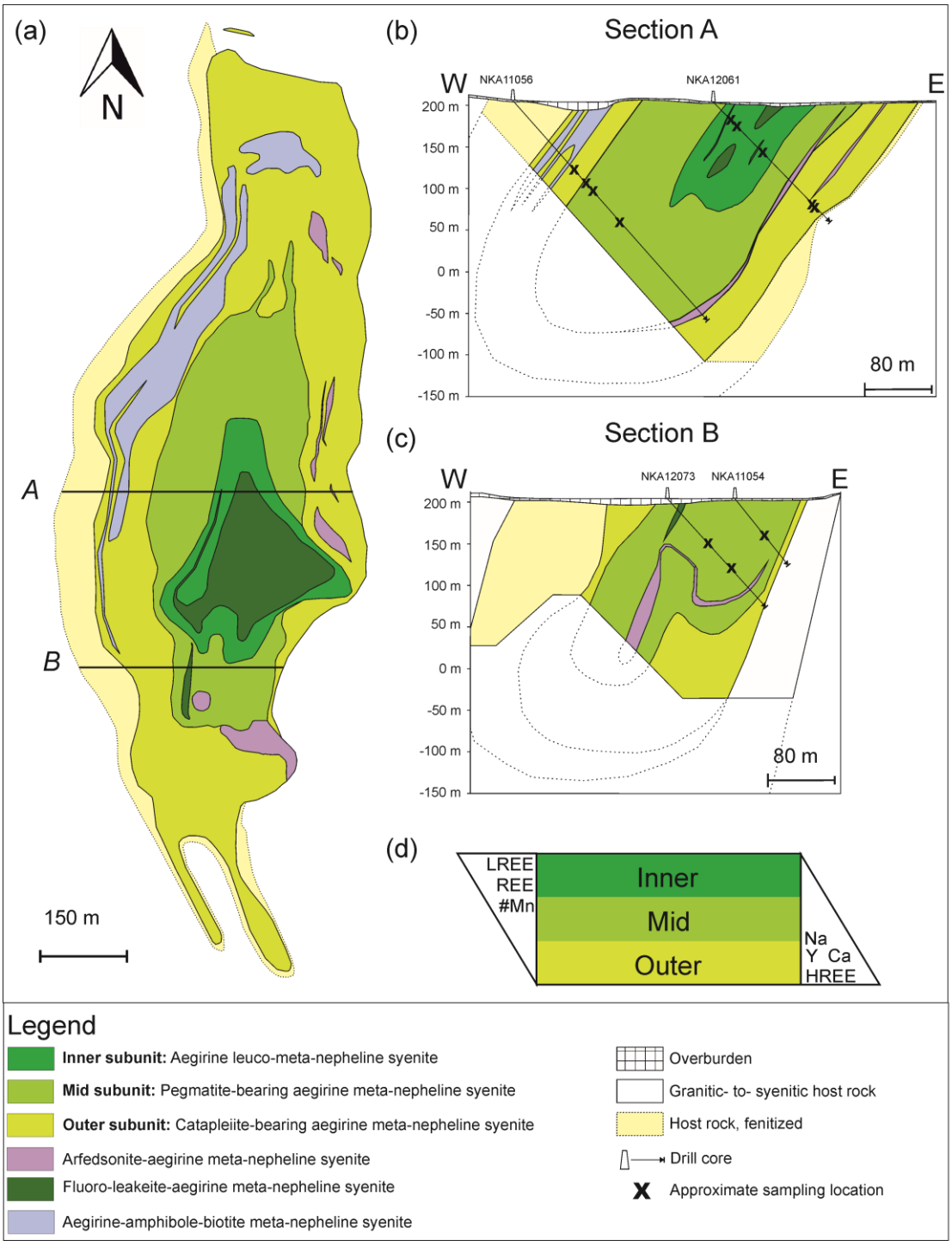

Fig.2. (a) Simplified geological map of the Norra Kärr complex illustrating major lithological units (modified after Tasman Metals Ltd). The deformation is well visualized in W-E cross sections (b) J and (c) P. Approximate sampling location of samples used for this study as listed in Table 1 are indicated. d) Considered primary magmatic layering of the intrusion with preserved major and trace element enrichment and depletion (#Mn = Mn/(Mn+Fe)).

Geological setting and description

The 1.49±0.01 Ga Norra Kärr complex (Sjöqvist et al., 2014) is located in the Växjö Granite Suite between the Vimmerby Batholith in the east and the major Protogine shear zone (PZ) in the west of the Trans-Scandinavian Igneous Belt (TIB) (Fig. 1). The TIB represents a series of 1.85 and 1.75 Ga old intrusions in the Svecofennian domain of Fennoscandia that record the reworking of juvenile continental crust (Andersson et al., 2007 and references therein). The magmatic emplacement of Norra Kärr is attributed to either anorogenic or orogenic extension. It can be correlated to the pre-collisional stage of the Danopolonian or Hallandian orogeny in the area east and south-east of Lake Vättern, where A- and I-type granitoids and syenitoids were emplaced in a typical volcanic arc setting (Brander, 2011; Brander and Söderlund, 2009). Åberg (1988) links the emplacement of alkali-calcic and calc-alkaline intrusions into the southernmost parts of the TIB to continental rifting. These rocks are preserved within a westward-dipping (c. 40°) synform (Fig. 2), deformed by moderate east–west- and subsequent weak north–south-directed compression under ductile conditions (Rankin, 2011). The age of deformation accompanied by moderate to high greenschist-facies metamorphism (e.g., Wahlgren and Stephens, 2004) during the Sveconorwegian orogeny has been constrained to 1148±5 Ma (Sjöqvist et al., 2014).

The most common rock types of the Norra Kärr complex (about 85 vol. % of the exposed area) are varieties of catapleiite- and EGM-bearing aegirine meta-nepheline syenites (Fig. 2). The central part (inner subunit) is strongly foliated and is best described as an aegirine leuco-meta-nepheline syenite. A zone of aegirine meta-nepheline syenite rich in pegmatoidal schlieren (mid-subunit) surrounds the inner subunit and is, in turn, surrounded by an outer subunit of foliated catapleiite-bearing aegirine meta-nepheline syenites. The most common deformation features in all rock types include the alignment and stretching of certain minerals and the presence of porphyroclasts, which have tails of recrystallized material (sigma- and delta-clast structures).

Texturally different EGM varieties have been distinguished by Atanasova et al. (2017), which we group here into *magmatic* EGM (sector- and oscillatory-zoned), *metamorphic* EGM (irregular replacement areas) and *late metamorphic* EGM (EGM rims). In the studied samples of the inner subunit, a magmatic record of EGM is missing.On the deposit scale, magmatic EGM show a continuous decrease in Y (from 0.8 to 0.3 apfu) and HREE (from 0.15

Table 3: Average compositions of the various types of eudialyte-group minerals (EGM) of the Norra Kärr complex

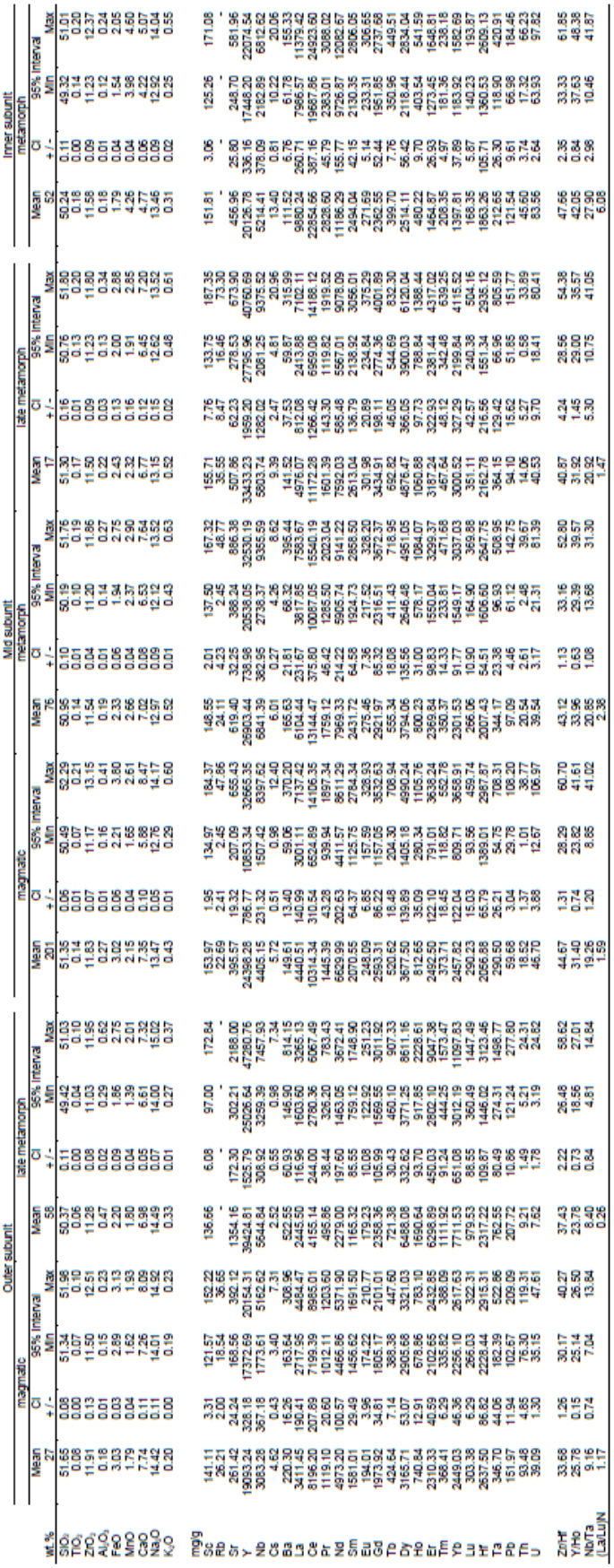

Table 4: Average compositions of the various clinopyroxene (cpx) types of the Norra Kärr complex

	Outer								Mid								Inner							
	magmatic				metamorph				early magmatic				magmatic				magmatic				metamorph			
	Mean	CI	95% interval		Mean	CI	95% interval		Mean	CI	95% interval		Mean	CI	95% interval		Mean	CI	95% interval		Mean	CI	95% interval	
mpig	111	+/-	Min	Max	90	+/-	Min	Max	16	+/-	Min	Max	362	+/-	Min	Max	90	+/-	Min	Max	123	+/-	Min	Max	26	+/-	Min	Max
Li	35.79	4.21	21.87	68.73	43.98	2.40	27.18	56.66	22.11	4.99	16.24	44.70	25.52	0.84	16.38	40.24	54.09	3.31	24.72	80.48	249.70	201.0	15.05	5410.2	22.13	1.53	15.68	29.11
Be	-	-	0.26	1.77	-	-	0.99	0.99	2.79	0.34	1.84	3.98	1.75	0.24	0.55	3.36	6.36	1.54	1.41	11.30	-	-	0.34	3.50	-	-	0.70	9.51
B	-	-	-	-	-	-	-	-	-	-	-	-	-	-	-	-	-	-	-	-	-	-	-	-	-	-	-	-
Sc	-	-	4.52	9.15	-	-	-	-	31.92	2.47	23.27	37.55	12.41	0.72	6.55	25.38	1334.8	111.5	6.22	6.22	2620.4	137.7	7.72	18.72	2322.8	265.0	1416.6	3472.6
Ti	943.45	33.17	613.5	1328.9	500.9	41.2	222.1	948.3	3119.81	83.81	2891.36	3386.95	3446.5	223.9	1382.2	10345.3	1	6	758.2	2487.0	1	0	1125.2	4362.4	4	3	3	9
V	14.07	1.22	5.27	22.43	7.98	1.75	1.62	28.63	8.23	0.16	7.76	8.96	6	1	0	19.93	2.61	0.58	0.35	13.04	10.28	1.55	1.43	29.99	7.66	1.59	2.35	14.34
Cr	-	-	-	-	-	-	-	-	-	-	-	-	-	-	-	-	-	-	-	-	-	-	-	-	-	-	-	-
Rb	-	-	0.09	9.22	-	-	0.33	8.28	-	-	-	2.16	-	-	0.13	37.82	-	-	0.33	11.74	-	-	0.17	19.68	-	-	0.29	13.52
Sr	0.68	0.06	0.35	1.41	0.52	0.05	0.29	1.09	0.72	0.33	0.28	2.16	3.31	1.75	0.44	5.90	-	-	0.35	2.04	1.12	0.19	0.35	2.37	0.76	0.25	0.28	2.09
Y	2.22	0.27	0.45	5.32	1.20	0.10	0.46	2.30	4.36	0.36	3.25	5.37	43.83	63.31	1.36	33.09	1.36	0.16	0.52	3.22	1.27	0.21	0.11	4.69	0.76	0.29	0.14	2.50
		183.3	419.3	3706.7	325.7	39.9	160.5	760.4	18.50	2.73	10.51	29.07	2966.1	290.5	1.36	243323	20454.2	1692.3	306.2	2049.8	1074.4	137.7	147.8	3464.7	147.8	147.8	147.8	1497.4
Zr	1629.20	8	6	0	1	9	4	5	6	1	0	0	3	9	558.53	8246.05	757.86	92.72	6	5	6	4	170.97	6	613.45	5	247.70	3
Nb	-	-	-	-	-	-	-	-	1.09	0.70	0.15	4.31	13.18	13.30	0.09	35.03	0.80	0.33	0.09	4.18	5.67	6.14	0.08	14.89	1.66	1.33	0.09	10.56
Cs	0.12	0.02	0.09	2.74	0.39	0.14	0.09	2.76	0.86	0.58	0.10	3.41	-	-	0.06	10.11	-	-	0.12	0.47	0.13	0.03	0.10	0.30	-	-	0.10	1.05
Ba	-	-	0.10	0.35	-	-	0.11	0.25	-	-	-	-	-	-	-	-	-	-	-	-	-	-	-	-	-	-	-	-
La	0.52	0.07	0.13	1.35	0.31	0.10	0.05	2.03	4.11	0.65	2.52	6.40	10.55	10.78	0.48	17.54	0.51	0.11	0.08	2.14	1.45	0.45	0.13	10.07	1.13	0.82	0.11	7.25
Ce	1.82	0.22	0.27	4.85	0.81	0.21	0.24	4.19	13.76	1.46	8.98	17.41	28.51	27.75	2.07	36.22	1.56	0.24	0.45	4.10	3.12	0.71	0.46	14.11	2.00	1.15	0.30	9.78
Pr	0.36	0.05	0.05	0.96	0.12	0.03	0.05	0.50	2.56	0.25	1.78	3.29	3.93	3.66	0.35	3.74	0.27	0.04	0.05	0.75	0.39	0.07	0.05	1.34	0.24	0.10	0.05	0.95
Nd	1.63	0.23	0.28	4.61	0.56	0.09	0.28	1.99	11.93	1.21	8.20	15.02	4.38	0.69	1.99	8.78	1.41	0.20	0.33	3.64	1.51	0.31	0.28	3.81	0.88	0.26	0.28	2.34
Sm	0.47	0.05	0.18	1.23	-	-	-	-	2.61	0.36	1.52	3.65	4.20	4.99	0.30	2.42	-	-	0.30	0.76	-	-	0.26	1.33	-	-	0.30	0.38
Eu	-	-	0.04	0.15	-	-	-	-	0.22	0.05	0.09	0.37	-	-	0.07	1.12	-	-	-	-	-	-	0.07	0.17	-	-	-	-
Gd	-	-	0.02	1.08	-	-	-	-	1.75	0.29	1.07	2.63	4.86	6.60	0.33	1.80	-	-	0.31	0.77	-	-	0.21	1.20	-	-	0.22	0.22
Tb	-	-	0.02	0.17	-	-	-	-	0.27	0.04	0.15	0.36	0.88	1.20	0.05	0.36	-	-	0.05	0.13	-	-	0.03	0.22	-	-	0.06	0.06
Dy	0.35	0.05	0.11	1.02	-	-	0.20	0.41	1.77	0.34	0.55	2.88	5.85	8.15	0.20	2.70	-	-	0.20	0.57	-	-	0.11	1.32	-	-	0.19	0.28
Ho	0.09	0.01	0.03	0.24	-	-	0.04	0.10	0.53	0.06	0.33	0.70	1.28	1.78	0.05	0.64	-	-	0.05	0.21	-	-	0.03	0.17	-	-	-	-
Er	0.53	0.07	0.15	1.32	0.31	0.04	0.15	0.73	3.15	0.37	1.85	3.96	4.03	5.30	0.15	2.77	-	-	0.15	0.57	0.23	0.04	0.12	0.74	-	-	0.15	0.31
Tm	0.19	0.02	0.05	0.41	0.14	0.02	0.05	0.28	1.04	0.13	0.66	1.36	0.69	0.76	0.05	0.67	-	-	0.05	0.21	0.08	0.01	0.04	0.19	-	-	0.05	0.09
Yb	2.98	0.30	0.60	6.16	2.80	0.31	0.52	5.82	15.53	1.34	11.60	19.15	6.45	5.07	1.21	7.75	1.87	0.13	0.75	3.03	1.03	0.17	0.25	3.29	0.73	0.17	0.32	1.64
Lu	0.84	0.08	0.24	1.66	0.95	0.11	0.19	1.86	3.57	0.31	2.43	4.35	1.28	0.64	0.39	1.80	0.56	0.04	0.24	0.89	0.29	0.04	0.09	0.94	0.20	0.04	0.08	0.42
Hf	73.23	8.78	17.72	163.86	17.01	2.42	7.99	43.79	770.22	47.97	619.81	891.50	110.28	9.45	22.91	329.73	31.73	3.16	12.73	68.86	37.77	5.40	4.51	121.87	23.17	5.48	8.62	57.62
Ta	-	-	0.04	0.26	-	-	0.04	0.04	0.16	0.03	0.07	0.26	0.04	-	0.04	8.17	-	-	0.04	0.10	-	-	0.04	1.32	-	-	0.04	0.55
Pb	0.23	0.20	0.02	1.47	-	-	0.05	0.77	-	-	0.06	0.41	0.64	0.29	0.05	3.00	-	-	0.06	0.91	1.48	0.69	0.06	7.41	1.46	0.94	0.04	8.13
Th	0.11	0.03	0.02	0.47	-	-	0.03	0.43	0.25	-	0.03	0.90	-	-	0.03	1.32	-	-	0.03	0.13	0.19	0.04	0.02	0.65	0.12	0.06	0.03	0.52
U	-	-	0.02	0.36	-	-	0.02	0.06	0.13	0.08	0.02	0.43	-	-	0.02	6.55	-	-	0.02	0.18	-	-	0.02	1.00	-	-	0.02	1.73
Zr/Hf	22.94	0.56	17.60	27.90	19.99	0.64	13.32	25.93	26.48	1.04	22.41	29.09	27.97	0.60	15.76	36.15	23.59	0.79	18.36	32.58	29.27	0.69	21.93	36.51	26.51	1.42	20.07	31.74
Y/Ho	24.74	1.68	8.93	41.72	21.59	1.30	9.28	32.27	35.29	4.31	23.67	50.05	40.52	3.89	16.03	80.11	23.81	2.43	9.20	54.45	20.56	2.39	2.22	51.87	14.01	5.79	1.54	49.46
Norra	6.97				9.37				6.42				33.03				14.83				19.00				10.52			

to 0.05 apfu) with increasing ΣREE (from 0.4 to 0.8 apfu) and LREE (from 0.3 to 0.7 apfu) from the outer to the mid subunit (Fig. 2 and Atanasova et al., 2017). These changes are attributed to magmatic differentiation processes forming magmatic layering, now preserved in the fold structure that defines the Norra Kärr deposit. The clinopyroxene in these samples is aegirine ($Jd_{2–40}Ae_{45–98}Q_{0–18}$); an early magmatic Zr-aegirine that crystallized before EGM can be distinguished from late magmatic aegirine that co-crystallized with EGM, and metamorphic Al-aegirine that formed due to recrystallization during deformation. Detailed descriptions of all samples and textural varieties of EGM and cpx are available in Atanasova et al. (2017).

Rock-forming alkali feldspar and nepheline are assumed to contain negligible amounts of HFSE only and are therefore not considered further in this study. Noteworthy are secondary REE minerals, spatially associated with EGM. However, due to their very limited grain size (< 10µm) and low abundance (< 0.25 wt.% in average) in most parts of the deposit (Atanasova et al., 2017), their role for the overall REE budget is considered negligible and will not be discussed further here.

Results

More than 830 spot analyses in 60 aegirine grains and more than 320 spot analyses in 55 EGM grains were evaluated for this study. The data are compiled in electronic supplement B. An overview of the data set is presented in terms of averages for all subunits and genetic varieties of EGM and cpx in Tables 3 and 4, respectively. All REE and trace element patterns are shown normalized to the primitive mantle values of Palme and O'Neill (2014). The rare earth elements (REE) are divided according to their atomic weight into 1) light rare earth elements (LREE), i.e. La through to Nd, 2) Middle rare earth elements (MREE), Sm through to Dy and 3) heavy rare earth elements (HREE), Ho through to Lu (Jaireth et al., 2014). Yttrium is grouped with the HREE due to chemical similarity(Bgs, 2011).

Eudialyte-group minerals

Primitive mantle-normalized trace element patterns for EGM reveal enrichment of all LILE without significant differences between the three subunits or the various EGM types (Fig. 3). In all three subunits, Cs and Pb scatter between enrichment factors of 100 to 1,000 and are highly enriched compared to the primitive mantle, while Rb, Sr, Ba and Sc are only moderately enriched with factors between 10 and 100. Amongst

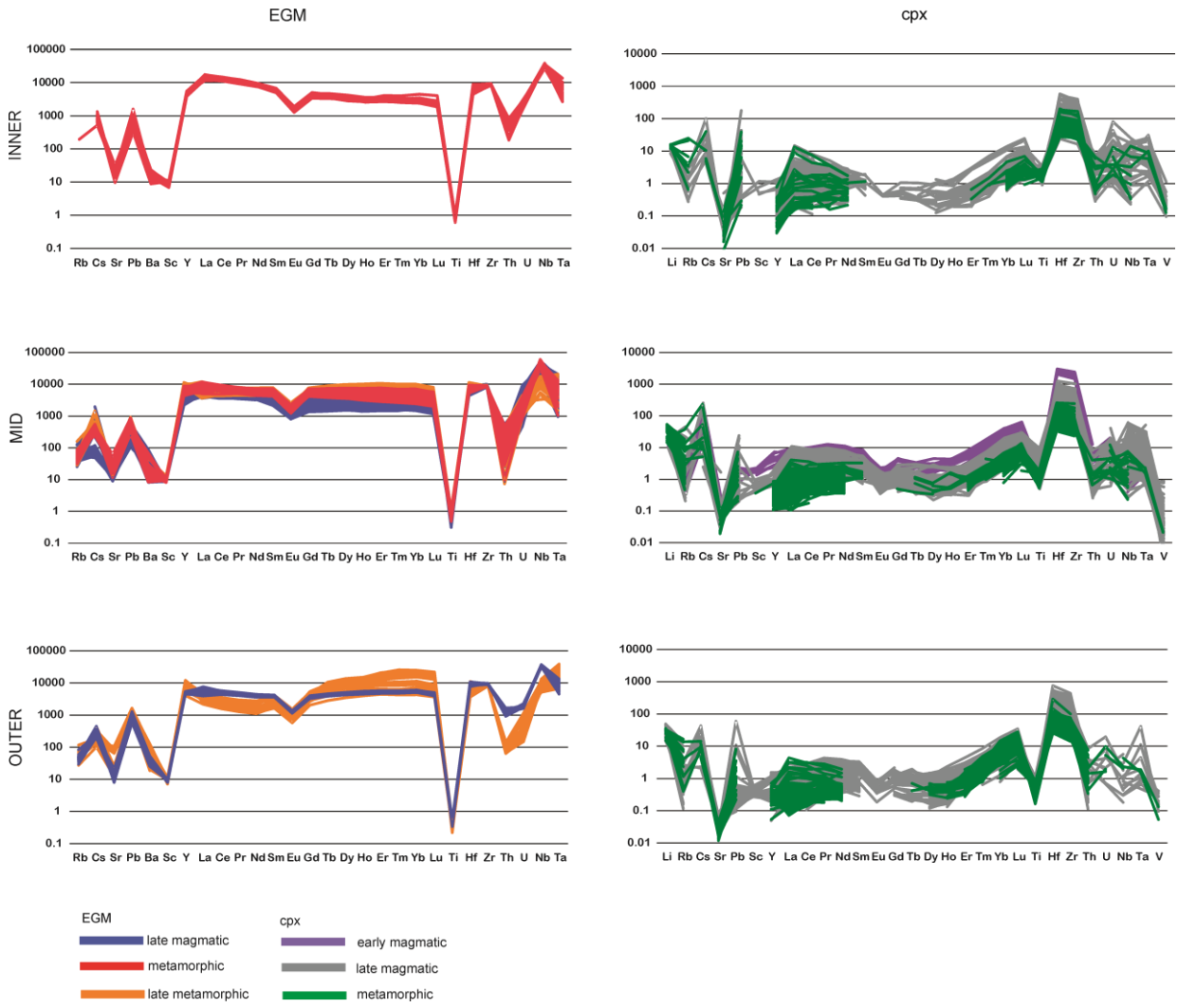

Fig. 3. Primitive mantle-normalized trace elements patterns for sodic clinopyroxenes (cpx) and eudyalite-group minerals (EGM). Normalizing values are after Palme and O'Neill (2014).

the HFSE, Zr, Hf, Ta and Nb are highly enriched, if compared to the primitive mantle, with enrichment factors >1,000 for Zr, Hf, and Ta. The enrichment factor for Nb even exceeds 10,000. The enrichment of U and Th scatters widely, with enrichment factors between 10 and 1,000. Ti is the only HFSE that is depleted – with remarkable consistency (Fig. 3). Again, no large differences between the three subunits as well as between different paragenetic generations are noted (Fig. 3).

EGM REE patterns show high and rather consistent enrichment compared to primitive mantle with enrichment factors varying between about 1,000 and 10,000 (Fig. 4). Total REE concentrations decrease from the inner towards the outer subunit; this is accompanied by relative LREE (La-Dy) depletion and HREE (Ho-Lu) enrichment from the inner to the outer subunit, especially for late metamorphic EGM (Fig. 4), causing the distinct impression that the pattern "tilts" in a very

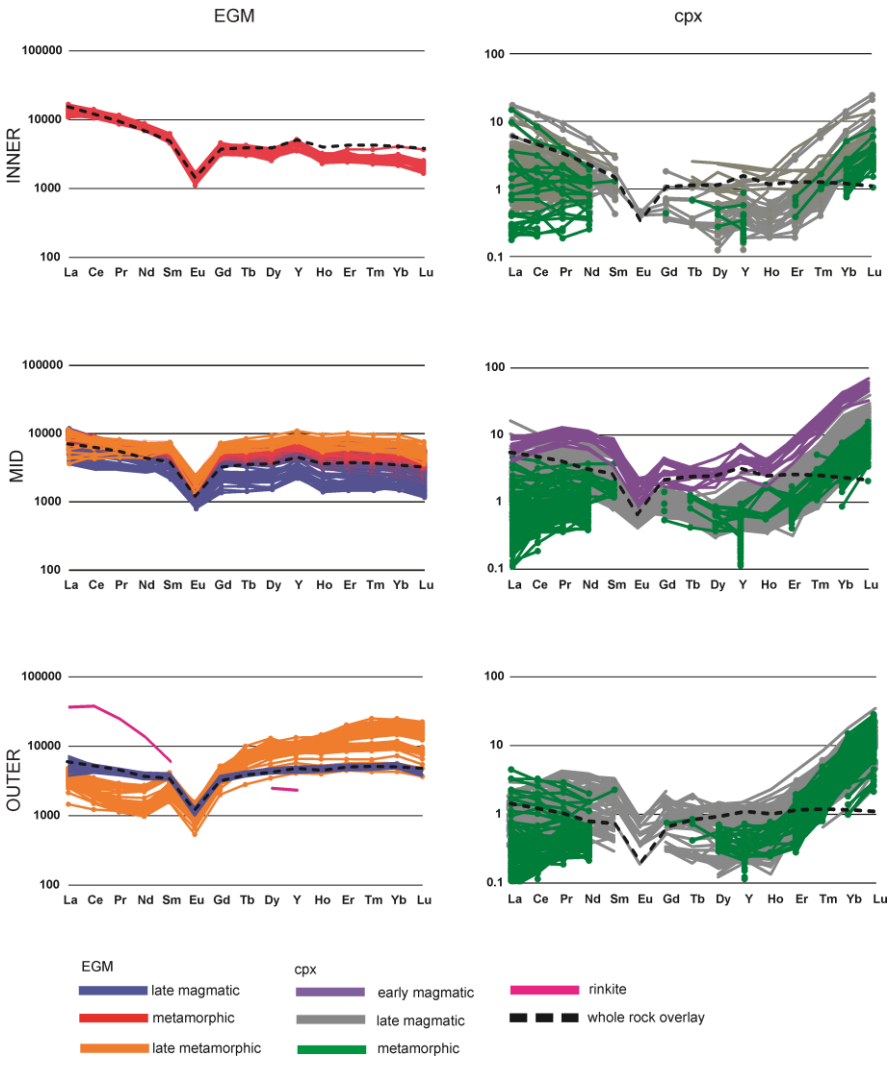

Fig. 4. Primitive mantle-normalized REE+Y patterns for sodic clinopyroxenes (cpx) and eudyalite-group minerals (EGM). For comparison, whole-rock patterns (dashed lines) are plotted as overlay. Data for rinkite is after Sokolova and Cámara (2008). Normalizing values are after Palme and O'Neill (2014).

systematic fashion. In the inner subunit, LREE (first tetrad) are concave-shaped, while MREE (Sm-Nd) and HREE show no curvature. In the outer subunit, the first tetrad is typically convex-shaped, while HREE (third and fourth tetrad) are concave-shaped. Normalized REE patterns for EGM of the mid-subunit are almost flat. A well-defined negative Eu anomaly is present across the intrusion. Positive Y anomalies are only observed in the mid- and the inner subunits (Fig. 4).

Clinopyroxene

Primitive mantle-normalized trace element patterns for aegirine show remarkable enrichment for some large ion lithophile elements (LILE) such as Li, Cs and Pb, whilst others (e.g., Sr) are depleted, with no

large differences between the three subunits and the three paragenetic generations of aegirine (Fig. 3). Amongst the HFSE, Zr and Hf are highly enriched (Hf ≥ Zr), with enrichment factors decreasing from early magmatic Zr-aegirine (between 1,000 and 3,000) via late-magmatic aegirine to metamorphic Al-aegirine (enrichment factors generally <200), again with no large differences between the three subunits (Fig. 3). In contrast, values for Nb, Ta, U and Th are lower, scatter considerably, and are in some cases depleted relative to primitive mantle (Fig. 3).

REE patterns for cpx reveal the expected low concentrations of REE – and moderate depletions or enrichments relative to primitive mantle, with factors varying between about 0.2 and 50 (Fig. 4). In general, REE are highest in early magmatic Zr-aegirine continuously decreasing towards metamorphic Al-aegirine with no large change in the shape of the REE pattern. For metamorphic Al-aegirines from all three subunits, the majority of MREE are below the limit of detection (Fig. 4). The patterns are concave-shaped for LREE and convex-shaped for HREE and especially the MREE are depleted (Fig. 4). The shape of REE patterns is characteristic for sodic cpx, and is attributed to bimodal partitioning of REE into two crystallographic sites of the cpx (Beard, 2018; Marks et al., 2004; Reguir et al., 2012). All REE patterns show a well-defined negative Eu anomaly, whilst positive Y anomalies are restricted to magmatic aegirines from the mid subunit (Fig. 4).

Discussion

This study aims to differentiate the effects of HFSE and REE partitioning under magmatic and metamorphic conditions. In doing so, it contributes to the general understanding of the genesis and alteration of EGM-bearing REE deposits resulting in local HREE enrichment under magmatic and metamorphic conditions. Trace element data for EGM and cpx, and in particular the geochemical twins Y/Ho, Zr/Hf and Nb/Ta, are compared with whole-rock geochemical data from the Norra Kärr complex, and with available data on EGM from alkaline complexes published by Schilling et al. (2011). In addition, the REE distribution between EGM and cpx as well the extreme HREE enrichment of the complex are discussed.

Parental magmas of the Norra Kärr rocks

Parental magmas for evolved EGM-bearing rocks range from alkali basaltic to nephelinitic in composition, depending largely on mantle source composition, degree of melting, and contamination (e.g., Marks and Markl, 2017 and references

therein; Schilling et al., 2011). Alkali basaltic precursors typically fractionate large amounts of plagioclase, which results in the subsequent depletion in R^{2+} ions such as Ca, Sr, Ba, and Eu (Marks et al., 2004; Nash and Crecraft, 1985; White et al., 2003). Accordingly, pronounced negative Eu anomalies and relative depletions for Sr and Ba in EGM are indicative of alkali basaltic parental melts (Marks and Markl, 2017; Schilling et al., 2011). In contrast, nephelinitic melts do not fractionate large amounts of plagioclase and evolved EGM-bearing rocks derived from such parental magmas are, therefore, relatively Ca- and Sr-rich and lack Eu anomalies (e.g., Arzamastsev et al., 2001; Kramm and Kogarko, 1994; Marks et al., 2011).

Whole-rock data and EGM from Norra Kärr are characterized by well-developed negative Eu anomalies and are relatively depleted in Ba and Sr (Table 2 and 3; Fig. 4; Sjöqvist et al., 2013). In addition, the Norra Kärr lithologies are strongly depleted in Co, V, Cr, Ni and Sc (Table 2), similar to comparable lithologies from Ilímaussaq (Bailey et al., 2001). This indicates early fractionation of olivine, augite, and spinel from as well as prolonged differentiation of an alkali basaltic magma (e.g., Arth, 1976; Beard, 2018; Canil and Fedortchouk, 2001; Marks et al., 2004; Nash and Crecraft, 1985; White et al., 2003). In accordance, the shapes of mantle-normalized REE patterns for magmatic EGM (Fig. 4) are similar to those from Ilimaussaq, Mont Saint Hilaire and Ascension Island, all of which are considered to be of alkali basaltic origin (Schilling et al., 2011). We thus suggest prolonged differentiation of alkali basaltic rather than nephelinitic parental melts as the source for the Norra Kärr rocks. The emplacement of the magmatic precursor to the Norra Kärr complex was most likely linked to the Hallandian orogenic event, during which basaltic rocks extruded during an initial rifting period, followed by the intrusion of I- to A-type granites (Brander, 2011; Brander and Söderlund, 2009).

Fractionation of the geochemical twins Y/Ho, Zr/Hf and Nb/Ta

Major silicate reservoirs including peridotite xenoliths, mid-ocean-ridge basalts (MORB), ocean-island basalts (OIB), komatiitic lava and primitive mantle show nearly chondritic and uniform ratios of Y/Ho = 28 ± 3, Zr/Hf = 37 ± 3 and Nb/Ta = 17 ± 3 (Jochum et al., 1989). This indicates a very similar partitioning behavior of these geochemical twin pairs during mantle melting and fractional crystallization in most magmatic systems (Bau and Dulski, 1995; Jochum et al., 1989) and implies largely CHArge-and-RAdius-Controlled (CHARAC) behavior (Bau, 1996). In highly evolved magmatic

systems, however, fractionation of major HFSE host minerals (e.g., zircon, baddeleyite, pyrochlore, titanite) may decouple Y/Ho, Zr/Hf, and Nb/Ta (e.g., Bea et al., 2006; Chakhmouradian, 2006; Claiborne et al., 2006; Linnen and Keppler, 2002; Marks et al., 2008; Walter et al., 2018).

Magmatic and metamorphic EGM from Norra Kärr are marked by Y/Ho, Zr/Hf and Nb/Ta ratios that increase from the outer (older) to the mid towards the inner (younger) lithological subunit, with no large differences between magmatic and metamorphic EGM in any given subunit (Fig. 5, Table 3). Both Y/Ho and Zr/Hf largely overlap with the CHARAC field, with the exception of (i) EGM from the inner subunit exhibiting larger than CHARAC Y/Ho and (ii) late-metamorphic and unusually poikilitic EGM from the outer subunit (see Atanasova et al., 2017 for details) with Y/Ho slightly lower than the CHARAC range. Similarly, chondritic Nb/Ta values are observed in the mid subunit, whereas EGM from the outer and inner subunits have lower and higher Nb/Ta, respectively. We attribute the observed development of Zr/Hf and Y/Ho within the CHARAC range from lower to higher ratios from the outer to the inner subunit to the magmatic development of the complex (Fig. 5).

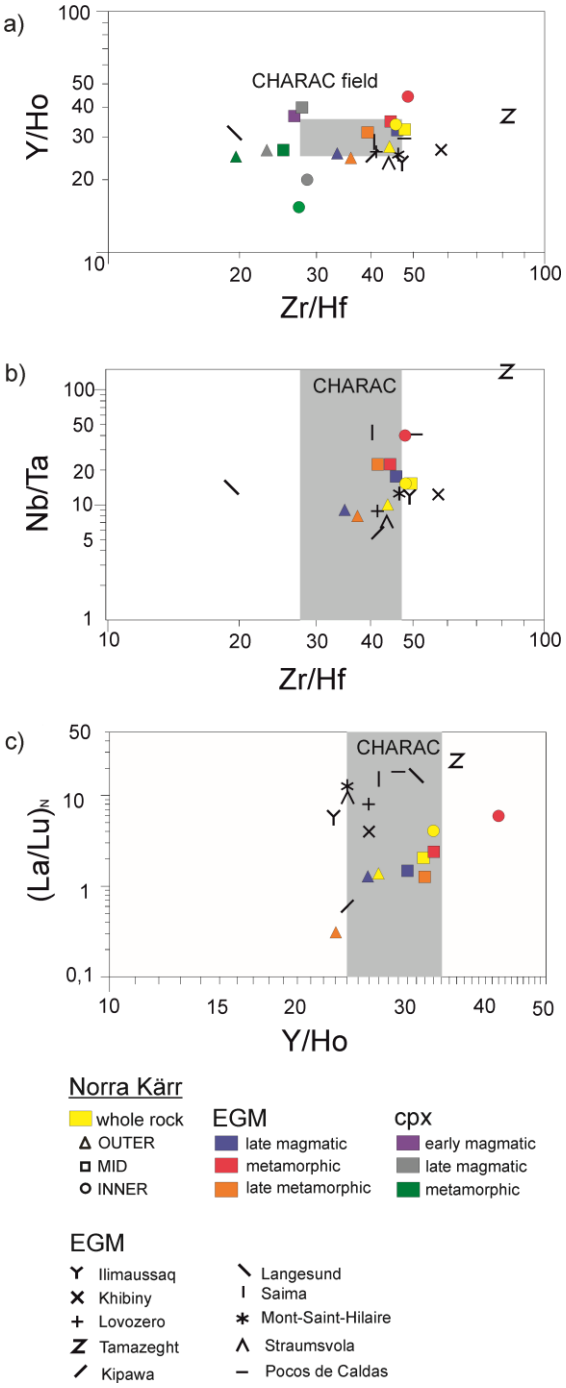

Fig.5. a) Averaged Y/Ho vs. Zr/Hf for whole-rocks, cpx and EGM from Norra Kärr; b) averaged Nb/Ta vs. Zr/Hf as well as c) primitive mantle-normalized La/Lu ((La/Lu)N) vs Y/Ho for whole-rocks and EGM from Norra Kärr are illustrated and respectively compared with available data for EGM.

We assume further that EGM are not able to fractionate the twin pairs and therefore only

minor differences are documented between magmatic and metamorphic EGM in the mid and outer subunits (Fig. 5). Very likely, a similar development has taken place in the inner subunit.

Similar to EGM from Norra Kärr, magmatic EGM from most other known examples, including the Ilimaussaq complex, Greenland and the Lovozero complex, Russia show CHARAC compositions for Y/Ho and Zr/Hf (Schilling et al., 2011; Fig. 5). Larger deviations are restricted to late-magmatic or hydrothermal EGM from Khibina, Russia and Langesund, Norway (in both for Zr/Hf) as well as from Tamazeght, Morocco (Y/Ho and Zr/Hf; Fig. 5) alkaline complexes (data used from Schilling et al., 2011). By analogy, metamorphic EGM of the inner subunit at Norra Kärr (red dot in Fig. 5), in which deformation textures are especially prominent, could as well have experienced a significant compositional overprint that may tentatively be related to syn-deformational and syn-metamorphic fluid-rock interaction (see Atanasova et al., 2017 for details). The variation of Nb/Ta on EGM from Norra Kärr is inconclusive and data from several other localities have near chondritic Nb/Ta (e.g., Langesund), but also show clear deviations to higher (e.g., Saima, China) and lower ratios (e.g., Kipawa, Canada).

The trace element chemistry of sodic clinopyroxene from Norra Kärr show no significant, systematic differences in Y/Ho and Zr/Hf between subunits; data for Nb/Ta is not available from the present study. Within a given subunit, however, Zr/Hf and Y/Ho slightly decrease from magmatic to metamorphic cpx (Fig. 5a). We attribute this to different crystallization conditions combined with a change in the major element composition of cpx from almost pure aegirine crystallized from magma at relatively high temperatures (up to 700°C) to jadeite-rich compositions formed during metamorphic conditions at 400-500°C (Atanasova et al., 2017).

When comparing Y/Ho, Zr/Hf and Nb/Ta between whole-rock, cpx and EGM (Fig. 5), two major observations are apparent: (i) All three ratios are very similar to identical between whole-rocks and EGM. (ii) For cpx, Y/Ho ratios largely overlap with those of EGM and whole-rocks, but Zr/Hf ratios for cpx (20-29) are clearly lower than those for EGM (33-46) and whole-rock samples (40-45). Since EGM are the major host of Y, Ho, Zr, Hf and also Nb and Ta in the Norra Kärr rocks, the close similarity between mineral chemistry and whole-rock data is hardly surprising. EGM contain around 12 wt.% ZrO_2, up to 2,600 mg/g Hf, up to 4 wt.% Y, up to 1,700 mg/g Ho, up to 7,000 mg/g Nb, and up to 800 mg/g Ta (Atanasova et al., 2017; Table 3).

Table 5: Modal mineralogy of subunits of the Norra Kärr complex

	Inner				Mid (matrix)	Mid (schlieren)				Outer			
	Mean	CI	95% Interval			Mean	CI	95% Interval		Mean	CI	95% Interval	
wt.%	n=3	(+/-)	Min	Max	n=1	n=17	(+/-)	Min	Max	n=7	(+/-)	Min	Max
Albite	22.88	4.15	13.27	31.66	57.87	4.43	0.84	0.00	21.83	39.66	1.44	29.73	53.85
Microcline	16.80	3.05	15.21	19.03	4.41	25.13	1.85	2.98	58.98	13.17	0.43	8.35	15.83
Aegirine	17.60	3.19	15.24	19.69	19.42	18.20	1.23	2.86	34.03	13.47	0.55	9.42	17.49
Nepheline	9.39	1.70	4.83	12.72	10.30	8.84	1.14	0.02	32.98	20.15	1.61	3.17	29.14
Natrolite	22.11	4.01	12.12	36.86	2.57	27.12	1.47	12.12	51.24	8.16	1.72	0.39	27.19
Catapleiite	1.74	0.32	0.94	2.19	2.97	2.45	0.23	0.10	6.29	1.13	0.14	0.14	2.63
Eudialyte	7.25	1.32	1.11	14.43	2.19	13.39	1.15	2.70	35.39	3.81	0.37	0.38	6.25
Other REE minerals	1.80	0.33	0.07	4.96	0.25	0.14	0.01	0.04	0.43	0.11	0.03	0.00	0.46

CI = confidential interval

Clinopyroxene, in contrast, contains only minor to trace amounts of the above-listed elements (800-20,000 mg/g Zr, 30-800 mg/g Hf, 1-20 mg/g Y, 0.1-0.5 mg/g Ho, 0.6-8 mg/g, Nb, and 0.1-1.3 mg/g Ta; Table 4). Furthermore, alkali feldspar, nepheline and natrolite, the other rock-forming silicate minerals in the nepheline syenite of Nora Kärr, can safely be assumed to contain only negligible amounts of HFSE. It is thus hardly surprising that the mineral chemistry of EGM controls the whole-rock Y/Ho, Zr/Hf and Nb/Ta (Fig. 5), despite the fact that the modal abundance of EGM (6-14 %, Table 5) is lower than that of other rock-forming silicate minerals (Table 5).

In the outer subunit, however, Zr/Hf in EGM and whole-rock are clearly different (Table 2 and 4 and Fig 5). We suggest that this is due to the relatively high modal abundance of catapleiite compared to EGM in this unit (Table 5). Catapleiite features higher Zr/Hf ratio as it incorporates more Zr (30 wt.% ZrO_2) than Hf (0.6 wt.% HfO_2) compared to EGM (Atanasova et a., 2017). Alternatively, the Zr/Hf ratio in EGM could also be influenced by the equilibrium distribution of Hf between EGM and catapleiite. We see that the Zr/Hf in EGM increases from the outer to the inner subunits with decreasing modal abundance of catapleiite. Atanasova et al. (2017) discuss in detail the combination of constraints such as a_{H2O}, a_{HCl} and REE enrichment in the melt on the coexistence and replacement of EGM and catapleiite during crystallization. Very low Zr/Hf recorded for cpx relative to those observed for EGM and whole-rock samples from Norra Kärr are attributed according to Kogarko (2015) to more compatible behavior of Hf (K_d range 0.5-0.7) compared to Zr (K_d range 0.3-0.5) for cpx.

Our observations clearly demonstrate that the geochemical twins Zr and Hf can be fractionated between minerals under magmatic conditions in highly evolved systems. Results yield distinct differences between magmatic and metamorphic EGM and cpx that are reflected by their Zr/Hf and Y/Ho ratios, with much stronger effects for cpx than for EGM. It appears that EGM, in

contrast to cpx (and catapleiite), are not able to fractionate elements in the pairs Zr-Hf and Y-Ho from each other. We assume that the HFSE geochemical twins are not robust proxies for the geochemical evolution of magmas.

Rare earth element distribution between EGM and cpx

The amount of LREE, MREE and HREE as well as the ratios REE_{EGM}/REE_{CPX} are illustrated for magmatic and metamorphic EGM and cpx using trace element data (Fig. 6). According to previous studies by Atanasova et al. (2017), we assume late magmatic EGM to be genetically similar to late magmatic aegirine, while metamorphic aegirine is linked to metamorphic and late-metamorphic EGM of the outer and mid subunits. Due to the lack of a magmatic textural record in the inner subunit, these data are not included here. Pre-EGM early-magmatic aegirine is plotted for comparison.

The largest amount of REE is hosted by EGM, namely 50,000 – 80,000 mg/g (Fig. 6), while cpx hosts far below 10,000 mg/g of total REE in the exposed part of the intrusion (Fig. 6). However, the enrichment of REE in EGM during magmatic evolution corresponds to REE depletion in cpx. Similarly, we observe inverse REE behavior in metamorphic EGM and cpx (Fig. 6b). The negative correlation between the ability of cpx to incorporate significant REE amounts and the co-crystallisation of EGM is best noticed in early magmatic "pre-EGM" aegirines, which show elevated contents of REE (up to 80 mg/g).

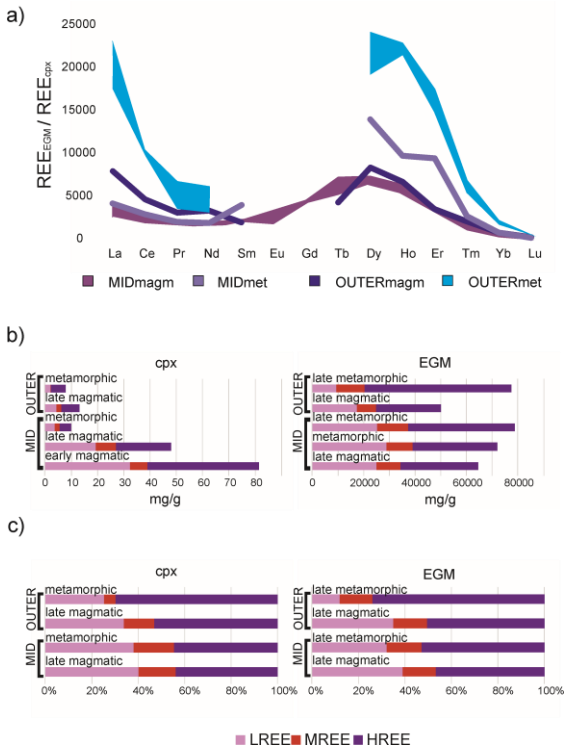

Fig. 6. The significant difference in rare earth element (REE) distribution between the mid and outer geological subunits of the Norra Kärr complex is illustrated considering elemental concentrations in both EGM and cpx (Tables 3 and 4). a) The corresponding behavior of REE during magmatic and metamorphic processes is visualized using the ratios of total rare earth amount REE_{EGM}/REE_{CPX}. The systematic change in REE concentrations from magmatic and metamorphic transition is illustrated by b) the amount and c) the proportion (as a share of 100%) of LREE (La-Nd), MREE (Sm-Dy) and HREE (Ho-Lu + Y) in magmatic to metamorphic EGM and cpx.

Similar observations have been made for clinopyroxene from Ilimaussaq, where "pre-EGM" augites (in augite syenite)

contain c. 300mg/g TREE, while "post-EGM" aegirines (in agpaites) only contain c. 40 mg/g TREE (Marks et al., 2004).

Even if it is not possible to calculate the REE partition coefficients between magma and cpx or magma and EGM, it is still obvious that K_d for EGM is always much larger than K_d for cpx. In fact, the observed inverse behavior of REE concentrations in EGM and cpx during magmatic evolution suggests that this difference increases with time.

Enrichment of HREE in late metamorphic EGM

The normalized ratio La/Lu is a proxy for the relative enrichment of LREE over HREE in minerals or rocks. La/Lu for EGM from Norra Kärr and several other locations are compared in Fig. 5c. The majority of the literature data have average La/Lu between 4 and 20, reflecting either the LREE-enrichment of the magma from which EGM crystallized or a crystallographic preference/tendency of EGM for LREE. Data for late-magmatic to hydrothermal EGM from Tamazeght have very high $(La/Lu)_N > 30$ reflecting exceptional LREE enrichment during a strong postmagmatic hydrothermal overprint.

EGM from Norra Kärr have comparatively low $(La/Lu)_N$ between 0.3 and 6.1 (Fig. 5c). This is attributed to a HREE-enriched source magma, as has been proposed for EGM from the Thor Lake layered intrusion in Canada (Möller and Williams-Jones, 2016). Late metamorphic EGM from the outer subunit show particularly low $(La/Lu)_N < 1$ (Fig. 5c). The only documented example with similarly low $(La/Lu)_N$ comes from the Kipawa complex (Canada), representing nepheline syenites deformed and metamorphosed during the ca. 1 Ga Grenvillian orogeny (Breemen and Currie, 2004) – an age, geotectonic setting and post-magmatic evolution virtually identical to that of Norra Kärr.

Atanasova et al. (2017) interpreted enrichment of Y and HREE in the late metamorphic EGM of the outer subunit as a compositional adaptation of the EGM by recrystallization in response to metamorphic deformation. In addition, late metamorphic HREE-enriched EGM of this unit are intergrown with LREE-rich rinkite-group minerals (Fig. 4b). Several studies suggest that REE, Nb, and Zr are immobile beyond the extent of local recrystallization (Borst et al., 2016; Möller and Williams-Jones, 2017; van de Ven et al., 2019). Accordingly, we assume REE fractionation and local redistribution (on the mm-scale) to be the major driving mechanisms for the observed change of mineral chemistry (decreasing La/Lu ratio, HREE enrichment) of magmatic vs. post-magmatic EGM at

Norra Kärr. We suggest that during recrystallization of magmatic EGM to late metamorphic, poikilitic EGM, LREE were released by EGM and immediately consumed to form rinkite-group minerals. HREE were obviously less mobile and remained in late metamorphic, poikilitic EGM (Fig. 4b).

Conclusions

The Norra Kärr complex is considered to be of alkali basaltic origin, its formation being linked to prolonged rifting and magmatism in the course of the Hallandian orogenic event. An enrichment of the magma in REE in general, and HREE in particular appears likely. It remains uncertain, however, if this enrichment is due to the presence of a mantle source pre-enriched in REE, or if it is related to the process of mantle melt formation. Fractional crystallization as expressed by compositional layering preserved in the now deformed and metamorphosed complex is associated with relatively minor yet systematic changes in whole-rock REE compositions. These trends are recorded by magmatic EGM, the dominant host of REE in the Norra Kärr complex. Deformation and greenschist facies metamorphism during the Grenvillian Orogeny, on the other hand, were accompanied by recrystallization and local redistribution of REE. As a result, whole-rock compositions remained unchanged, whilst the compositions of EGM changed significantly, with HREE being enriched in recrystallized EGM and LREE incorporated into rinkite-group minerals.

Results of this study also illustrate the extent at which geochemical twins such as Zr/Hf or Y/Ho of the HFSE can be fractionated during magmatic and post-magmatic alteration processes. Y/Ho fractionation observed in cpx at Norra Kärr is almost certainly related to the metamorphic overprint. Our study illustrates clearly that the mineral chemistry of cpx and EGM are not robust proxies for the geochemical evolution of magmas once the magmatic host has experienced metamorphism or a hydrothermal overprint. This is particularly true for HFSE geochemical twins – element pairs thought to be particularly suitable as geochemical proxies.

Acknowledgements

This research did not receive any specific grant from funding agencies in the public, commercial, or not-for-profit sectors.

Research for this study benefited from numerous discussions with Magnus Leijd, Axel Sjöqvist and Charles Beard. The authors are deeply grateful for their support and are in particular indebted to Charles

Beard for his significant contribution to improve the written manuscript. LA-ICP-MS analyses were carried out at the Institute for Mineralogy of the Westfälische Wilhelms-Universität Münster with the greatly appreciated assistance of Jasper Berndt and Beate Schmitt. Furthermore, the authors are indebted to Leading Edge Materials (formerly Tasman Metals Ltd.) for supporting field work, providing rock samples, geological maps and cross sections.

References

Åberg, G., 1988. Middle Proterozoic anorogenic magmatism in Sweden and worldwide. Lithos 21, 279–289.

Andersson, U.B., Rutanen, H., Johansson, Å., Mansfeld, J., Rimša, A., 2007. Characterization of the Paleoproterozoic mantle beneath the Fennoscandian Shield: Geochemistry and isotope geology (Nd, Sr) of~ 1.8 Ga mafic plutonic rocks from the Transscandinavian Igneous Belt in southeast Sweden. Int. Geol. Rev. 49, 587–625.

Arth, J.G., 1976. Behavior of trace elements during magmatic processes—a summary of theoretical models and their applications. J. Res. US Geol. Surv 4, 41–47.

Arzamastsev, A.A., Glaznev, V.N., Arzamastseva, L. V, Bea, F., Montero, P., 2001. Kola alkaline province in the Paleozoic: evaluation of primary mantle magma composition and magma generation conditions. Russ. J. Earth Sci. 3.

Atanasova, P., Krause, J., Möckel, R., Osbahr, I., Gutzmer, J., 2015. Electron Probe Microanalysis of REE in Eudialyte Group Minerals: Challenges and Solutions. Microsc. Microanal. 21, 1096–1113.

Atanasova, P., Marks, M.A.W., Heinig, T., Krause, J., Gutzmer, J., Markl, G., 2017. Distinguishing Magmatic and Metamorphic Processes in Peralkaline Rocks of the Norra Kärr Complex (Southern Sweden) Using Textural and Compositional Variations of Clinopyroxene and Eudialyte-group Minerals. J. Petrol. 58, 361–384. https://doi.org/10.1093/petrology/egx019

Bailey, J.C., Gwozdz, R., Rose-Hansen, J., Sørensen, H., 2001. Geochemical overview of the Ilímaussaq alkaline complex, South Greenland. Geol. Greenl. Surv. Bull. 190, 35–53.

Bau, M., 1996. Controls on the fractionation of isovalent trace elements in magmatic and aqueous systems: evidence from Y/Ho, Zr/Hf, and lanthanide tetrad effect. Contrib. to Mineral. Petrol. 123, 323–333.

Bau, M., Dulski, P., 1995. Comparative study of yttrium and rare-earth element behaviours in fluorine-rich hydrothermal fluids. Contrib. to Mineral. Petrol. 119, 213–223.

Bea, F., Montero, P., Ortega, M., 2006. A LA–ICP–MS evaluation of Zr reservoirs in common crustal rocks: Implications for Zr and Hf geochemistry, and zircon-forming processes. Can. Mineral. 44, 693–714.

Beard, C.D., 2018. Mineral-melt trace element partitioning in alkaline magmatic systems 152.

Bgs, C., 2011. Rare Earth Elements.

Borst, A.M., Friis, H., Andersen, T., Nielsen, T.F.D., Waight, T.E., Smit, M.A., 2016. Zirconosilicates in the kakortokites of the Ilímaussaq complex, South Greenland:

Implications for fluid evolution and high-field-strength and rare-earth element mineralization in agpaitic systems. Mineral. Mag. 80, 5–30.

Brander, L., 2011. The Mesoproterozoic Hallandian event-a region-scale orogenic event in the Fennoscandian Shield.

Brander, L., Söderlund, U., 2009. Mesoproterozoic (1.47–1.44 Ga) orogenic magmatism in Fennoscandia; Baddeleyite U–Pb dating of a suite of massif-type anorthosite in S. Sweden. Int. J. Earth Sci. 98, 499–516.

Breemen, O. van, Currie, K.L., 2004. Geology and U Pb geochronology of the Kipawa Syenite Complex a thrust related alkaline pluton and adjacent rocks in the Grenville Province of western Quebec. Can. J. Earth Sci. 41, 431–455.

Canil, D., Fedortchouk, Y., 2001. Olivine–liquid partitioning of vanadium and other trace elements, with applications to modern and ancient picrites. Can. Mineral. 39, 319–330.

Chakhmouradian, A.R., 2006. High-field-strength elements in carbonatitic rocks: geochemistry, crystal chemistry and significance for constraining the sources of carbonatites. Chem. Geol. 235, 138–160.

Claiborne, L.L., Miller, C.F., Walker, B.A., Wooden, J.L., Mazdab, F.K., Bea, F., 2006. Tracking magmatic processes through Zr/Hf ratios in rocks and Hf and Ti zoning in zircons: an example from the Spirit Mountain batholith, Nevada. Mineral. Mag. 70, 517–543.

Goodenough, K.M., Schilling, J., Jonsson, E., Kalvig, P., Charles, N., Tuduri, J., Deady, E.A., Sadeghi, M., Schiellerup, H., Müller, A., Bertrand, G., Arvanitidis, N., Eliopoulos, D.G., Shaw, R.A., Thrane, K., Keulen, N., 2016. Europe's rare earth element resource potential: An overview of REE metallogenetic provinces and their geodynamic setting. Ore Geol. Rev. 72, Part 1, 838–856. https://doi.org/http://dx.doi.org/10.1016/j.oregeorev.2015.09.019

Jaireth, S., Hoatson, D.M., Miezitis, Y., 2014. Geological setting and resources of the major rare-earth-element deposits in Australia. Ore Geol. Rev. 62, 72–128.

Jochum, K.P., McDonough, W.F., Palme, H., Spettel, B., 1989. Compositional constraints on the continental lithospheric mantle from trace elements in spinel peridotite xenoliths. Nature 340, 548.

Jochum, K.P., Stoll, B., Herwig, K., Willbold, M., 2007. Validation of LA-ICP-MS trace element analysis of geological glasses using a new solid-state 193 nm Nd: YAG laser and matrix-matched calibration. J. Anal. At. Spectrom. 22, 112–121.

Jochum, K.P., Stoll, B., Herwig, K., Willbold, M., 2006. Improvement of in situ Pb isotope analysis by LA-ICP-MS using a 193 nm Nd: YAG laser. J. Anal. At. Spectrom. 21, 666–675.

Johnsen, O., Ferraris, G., Gault, R.A., Grice, J.D., Kampf, A.R., Pekov, I. V, 2003. The nomenclature of eudialyte-group minerals. Can. Mineral. 41, 785–794.

Karup-Møller, S., Rose-Hansen, J., 2013. New data on eudialyte decomposition minerals from kakortokites and associated pegmatites of the Ilímaussaq complex, South Greenland. Geol. Soc. Denmark. Bull. 61, 47–70.

Karup-Møller, S., Rose-Hansen, J., Sørensen, H., 2010. Eudialyte decomposition minerals with new

hitherto undescribed phases from the Ilímaussaq complex, South Greenland. Geol. Soc. Denmark. Bull. 58, 75–88.

Kogarko, L.N., 2015. Fractionation of zirconium in pyroxenes of alkaline magmas. Geochemistry Int. 53, 1–8.

Kramm, U., Kogarko, L.N., 1994. Nd and Sr isotope signatures of the Khibina and Lovozero agpaitic centres, Kola Alkaline Province, Russia. Lithos 32, 225–242.

Linnen, R.L., Keppler, H., 2002. Melt composition control of Zr/Hf fractionation in magmatic processes. Geochim. Cosmochim. Acta 66, 3293–3301.

Marks, M., Halama, R., Wenzel, T., Markl, G., 2004. Trace element variations in clinopyroxene and amphibole from alkaline to peralkaline syenites and granites: implications for mineral–melt trace-element partitioning. Chem. Geol. 211, 185–215.

Marks, M.A.W., Coulson, I.M., Schilling, J., Jacob, D.E., Schmitt, A.K., Markl, G., 2008. The effect of titanite and other HFSE-rich mineral (Ti-bearing andradite, zircon, eudialyte) fractionation on the geochemical evolution of silicate melts. Chem. Geol. 257, 153–172.

Marks, M.A.W., Hettmann, K., Schilling, J., Frost, B.R., Markl, G., 2011. The mineralogical diversity of alkaline igneous rocks: critical factors for the transition from miaskitic to agpaitic phase assemblages. J. Petrol. 52, 439–455.

Marks, M.A.W., Markl, G., 2017. A global review on agpaitic rocks. Earth-Science Rev. 173, 229–258.

Mitchell, R.H., 2015. Primary and secondary niobium mineral deposits associated with carbonatites. Ore Geol. Rev. 64, 626–641.

Möller, V., Williams-Jones, A.E., 2017. Magmatic and Hydrothermal Controls on the Mineralogy of the Basal Zone, Nechalacho REE-Nb-Zr Deposit, Canada☼. Econ. Geol. 112, 1823–1856. https://doi.org/10.5382/econgeo.2017.4531

Möller, V., Williams-Jones, A.E., 2016. Petrogenesis of the Nechalacho Layered Suite, Canada: Magmatic Evolution of a REE–Nb-rich Nepheline Syenite Intrusion. J. Petrol. 57, 229–276.

Nash, W.P., Crecraft, H.R., 1985. Partition coefficients for trace elements in silicic magmas. Geochim. Cosmochim. Acta 49, 2309–2322.

Palme, H., O'Neill, H., 2014. Cosmochemical Estimates of Mantle Composition. Planets, Asteriods, Comets and The Solar System, Volume 2 of Treatise on Geochemistry . Edited by Andrew M. Davis.

Pfaff, K., Krumrei, T., Marks, M., Wenzel, T., Rudolf, T., Markl, G., 2008. Chemical and physical evolution of the 'lower layered sequence'from the nepheline syenitic Ilímaussaq intrusion, South Greenland: Implications for the origin of magmatic layering in peralkaline felsic liquids. Lithos 106, 280–296.

Pfaff, K., Wenzel, T., Schilling, J., Marks, M.A.W., Markl, G., 2010. A fast and easy-to-use approach to cation site assignment for eudialyte-group minerals. Neues Jahrb. für Mineral. J. Mineral. Geochemistry 187, 69–81.

Rankin, L.R., 2011. Structural setting of the Norra Kärr intrusive complex, Central Sweden. Geointerp Confidential Report 2011/14.

Rastsvetaeva, R.K., 2007. Structural mineralogy of the eudialyte group: A review. Crystallogr. Reports 52, 47–

64. https://doi.org/10.1134/s1063774507010063

Reguir, E.P., Chakhmouradian, A.R., Pisiak, L., Halden, N.M., Yang, P., Xu, C., Kynický, J., Couëslan, C.G., 2012. Trace-element composition and zoning in clinopyroxene-and amphibole-group minerals: implications for element partitioning and evolution of carbonatites. Lithos 128, 27–45.

Salvi, S., Fontan, F., Monchoux, P., Williams-Jones, A.E., Moine, B., 2000. Hydrothermal mobilization of high field strength elements in alkaline igneous systems: evidence from the Tamazeght Complex (Morocco). Econ. Geol. 95, 559–576.

Schilling, Julian, Marks, M.A.W., Wenzel, T., Vennemann, T., Horváth, L., Tarassoff, P., Jacob, D.E., Markl, G., 2011. The magmatic to hydrothermal evolution of the intrusive mont saint-hilaire complex: Insights into the late-stage evolution of peralkaline rocks. J. Petrol. 52, 2147–2185.

Schilling, J, Wu, F.-Y., McCammon, C., Wenzel, T., Marks, M.A.W., Pfaff, K., Jacob, D.E., Markl, G., 2011. The compositional variability of eudialyte-group minerals. Mineral. Mag. 75, 87–115.

Sjöqvist, A.S.L., 2015. Agpaitic rocks of the Norra Kärr alkaline complex. Earth Sci. University of Gothenburg.

Sjöqvist, A.S.L., Cornell, D.H., Andersen, T., Andersson, U.B., Christensson, U.I., Ranjer, S.J.E., Holtstam, D., Leijd, M., 2014. Geochronology of the Norra Kärr alkaline complex, southern Sweden, in: 31st Nordic Geological Winter Meeting, Lund, Sweden.

Sjöqvist, A.S.L., Cornell, D.H., Andersen, T., Erambert, M., Ek, M., Leijd, M., 2013. Three compositional varieties of rare-earth element ore: eudialyte-group minerals from the Norra Kärr Alkaline Complex, Southern Sweden. Minerals 3, 94–120.

Smith, M.P., Moore, K., Kavecsánszki, D., Finch, A.A., Kynicky, J., Wall, F., 2016. From mantle to critical zone: A review of large and giant sized deposits of the rare earth elements. Geosci. Front.

Söderlund, U., Möller, C., Andersson, J., Johansson, L., Whitehouse, M., 2002. Zircon geochronology in polymetamorphic gneisses in the Sveconorwegian orogen, SW Sweden: ion microprobe evidence for 1.46–1.42 and 0.98–0.96 Ga reworking. Precambrian Res. 113, 193–225.

Sokolova, E., Cámara, F., 2008. From structure topology to chemical composition. VIII. Titanium silicates: the crystal chemistry of mosandrite from type locality of Låven (Skådön), Langesundsfjorden, Larvik, Vestfold, Norway. Mineral. Mag. 72, 887–897.

van de Ven, M.A.J., Borst, A.M., Davies, G.R., Hunt, E.J., Finch, A.A., 2019. Hydrothermal Alteration of Eudialyte-Hosted Critical Metal Deposits: Fluid Source and Implications for Deposit Grade. Minerals 9, 422.

Wahlgren, C.-H., Cruden, A.R., Stephens, M.B., 1994. Kinematics of a major fan-like structure in the eastern part of the Sveconorwegian orogen, Baltic Shield, south-central Sweden. Precambrian Res. 70, 67–91.

Wahlgren, C., Stephens, M.B., 2004. Tectonometamorphic reworking of TIB rocks during the Sveconorwegian orogeny, south-central Sweden. Spec. Pap. Surv. Finl. 37, 56.

Walter, B.F., Burisch, M., Fusswinkel, T., Marks, M.A.W., Steele-MacInnis, M., Wälle, M., Apukhtina, O.B., Markl, G., 2018. Multi-reservoir fluid mixing processes in rift-related hydrothermal

veins, Schwarzwald, SW-Germany. J. Geochemical Explor. 186, 158–186.

White, D.J., Musacchio, G., Helmstaedt, H.H., Harrap, R.M., Thurston, P.C., Van der Velden, A., Hall, K., 2003. Images of a lower-crustal oceanic slab: Direct evidence for tectonic accretion in the Archean western Superior province. Geology 31, 997–1000.

Wood, B.J., Blundy, J.D., 1997. A predictive model for rare earth element partitioning between clinopyroxene and anhydrous silicate melt. Contrib. to Mineral. Petrol. 129, 166–181.